Terahertz Patch Antenna Microcavity Lasers with Integrated Beam Control

Okinawa Institute of Science and Technology
Graduate University

Thesis submitted for the degree

Doctor of Philosophy

Terahertz Patch Antenna Microcavity Lasers with Integrated Beam Control

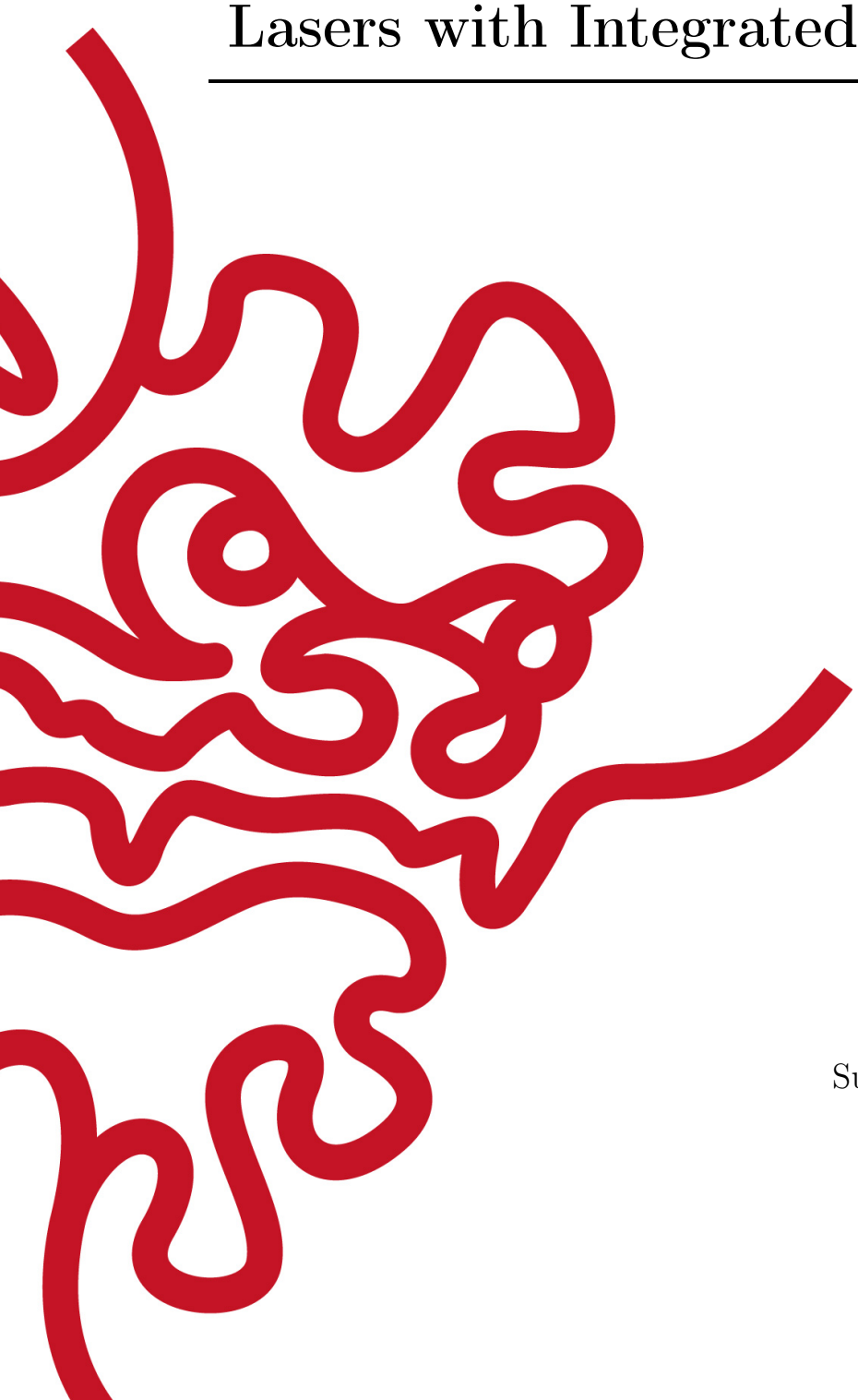

by

Joel Pérez Urquizo

Supervisor: **Keshav M. Dani**

September 2021

Declaration of Original and Sole Authorship

I, Joel Pérez Urquizo, declare that this thesis entitled *Terahertz Patch Antenna Microcavity Lasers with Integrated Beam Control* and the data presented in it are original and my own work.

I confirm that:

- No part of this work has previously been submitted for a degree at this or any other university.
- References to the work of others have been clearly acknowledged. Quotations from the work of others have been clearly indicated, and attributed to them.
- In cases where others have contributed to part of this work, such contribution has been clearly acknowledged and distinguished from my own work.
- None of this work has been previously published elsewhere, with the exception of the following:

  1. **J. Pérez-Urquizo**, Y. Todorov, L. Li, A.G. Davies, E.H. Linfield, C. Sirtori, J. Madéo and K.M. Dani, "Monolithic patch-antenna THz lasers with extremely low beam divergence and polarization control", ACS Photonics, 8, 2, 412–417 (2021).
  2. **J. Pérez-Urquizo**, J. Madéo and K.M. Dani, "Optical losses in THz arrays of patch-antenna microcavities coupled to subwavelength wires," Proc. SPIE 11827, Terahertz Emitters, Receivers, and Applications XII, 118270A (2021).
  3. J. Madéo, **J. Pérez-Urquizo**, Y. Todorov, C. Sirtori, and K. M. Dani, "Engineering the Losses and Beam Divergence in Arrays of Patch Antenna Microcavities for Terahertz Sources," Journal of Infrared, Millimeter, and Terahertz Waves 38, 1321-1330 (2017).

  Results of publication no. 3 were jointly generated by the first author of the publication and myself. Section 2.3 includes some results from this publication. Authorization to use the results has been obtained from the first author.

Date: September 2021
Signature:

Joel Pérez Urquizo

Abstract

Terahertz (THz) refers to the region of the electromagnetic spectrum that lies in between the infrared and microwaves. This frequency range possesses great potential to host several applications in wide-ranging fields, such as wireless communications, astronomy, non-invasive imaging and security scanning. However, despite sustained progress over the past decade, THz technology has not yet reached the level of maturity and flexibility of the neighboring radio frequency (RF) and optical range. One missing key aspect is the ability to integrate advanced beam control functionalities within a monolithic platform. A promising approach to achieve this goal is to combine within a single device two features of the neighboring ranges: optical microcavities, that can sustain efficient lasing operation; and antenna arrays, providing a high level of beam control. In this thesis, we investigate via simulations fabrication and characterization the emission properties of arrays of patch antenna-coupled microcavities embedding quantum cascade active regions. The geometrical configuration of the array allows independent and simultaneous tuning of the losses governing the microcavities as well as beam shaping by constructive interference in the far-field. We show that optimized arrays emit THz with unprecedented low beam divergence and robust lasing in single frequency and spatial mode. Additionally, we demonstrate polarization functionalization by coupling the patch antenna microcavities with plasmonic wires. This feature introduces an additional degree of freedom to adjust the relative emission from the cross-polarized modes of the patch, allowing the device to radiate with any coherent polarization state from linear to circular. Finally, we discuss how this design can further enable other advanced functionalities such as active beam steering and control of THz non-linearities. The successful implementation of integrated advanced functionalities and sources on-a-chip demonstrates the ability of our platform to replicate in the THz range the beam control concepts used in the RF and optics, thus paving the way towards establishing a mature technology in this range of the electromagnetic spectrum.

Acknowledgment

I would like to express my sincere gratitude to the people, without whom it would not have been possible to complete this work.

First, to my supervisor Prof. Keshav Dani who kindly accepted me as a member of the Femtosecond Spectroscopy Unit (FSU), and trusted me (and Julien) enough to let me realize my thesis in a field a little bit out of the scope of the main research line of the lab. I am very grateful to him for providing me with an excellent research environment to pursue my research.

I would like to thank my mentor Prof. Ulf Skoglund for the useful mentoring sessions I had with him over the course of my PhD life. I am grateful for his favorable advices and for making sure everything was going well by my side every time I met him.

Many thanks as well to Prof. Sirtori and Prof. Todorov from École Normale Supérieure for collaborating with us. Their inputs for understanding the patch microcavity physics and their writing contributions during the elaboration of my paper made a significant impact in the quality of this work.

None of this would have been possible without the QC samples provided by our collaborators at the University of Leeds. I would like to thank Prof. Edmund Linfield, Prof. Giles Davies and Dr. Lianhe Li for the high quality samples that they provided us.

I would like to acknowledge the expertise and valuable support from the engineering section and nano-fabrication team at OIST. Thanks to current and former members for providing the training of specialized instrumentation, maintaining and keeping the clean room operational, and assisting in troubleshooting whenever needed.

Great part of the simulations work performed in this thesis was possible thanks to the assistance and guidance for using the HPC clusters (the former SANGO and the newest DEIGO systems) at OIST provided by Dr. Jan Morén.

Special thanks to all the Graduate School staff for constant support and for simplifying all academic/non-academic -related paperwork.

Next, I would like to thank all the members of the FSU unit with whom I interacted during my life as a PhD student. I appreciate the daily spontaneous conversations, the opportunity of learning from everybody and all the moments that we created at numerous gatherings and travels.

To Dr. Julien Madéo, I would like to express my deepest gratitude for his invaluable contribution and endless support. I would like to thank him for assuming the role of my principal mentor and for guiding my research. Section 2.3 includes data that we jointly generated and published in "Journal of Infrared, Millimeter, and Terahertz

Waves 38, 1321-1330". I would like to thank him for authorizing the use of this data in my thesis. Likewise, I would like to thank him for the many hands on training on ultrafast-, optical- and THz instrumentation; help in data analysis and interpretation; scientific writing and proofreading; preparation for conference presentations and many more. Further, I am very grateful of his commitment and dedication to my professional development. Not only did I have useful discussions about science with him, but also about career development, which helped me to get a vision of what to do next in my professional career. Thanks for being the best scientific model and mentor I could have for my PhD.

I would like to thank my friends from whom I received so many joys throughout all this time. I am so grateful to have met wonderful people with whom I created moments that I will cherish forever.

Lastly, I want to thank my family for their constant support and love. Despite being geographically distant, they always continue to support me unconditionally in any aspect.

Abbreviations

AF	array factor
BWO	backward wave oscillator
CW	continuous wave
DFB	distributed feedback
DMD	digital micromirror device
FP	Fabry-Pérot
FTIR	Fourier Transformed Infrared
FWHM	full width half maximum
GaAs	gallium arsenide
ICP	inductively coupled plasma
IR	infrared
L-I-V	light-current-voltage
LO	longitudinal optical
MBE	molecular beam epitaxy
Mid-IR	mid-infrared
NIR	near infrared
OIST	Okinawa Institute of Science and Technology
PAM	patch antenna microcavity
PEC	perfect electric conductor
PMC	perfect magnetic conductor
PVD	physical vapor deposition
QC	quantum cascade
QCL	quantum cascade laser
QW	quantum well
RF	radio frequency
RTD	resonant tunneling diode
SI-SP	semi-insulating surface plasmon
TE	transverse electric
THz	terahertz
TM	transverse magnetic
VECSEL	vertical-external-cavity surface-emitting laser

Contents

List of Figures

Introduction

Patch antennas have had a significant impact on modern telecommunications systems due to the high degree of beam engineering achievable when used in arrays, offering great flexibility in designing radiation characteristics tailored for specific applications and simplicity of fabrication. Recently, the basic principles of antenna arrays with patch-like subwavelength resonators have been replicated in optical frequencies to achieve remarkable functionalities, such as field enhancement in photodetectors [1], strong light localization for trapping and sensing [2], perfect absorbers [3], thermal emitters [4, 5], beam shaping [6] and room temperature Mid-IR detectors when used in combination with active semiconductor heterostructures [7]. In the terahertz (THz) range, patch antennas have been used for fundamental studies [8] and as passive metamaterials [9] but their functionalization with electrical inputs remains challenging. The adaptation of these structures for THz emission has remained questionable due to their very low-quality factors [10, 11] and the divergent emission of the beam [12, 13], making them impractical for applications. As such, only electroluminescence has been reported [14, 15]. Lasing has also been demonstrated, but only through the use of external cavities [16–19], yet a monolithic solution remains puzzling. Transferring the observed characteristics of patch antennas from neighboring regimes into the THz domain would represent a significant technological advancement, as current THz technologies lack mature components and systems capable of integrating flexible foundations for beam generation and control.

A feasible approach for translating this concept to the THz regime is by associating arrays of patch antennas with metal-dielectric-metal -also called double metal (DM)- microcavities loaded with active semiconductor heterostructures. In this thesis, we investigate the emission properties of patch antenna microcavity (PAM) arrays incorporating quantum cascade (QC) active regions. Large arrays of PAMs provide engineered photon extraction efficiencies and higher quality factors than the single microcavity case, allowing lasing operation. Further, the collective effects introduced by the arrays permit the beam to be shaped by designing constructive interferences in the far-field. Concretely, we investigate planar arrays composed of 10×10 PAM elements interconnected with subwavelength wires along one direction. This device architecture leads to a robust single mode lasing with unprecedented beam divergence, better than $2^{\circ} \times 2^{\circ}$, which depends only on the number of resonators, allowing to functionalize the device while preserving a high-quality far-field pattern.

Chapter 1 contains a review of the basic concepts of the THz range, together with a description of the unique properties of the THz band that have motivated scientific research and the development of applications. Next, a broad review of the current tech-

nical approaches for generating THz radiation is presented, making special emphasis in the THz quantum cascade laser (QCL). Basic laser theory, along with a historical review leading to the development of the firsts THz QCLs is presented at the end of this chapter.

Chapter 2 provides a detailed description of patch antennas starting from the point of view of the microwave regime, and then providing a numerical study of their behavior when scaled to THz frequencies. At the end of this chapter, particular attention is given to the case when patch microcavities are interconnected by subwavelength wires.

Chapter 3 merges the concepts of THz QCLs and patch antenna arrays to form the PAM THz QCL concept. Detailed descriptions of the fabrication process and characterization of devices are given. The chapter finishes by presenting large-scale full-wave simulations of the emission from entire arrays.

Finally, in chapter 4, examples of device functionalization are presented. First, the chapter introduces a polarization control scheme based on the coherent manipulation of the orthogonal fundamental PAM modes, provided by the interconnecting wires' geometry. Numerical simulations for modeling the selection of a polarization state and experimental demonstrations are presented. The chapter finishes by discussing possible future work directions that can be pursued with the investigated devices, including the integration of nonlinear second harmonic generation in THz QCLs, THz QCLs with integrated beam steering and room temperature PAM THz QCLs exploiting integrated nonlinear down-conversion of mid-infrared QCLs.

Chapter 1

Terahertz Quantum Cascade Lasers

1.1 The terahertz range

Much of our understanding of how nature works is based on the study of interactions between matter and electromagnetic radiation. Thanks to this, a myriad of technologies and applications have been established exploiting most of the electromagnetic spectrum: radio technologies and mobile communications at long and microwave wavelengths, fiber-optics communications at infrared frequencies, laser and photonic technologies in the visible, ultraviolet germicidal irradiation with UV light-emitting diodes, medical imaging and material characterization with X-rays, among many others. When ordering these technologies in a line according to their operation frequency, a gap between the microwave band and the infrared range appears. This is the so-called THz band.

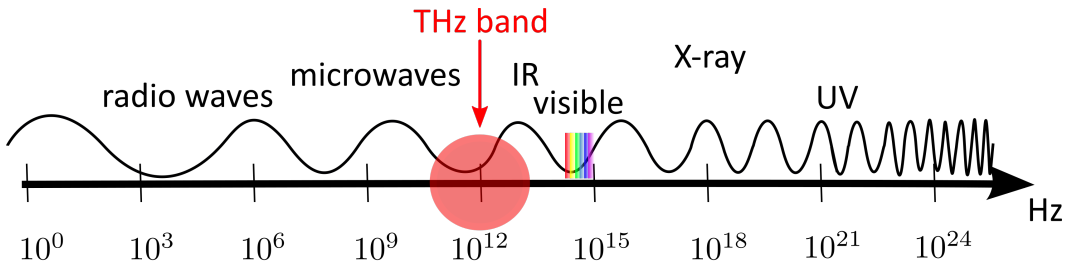

Figure 1.1: The electromagnetic spectrum. Highlighted at the centre the THz band.

The THz band, graphically depicted in Figure 1.1, is commonly defined in the frequency range between 100 GHz and 10 THz (corresponding to wavelengths of radiation ranging from 3 mm to 30 μm and photon energies from 0.4 meV to 40 meV). This band has remained under-explored for long time due to a lack of efficient, affordable and compact sources and detectors of THz radiation. Because of this, the band was also referenced as the THz gap. However, due to the growing interest in developing applications around this band, the THz gap started to be filled in the recent years. There are numerous opportunities in this band which drive the interest for develop-

ing THz technologies. For example, the THz band spans the energy scale of many fundamental excitations in condensed matter, like lattice vibrations (optical phonons), intermolecular vibrations, superconductive energy gaps, among others [20–22]. Then, THz spectroscopy can be utilized to explore the fundamental properties of many body-systems [23, 24]. Also, due to the excitation of inter- and intra- molecular modes, fundamental molecules exhibit unique spectral fingerprints in the THz region, permitting the accurate identification of drugs, gases and even explosive chemicals [25–27]. Other ideas for exploiting the potential of THz waves involve their ability to transmit through a wide variety of materials including fabrics, plastics, ceramics, etc. This attribute makes this band an attractive candidate for imaging applications [28], non-destructive testing [29] and security scanning [30]. Additionally, THz radiation is not associated with ionizing effects due to the low energy of THz photons. This has drawn attention for fostering applications in the medical sector such as the examination of *in vivo* tissues [31, 32] or the detection of cancer [33, 34]. An interesting avenue of research in the field of telecommunications is also pursued using THz waves. The largely available bandwidths at the THz band confer the possibility of short range ultra high speed mobile communications at Terabit/second data rates [35–37].

The majority of these examples have remained as laboratory demonstrations, and turning them into real-world applications has remained elusive. One of the main reasons is the lack of efficient, compact and reliable devices to generate THz radiation. A great deal of effort is still needed to bring a similar maturity level of THz technologies like that in the neighboring regimes. Today, one of the most active areas in THz research is the development of novel sources capable of controlling and manipulating THz waves [38, 39].

1.1.1 Terahertz sources

Compact, coherent, high-power, and tunable THz sources and devices with advanced functionalities are required to satisfy applications needs. Nonetheless, this is very difficult to achieve in practice. A graphical representation of the availability of sources in the THz range is shown in the graph of Figure 1.2.

Figure 1.2 shows the output power from different sources as a function of frequency. In the low-frequency end of the THz regime, THz is generated by frequency up-conversion of a signal generated by electronics means, such as Schottky diode multipliers and resonant tunneling diodes (RTD) [41, 42]. Other sources based on solid-state electronics capable of providing milliwatt-level power below 1 THz include gyrotrons [43] and backward wave oscillators (BWO) [44]. In these technologies, THz radiation is generated by accelerating electrons moving through a strong magnetic field. While these sources provide high power, they require strong magnetic fields for their operation, making them unattractive for applications. Also, radiation becomes very inefficient with increasing frequencies causing a collapse in power for all the electronics-based sources above $\sim$ 1 THz. Between 1 and 10 THz, the availability of sources for generating THz is more limited. Free electron lasers (FEL) can output optical power in kilowatts but require large facilities for their operation [45]. More compact devices outputting high power ($\sim$10 W) at THz frequencies are the p-doped germanium lasers, but require cryogenic cooling and large magnetic fields, hampering their practical im-

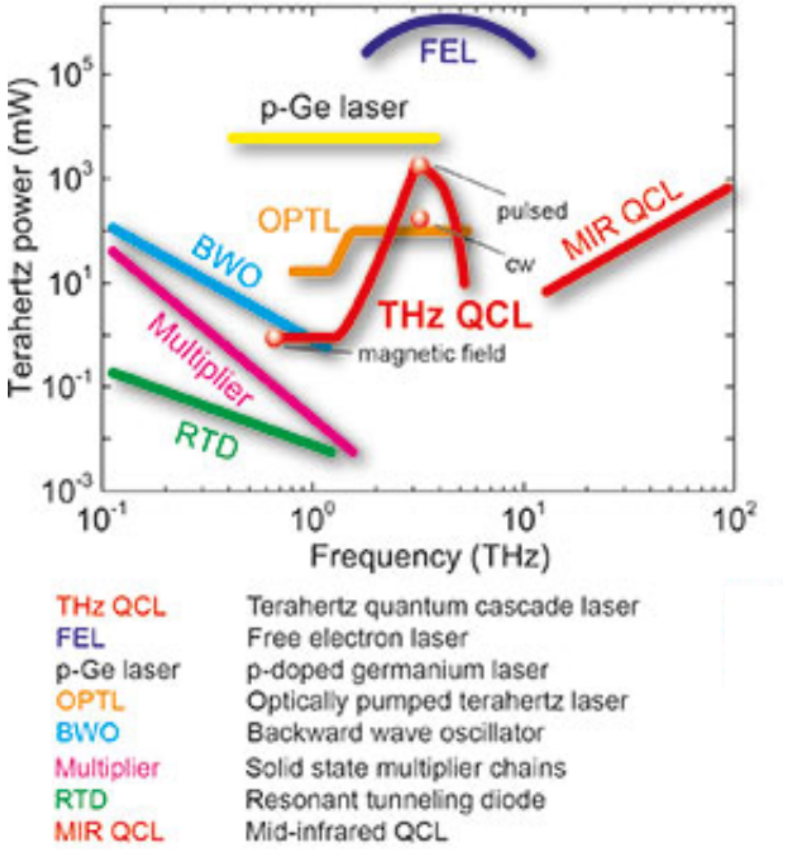

Figure 1.2: Available sources in the THz range and their respective achievable output power. Taken from Ref [40].

plementation [46]. In the same way, optically pumped methods like photoconductive antennas [47–49], optical rectification in nonlinear crystals [50, 51] or emission from air plasma induced by femtosecond optical pulses [52, 53], are high field and high power sources requiring costly and bulky external ultrafast laser systems.

In comparison with those methods, THz quantum cascade lasers (THz QCLs), unipolar semiconductor lasers exploiting intersubband transitions between quantum wells engineered at the nanometer scale, are the most compact devices covering a frequency range from 1 to 5 THz [54]. After almost 2 decades from their first demonstration, THz QCLs have emerged as a promising tool to develop efficient sources and devices, as the quantum-engineered design of QCLs enables electronic and optical properties to be tailored at will. Dedicated research on this device has lead to impressive performances. For instance, output powers >1 W [55, 56], operating temperatures as high as 250 K (easily accessible by thermoelectric Peltier cooling) [57] and continuous-wave (cw) operation [58–60]. Moreover, THz QCL gain media and their inherent high nonlinearities can be successfully exploited to produce frequency combs [61, 62], radiation amplifiers [63, 64], wavelength converters to telecomm NIR bands [65, 66] and integrated photonic mm-wave generation [67].

The following sections will provide the basic principles of operation of QCLs, start-

ing with a historic overview leading to the development of the firsts THz QCLs. Common active regions and waveguides designs developed to work at THz frequencies will be introduced and explained in detail at the end of this chapter.

1.2 Terahertz quantum cascade lasers

The firsts semiconductor lasers, developed in the 1960s, were based on GaAs p-n junctions [68, 69]. In these lasers, light emission is associated with electronic transitions between edge states in the conduction band and valence bands (interband transitions). Optical amplification via stimulated emission is carried out for a sufficiently large carrier density in the edge state of the conduction band. Electrons located in this band make optical transitions to the highest energy levels of the valence band by electron-hole recombination across the bandgap of the material, as depicted in Figure 1.3 a). In this scenario, the minimum frequency of the emitted photons is dictated by the energy bandgap of the semiconductor E_{BG}. Conventional semiconductors have a bandgap energy over a wide range in the eV regime. Due to the low energy levels of THz photons (4 meV - 40 meV), a THz laser based on this interband transition scheme cannot be realized.

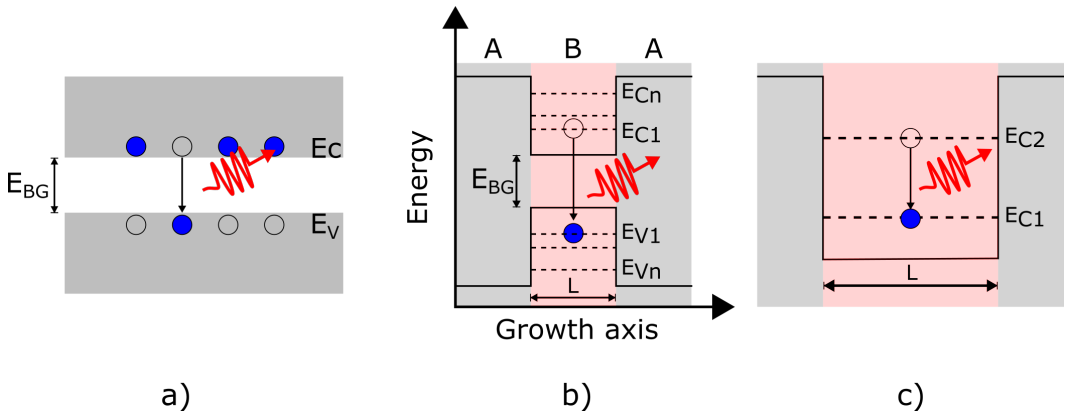

Figure 1.3: Optical transitions for different semiconductor laser schemes. a) Laser action in an interband laser. Optical transition occurs between electrons at the edge of the conduction band E_C recombining with holes at the valence band E_V. Emitted photons have an energy equal to the bandgap E_{BG}. b) Quantum well heterostructure laser. In this scheme, electrons are confined in the growth direction of a semiconductor material B, which is sandwiched by two layers of a semiconductor material A with a greater energy bandgap. Optical transitions occur between any of the discrete energy levels E_{Cn} and E_{Vn}. The energy of the emitted photons is greater than E_{BG}. c) Intersubband laser where optical transitions occur between subbands within the conduction band, therefore the energy of the emitted photons is $< E_{BG}$.

In 1975, van der Ziel et al. presented the first intersubband quantum well (QW) heterostructure laser [70]. A single quantum well is composed of a narrow bandgap semiconductor B grown in between two layers of a wider bandgap semiconductor A (Figure 1.3 b)). The resulting QW will contain discrete energy levels known as sub-

bands. The energy separation between the subbands is given by (for the case of a well of infinite potential):

$$\Delta E_n = \frac{\hbar^2 \pi^2 (2n+1)}{2m^* L^2} \tag{1.1}$$

where $\hbar = h/2\pi$ is the reduced Planck's constant, m^* is the electron's effective mass and L is the width of the quantum well. In QW heterostructure lasers, photons are emitted when an electron falls from a confined state in the conduction band, to another confined state in an energy level in the valence band. While the energy of the emitted photons can be tuned by simply varying the width of the wells, the minimum achievable energy is still limited by the bandgap of the semiconductor material. In 1971, Kazarinov and Suris envisaged a laser scheme based on optical intersubband transitions between separate subbands within the conduction band of a QW periodic structure [71]. In this model, the energy of the emitted photons is no longer limited by the semiconductor bandgap, therefore the emission energy can be significantly reduced (an illustration of this mechanism is depicted in Figure 1.3 c)). This concept formed the basis for the invention of the QCL. In 1994, after huge efforts for developing an epitaxy method capable of depositing thin films of single crystals at the nanometer scale in a controllable way, the first QCL was experimentally demonstrated by Faist et al. [72]. The laser was made from a AlInAs/GaInAs heterojunction material system lattice and emitted in the mid-IR with a wavelength of 4.2 μm (71 THz), with a maximum output power of 8 mW.

Figure 1.4 illustrates a very simple representation of the operating principle of a QCL.

The bandstructure of a QCL is formed by combining many QWs together into a chain or superlattice. The effect of this combination is that the electronic wavefunctions of neighboring QWs are delocalized in the wells and are energy-splitted. The set of wavefunctions of the different QWs comprising the superlattice form delocalized minibands. An electric field is applied perpendicular to the device to bend the bandstructure and align the minibands in order to obtain a population inversion and to allow the injection of current. Electrons are injected into an excited state E_{C2} of a miniband m by tunnel effect and undergo optical transition upon falling to a lower energy state E_{C1}, emitting a photon in the process. After photon emission, the electron is rapidly extracted from the E_{C1} state to be injected into the excited state of the following period, where another optical transition occurs. This process is called the cascade effect. With this technique, a single electron can produce several photons, making it more efficient than the other laser schemes presented in Figure 1.3.

Population inversion is a necessary condition to achieve laser effect. At the level of the radiative transition, the lifetime of the electrons in the excited state must be longer than the electrons' lifetime at the lower energy states. Section 1.2.1 presents the typical active region designs that allow obtaining population inversion.

Despite the successful demonstration of laser action in a QCL, the design presented issues that restricted its operation to cryogenic conditions, namely the non-radiative scattering losses, the free carrier absorption and the thermal backfilling of the lower laser level. The non-radiative scattering was dominated by the thermally activated phonons produced when electrons emit a longitudinal optical (LO) phonon rather than

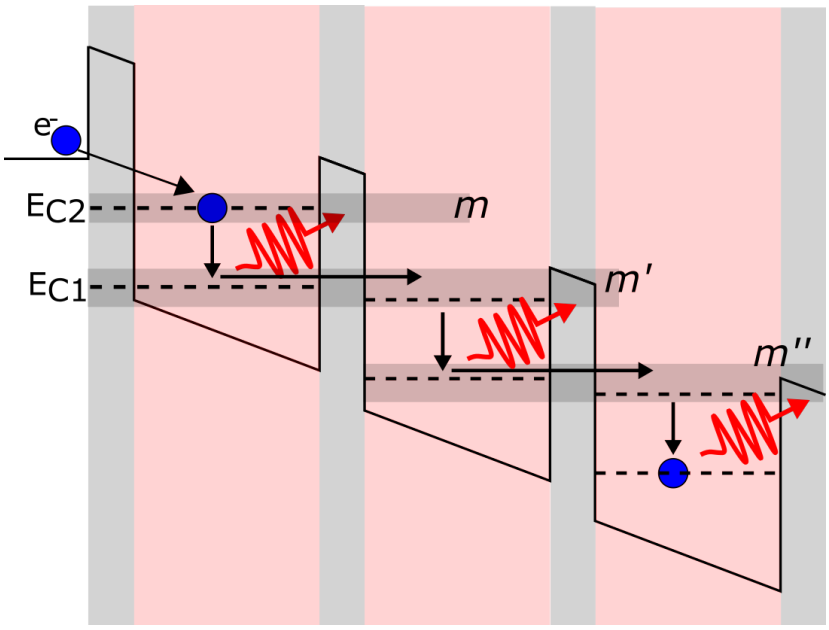

Figure 1.4: Schematic representation of the operating principle of a QCL. Red areas represent the quantum wells and gray areas the barriers. Arrows indicate the movement of electrons through the material. An electron is injected into the excited state E_{C2} contained in a miniband m (gray-shaded area) and undergoes optical transition by decaying to a lower energy state E_{C1} of a miniband m'. Photons are emitted in every stage (red curved arrow). After every emission, electrons tunnel to the next QW where another optical transition happens.

a photon when they decay from E_{C2} to E_{C1}. This reduces the population inversion between the two energy levels, thus decreasing the gain. Thermal backfilling refers to the process when electrons are thermally excited to the lower state E_{C1} from the injection region. This again reduces the population inversion and the overall gain. Further improvements in the QC design made possible the demonstration of the first QCL operating at room temperature in the Mid-IR [73]. To date, QCLs are the best performing semiconductor lasers in the Mid-IR, with devices outputting Watt-level power in cw operation at room temperature [74]. It was not until 2002 that the first QCL emitting in the THz range was demonstrated by Köhler et al [54]. It consisted of a GaAs/AlGaAs heterostructure emitting at 4.4 THz with an output power of 2 mW operating with a maximum temperature of 50 K in pulsed mode. Since then, continuous development in THz QCL designs have led to remarkable performances in terms of spectral coverage (1 to 5 THz), output power (>1 W in pulsed mode [55] and 0.2 W in cw [60]) and temperature performance (250 K [57]).

1.2.1 Active region designs

The most important tasks that an active region must simultaneously accomplish are to obtain a population inversion and to make the gain balance waveguide and other active region losses. An active region consists of two different zones: a gain region, which is in charge of creating and maintaining a population inversion between

two energy levels composing a radiative transition; and the injection region, designed to efficiently transport electrons from one gain region to another. These regions are schematically depicted in Figure 1.5. The gain and the injection regions constitute a period of the active region.

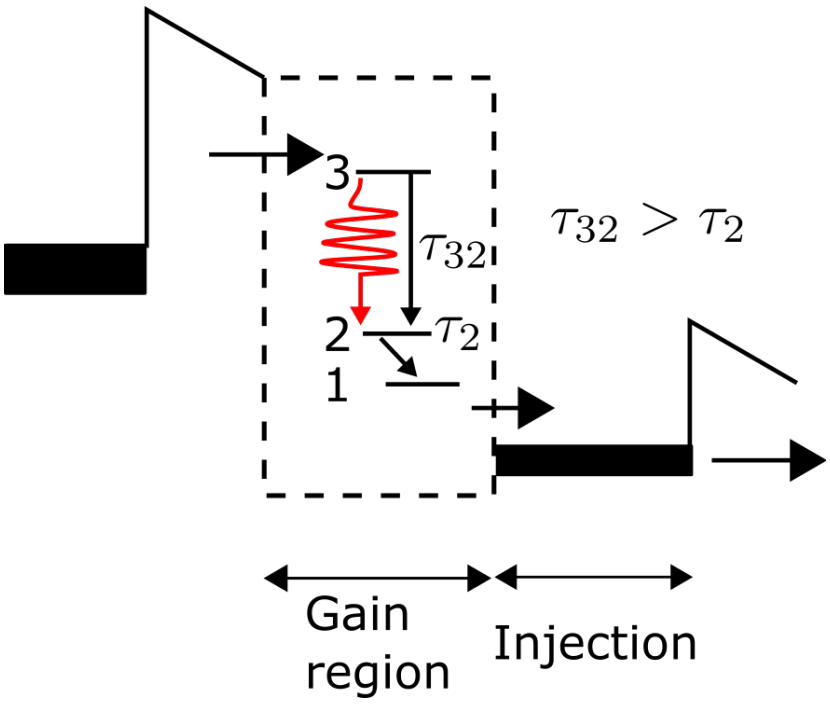

Figure 1.5: Conduction band diagram of a QCL containing 3 energy states. Adapted from [75].

Figure 1.5 shows an active region with three energy states. In this picture, electrons are injected by resonant tunneling into the $n = 3$ state and a population inversion is maintained between the $n = 3$ and $n = 2$ states defining the radiative transition. The population inversion condition is met when the lifetime of the lower-state τ_2 is shorter than the electron scattering time from the $n = 3$ to the $n = 2$ levels:

$$\tau_{32} > \tau_2 \tag{1.2}$$

An injection region follows the gain region. This enables electron injection by resonant tunneling into the next period. This is achieved by a series of alternating quantum wells and barriers with varying duty cycles.

The next sections will introduce two of the most common active regions designs utilized in THz QCLs: bound-to-continuum and resonant LO-phonon. The first of them involves a radiative transition between a continuum state (miniband) and an isolated state, where the continuum provides an effective method to achieve population inversion. The second design is based on a depopulation mechanism of the lower state of the lasing transition by emission of LO optical phonons.

Bound-to-continuum

Figure 1.6 illustrates the bandstructure of a QCL with a bound-to-continuum active region design. The system is based on a GaAs/$Al_{0.1}Ga_{0.9}As$ heterojunction material system emitting at 2 THz, conceived by Worral, et al. [76]. In a bound-to-continuum scheme, electron transport in between periods is carried out by minibands. In the figure, minibands are depicted in green shaded areas. The upper level of the radiative transition (indicated in red and labeled as 2 in the figure) consists of an isolated state decoupled from an upper miniband. This state is populated via resonant tunneling from a miniband's ground state g across a 5 nm $Al_{0.1}Ga_{0.9}As$ barrier. The lower energy state of the radiative transition (indicated in red and labeled as 1 in the figure), corresponds to the top energy state of another miniband spanning an energy range of 14 meV. The miniband allows the fast depopulation of the lower state of the radiative transition via elastic scattering processes, allowing population inversion. Also, this active region presents a reduced thermal backfilling, therefore good operational temperatures and output powers can be achieved with this design.

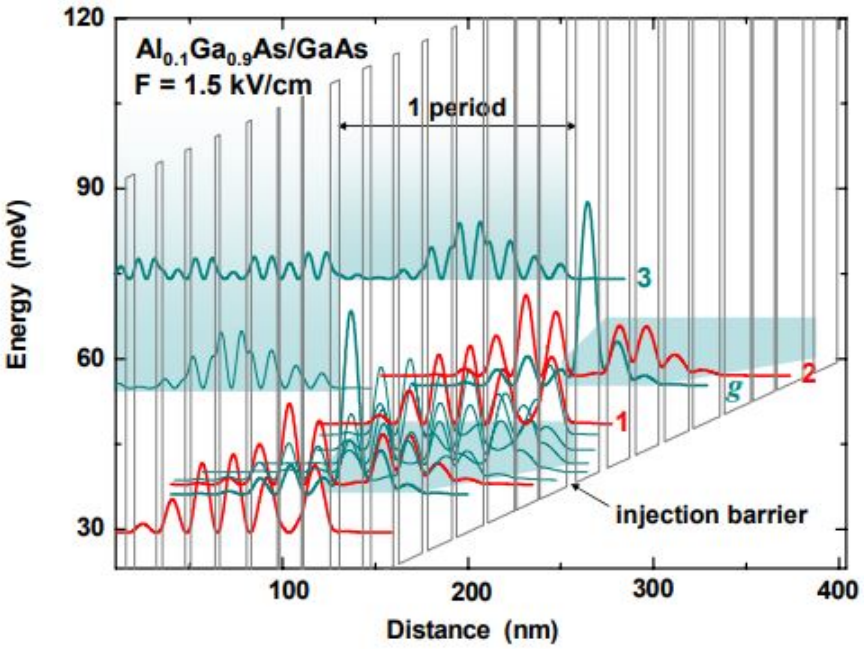

Figure 1.6: Band structure of 1 period of a bound-to-continuum active region design. Green shaded areas represent superlattice minibands. Representative moduli squared wavefunctions are also indicated. Thick red lines (1) and (2) represent the wavefunctions forming the lower and upper states of the radiative transition. Injection of electrons into level (2) is carried out by resonant tunneling from the state g (thick green line) across an injection barrier. Taken from [76].

Resonant LO-phonon

Figure 1.7 presents the band structure of a QCL with an active region based on a LO-phonon depopulation scheme realized by Luo, et al. [77]. In this example, the system is based on a GaAs/$Al_{0.15}Ga_{0.85}As$ heterojunction material system lattice emitting at 3.4 THz. Resonant LO-phonon active regions rely on LO-phonon emissions to quickly depopulate the lower state of the radiative transition. In this design, electrons in injector level (1') are injected into the upper state (4) via resonant tunneling. Electrons here undergo a radiative transition to the lower level of the radiative transition. Then, electrons decay to an energy state (1) placed $\sim$ 36 meV below the lower energy state. This energy difference matches the LO-phonon in GaAs, therefore providing a fast scheme for depopulation of the bottom energy state of the radiative transition. The advantage of this design is that as temperature rises, the LO-phonon population increases, stimulating more electrons to decay from the lower state. However, to create this energy difference, typically a greater external voltage is required to initiate lasing action.

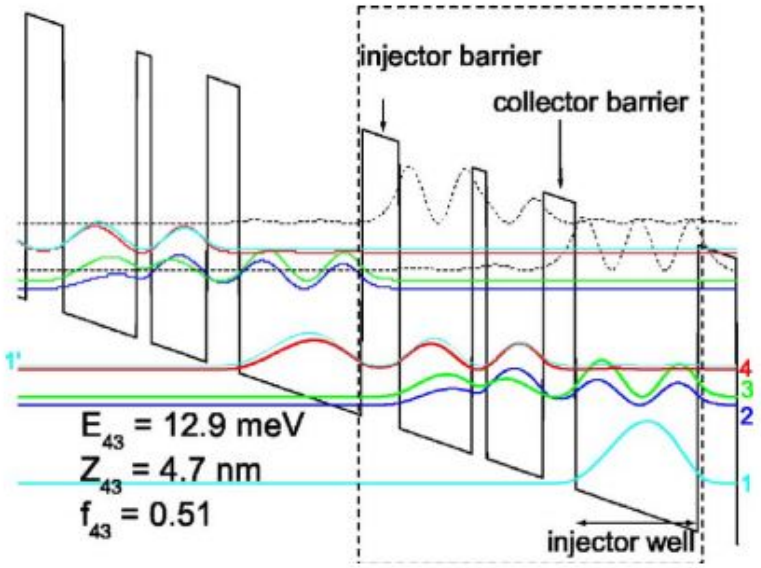

Figure 1.7: Band structure of 1 period of a resonant LO-phonon active region design. Taken from [77].

1.2.2 Waveguides and resonators for THz QCLs

There are two fundamental elements that lasers are composed of: a gain medium and a cavity for optical feedback. In a QCL, the active region provides the gain resulting from the stimulated emission of photons. An optical cavity is formed by etching into the active region material a waveguide structure, and serves two purposes: to confine photons providing mode overlap with the gain medium while granting optical feedback, thus allowing light amplification.

There are two types of waveguides used in THz QCLs: semi-insulating surface plasmon (SI-SP) and double metal (DM) waveguides, both depicted in Figure 1.8. The most common geometry design of a THz QCL waveguide consists of a ridge-shape Fabry-Pérot cavity. This cavity is formed by cleaving the ends of the semiconductor device, forming two parallel facets on either end of the waveguide. Typical dimensions for these waveguides lie in the order of a few hundred μm to a few mm for the length, few tens to a few hundred μm for the width and the thickness is determined by the size of the active region ($\sim$ 10 μm).

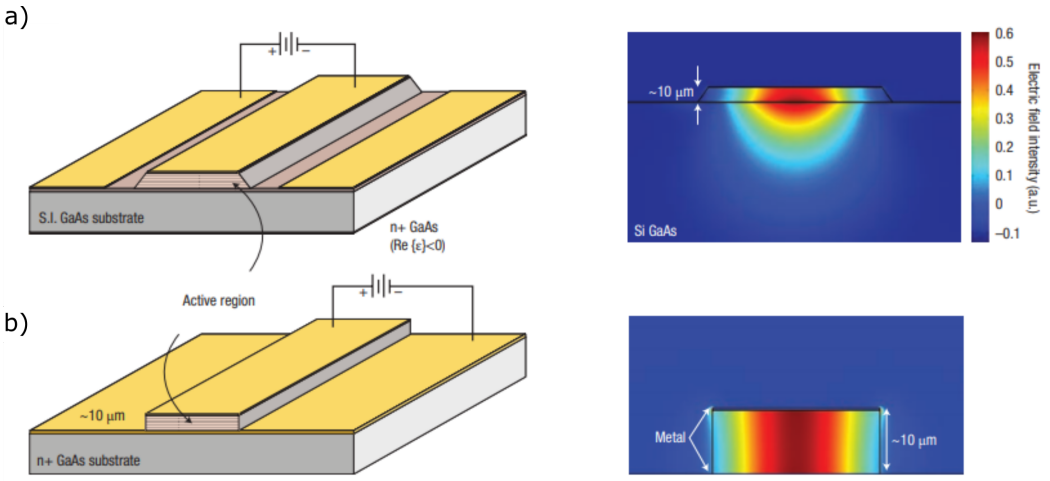

Figure 1.8: THz QCL waveguides. Left panels show an schematic diagram of a waveguide design in a) SI-SP configuration and b) DM configuration. At the right, lateral views of the mode intensity patterns for each waveguide are illustrated. Taken from [78].

The parameters impacting the performance of the waveguide are given by the waveguide losses α_w, referring to the scattering and absorption inside the waveguide, the mirror losses α_m, which accounts for the optical losses due to the finite reflectivity of the facets, and the confinement factor Γ, defined as the spatial overlap of the mode with the active region. The role of the waveguide is to optimize the overlap between the optical mode and the active region while minimizing losses. This determines the threshold current of the device, which is defined by:

$$J_{th} = \frac{\alpha_w + \alpha_m}{g_{th}\Gamma} \tag{1.3}$$

where g_{th} is the gain necessary to reach the lasing threshold.

Semi-insulating surface plasmon waveguides

In a SI-SP waveguide, depicted in Figure 1.8 a), the optical mode is confined between a highly doped semiconductor layer (at the bottom of the active region) and a top metal contact (typically gold). Surface plasmons are generated at the metal-semiconductor interface. A surface plasmon is an electromagnetic oscillation which

appears at the boundary between two media with dielectric functions $\epsilon = (n + ik)^2$ of opposite signs. The surface plasmon mode decays exponentially in both media. The decay length in the metal is extremely short owing to the large imaginary component of the refractive index at THz frequencies; whereas in the semiconductor side the mode decays less rapidly and extends substantially into the substrate. This produces a reduced confinement factor, which lies typically between Γ = 0.1-0.5, producing modes loosely confined [78]. The main advantage of this waveguide is that the extended intracavity mode at the facet eases the coupling to free space modes yielding a good far-field.

Double metal waveguides

Figure 1.8 b) presents a DM waveguide design. Here, the highly doped layer is substituted by a metal layer, fully confining the optical mode to the active region, then obtaining confining factors $\Gamma \approx 1$. With this type of guide, the best temperature performances have been demonstrated. The strong mode confinement makes it possible to reduce both lateral and vertical dimensions of the cavity to subwavelength scales. This makes the DM configuration attractive to achieve a strong light-matter interaction between the photons trapped within the waveguide cavity and the active region [79]. Furthermore, the resulting subwavelength-sized waveguide cavity induces an increase in the reflectivity of the facets linked to the impedance mismatch between the intracavity mode and the free space mode. As a result, DM waveguides have low mirror losses that allow a lower threshold current J_{th} to be obtained, favoring operation at high temperatures. However, the subwavelength nature of DM waveguides comes at the cost of poor optical outcoupling efficiencies and a strong divergence of the beam.

A simple approach to mitigate this effect is to attach a silicon hyperhemishperical lens at the facet of the DM waveguide to collimate the beam [80]. This, however, involves the addition of bulky components requiring careful alignment, making this approach largely impractical for applications. Other techniques, offering an integrated solution for beam optimization relies on cavity engineering beyond the basic Fabry-Pérot configuration. For example the integration of planar horn-type shape structures [81], waveguides incorporating distributed feedback gratings [82], photonic crystals [83], metasurfaces [84], micro-ring resonators [85], and antenna-coupled structures [86].

1.2.3 Antenna-coupled THz QCLs

Antenna-coupled THz QCLs are directly inspired from microwave engineering techniques by integrating antennas into QCLs designs. The versatility of antennas to in- and out-couple radiation offers multiple degrees of freedom to optimize the radiated beams, especially when arranged into arrays. Arrays of DM microcavity antennas loaded with a QC gain material significantly increase the effective aperture radiation area of a QCL, thereby providing a better far-field profile and improving the power extraction efficiency. Figure 1.9 a) shows a phase-locked array of subwavelength short-cavity surface-emitting THz QCLs, from Kao et al. [86]. In this work, phase-locking of all the laser elements is achieved by the antenna effect of mutual coupling through far-field interactions. This allows a long coupling range spanning over $\sim 8\ \lambda_0$ resulting

in the coherent interaction of 37 laser elements producing single mode radiation at 3 THz with a beam divergence better than 10° × 10°.

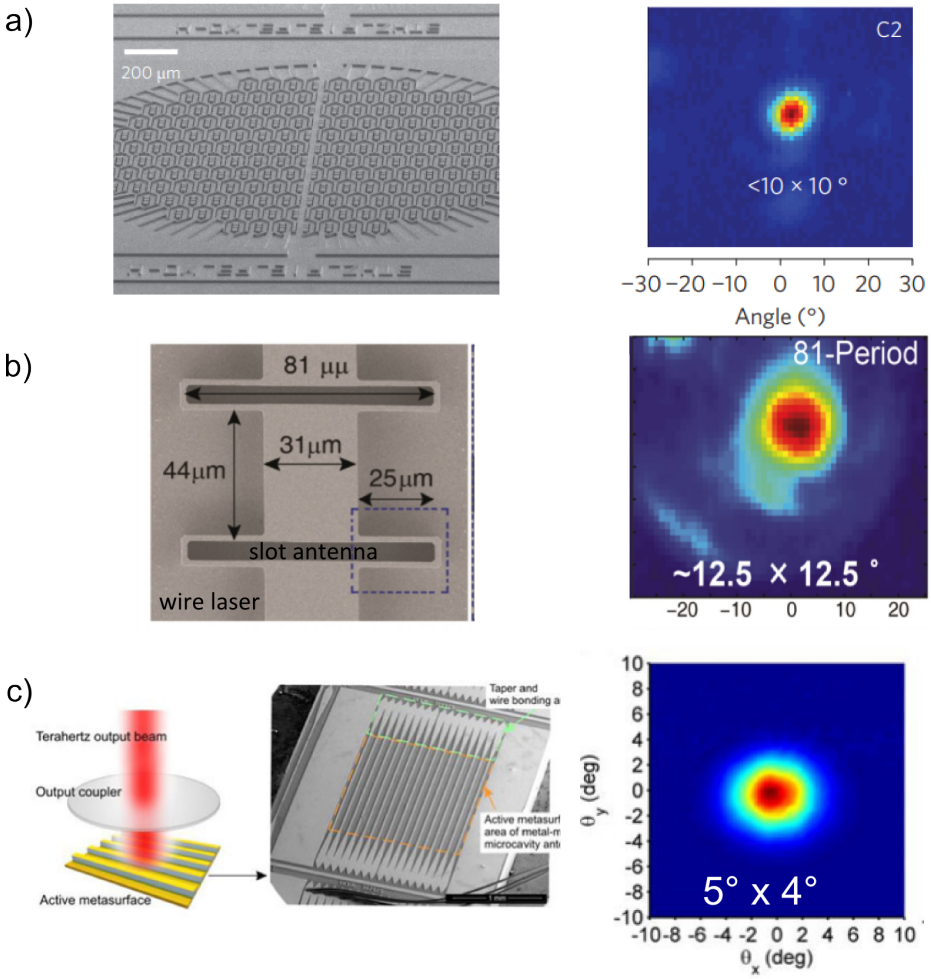

Figure 1.9: Antenna-coupled resonators for THz QCLs. SEM image (left) and measured far-field pattern (right) of a) a phased-locked array of subwavelength short-cavity surface-emitting THz QCLs [86], b) antenna coupled photonic wire lasers [87] and c) terahertz metasurface QC VECSEL [19].

Antenna-coupled cavities have been also used in photonic wire lasers QCLs. An example is presented in Figure 1.9 b). Wire lasers are characterized by having a deep subwavelength cross section, then producing strongly divergent and asymmetric beam profiles. By coupling slot antennas to an array of wire laser waveguides, a distributed feedback laser is created. Slot antennas create additional paths for electromagnetic energy to transmit from one wire segment to another, serving as both feedback enhancers and radiation emitters. By optimization of physical dimensions and array parameters, Kao et al. demonstrated shaping of the beam into narrow symmetric profiles with divergence $\sim 12.5° \times 12.5°$ emitting at 4 THz [87].

Another successful implementation of antenna-coupled QCLs is the metasurface reflectarray approach engineered by the group of B. Williams at UCLA [16–19]. The cavity design is composed of an array of DM ridge waveguides containing a QC material

paired with an external output coupler, forming a THz QC vertical-external-cavity surface-emitting laser (VECSEL). A schematic of this design is shown in Figure 1.9 c). Every ridge acts as an elongated patch microcavity to couple THz in the surface direction. When the structure is electrically biased, the emitted THz reflects back to the array and is amplified by stimulated emission in the QC active region. The amplified version of the THz signal is then re-radiated back into free space through the output coupler. Given that the metasurface's size is in the millimetre scale, high-power, directive and near-diffraction-limited beams can be achieved [17]. However, the additional size and complexity of an external cavity detriments the suitability of these devices for applications.

Another versatile antenna structure is the patch antenna. Arrays of patch antennas have impacted modern telecommunications in the RF range significantly, owing to their versatility in tailoring the properties of the emitted radiation such as beam width and polarization, along with their ease of fabrication. In this thesis, we make use of this antenna geometry to implement a patch antenna microcavity THz QCL. The next chapter presents an exhaustive description of the patch antenna. Following, chapter 3 addresses a methodology for implementing this antenna structure into THz QCLs.

1.3 Summary

The beginning of this chapter served as an introduction to the terahertz range. Section 1.1 reviewed the main characteristics of terahertz waves, the research opportunities and the available sources granting access to the THz range. Then, section 1.2 presented the basic concepts and principle of operation of terahertz quantum cascade lasers. A variety of different waveguides, resonators and active region designs were discussed. Lastly, special attention on antenna-coupled resonators for THz QCLs was given in section 1.2.3, introducing for the first time in this thesis the patch antenna concept.

Chapter 2

Patch Antenna Microcavities

This chapter introduces the fundamental building block of our device: the Patch Antenna Microcavitiy. The chapter begins with a brief review of the use of patch antennas in different spectral regimes. It follows with a summary of the two most popular models used for describing the radiation properties of patch antennas. Although originally developed for treating patch antennas in the RF regime, we will see that one of those models, the *cavity* model, provides a useful approach to understand and analyze patch antennas at THz frequencies. Next, we present a study of how the different contributions of the losses in arrays of antennas can be controlled by the array geometrical parameters, allowing to engineer photon extraction efficiencies. The last section presents a study of the influence of interconnecting wires in arrayed patch antenna microcavities via numerical simulations.

2.1 Patch Antennas

Microstrip lines were first proposed in the 1950s by Deschamps and Sichak [88] as an attempt to devise a feeding system solution less bulky than conventional waveguiding structures in the RF. The microstrip line was a variant of the "wire above ground" transmission line adapted to microwaves, and consisted of a strip made from a conductor material printed on a dielectric sheet backed by a ground metallic plane. The design not only succeeded in reducing size, weight and cost of microwave systems, but also allowed the easy integration of various circuitry elements of a communications system on a commonly printed circuit board. This work set the foundations for a new way of thinking about novel antenna structures based on microstrip lines. Years later, pioneering works utilized the microstrip line technology to demonstrate the first microstrip patch antennas [89–91]. Since this demonstration, patch antennas have been one of the most widely used and studied class of antennas in the RF.

A patch antenna is a simple antenna design consisting of a metallic 'patch' printed on a dielectric substrate of thickness $L \ll \lambda$ mounted over a large metallic ground plane, where λ is the operating wavelength. The patch geometry can come in various shapes and sizes, among which the rectangular, square and circular patches are the most commonly used. The size of the patch is designed such that the structure is resonant with a specific operating frequency. One of the most prominent characteristics of patch

antennas is their versatility for manipulating the characteristics of the emitted beams. Through its geometry, multiple properties such as resonance frequency, polarization, impedance and bandwidth can be controlled. Also, patch antennas implemented in arrays provide additional degrees of freedom to tailor the emission characteristics. Recently, patch antennas have also served as inspiration in the optical regime to design practical devices when combined with functional materials. The wave-matter interaction at optical frequencies at the interface between the metallic patch and the dielectric manifests itself as a surface plasmon polariton (SPP) wave [92, 93]. Because of this characteristic, patch antennas are also commonly known as plasmonic nanoantennas [94]. The success of their implementation in the optical range resides in the resulting *micro*-cavity formed below the patch. This provides strong field confinement and enhanced light-matter interaction localized at the nano-scale in combination with an efficient light harvesting and efficient light out-coupler element from the antenna counterpart. As a result, plasmonic patch antennas have been used to achieve photonic devices with a high degree of beam control and collection efficiencies for intra- chip communications and sensing [95, 96], emitters with controllable spontaneous emission [97], perfect absorbers [3], plasmonic devices with spectral tunability [98], mid-IR detectors with room temperature operation [7] and single photon sources with enhanced Purcell factors [99]. In the THz range, patch antennas have also been used for fundamental studies of the ultra-strong light-matter coupling regime [8], for phase-shaping metamaterials [9], perfect absorbers [100] and detectors with detectivity levels compared to commercial bolometers [101], and in combination with external cavities to achieve THz VECSELs [102].

There exist various methods of analysis and design of microstrip patch antennas. The most common ones are the *transmission-line* [103, 104] and the *cavity* models [105, 106]. Both provide good physical insight and analytic expressions which relate the geometric elements of the antennas with their radiation properties. While both models were originally developed for the RF, they have been used as well at optical frequencies as a starting point for the design and analysis of plasmonic nanoantennas [107, 108]. In this thesis, we use patch antennas of square shape in the THz domain. In this regime, metals do not behave as perfect electric conductors (PEC), as assumed in the transmission line and cavity models at microwave frequencies. The electric field penetrates in metals, generating non-negligible Ohmic losses and directly impacting the extraction efficiencies of the devices. However, a useful glimpse into the physics of patch antennas and good prediction of their behavior in the THz can be obtained with the transmission-line and cavity models. In the next sections, we will summarize the most relevant aspects of the two models and will provide a treatment of the losses in THz patch antennas by using full-wave finite element simulations.

2.1.1 Transmission-line model

This section introduces the transmission-line model for rectangular patch antennas. A typical patch antenna, as shown in Figure 2.1 (a), consists of a rectangular metallic patch of length s and width W placed over a substrate with a thickness of a small fraction of a wavelength ($L \ll \lambda_0$) above a ground plane. The patch antenna radiates in broadside direction (radiated field propagates in the direction perpendicular to the

patch surface.) due to the fringing fields originated at the sides of the antenna. The transmission-line model, as depicted in Figure 2.1 (b), represents the patch antenna by two radiating aperture slots (sides) separated by a low impedance Z_C transmission line of length s, where every aperture slot is modeled by a parallel equivalent admittance $Y_i = G_i + jB_i$.

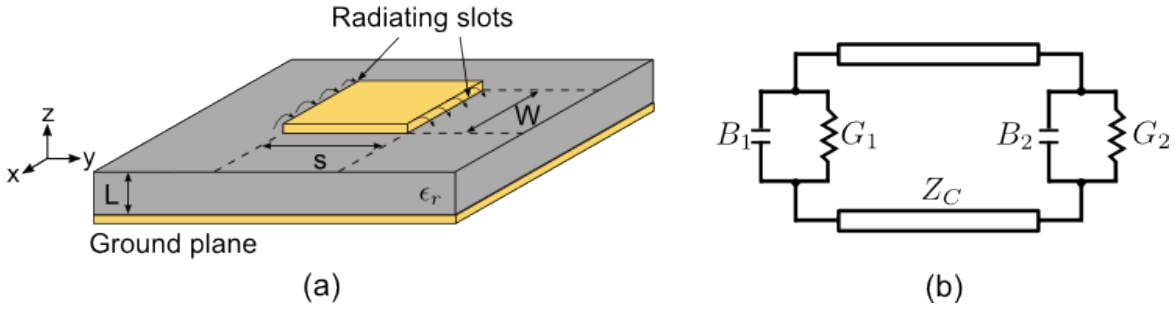

Figure 2.1: Microstrip patch antenna diagram. (a) Geometry (b) Equivalent transmission line model.

Because of the symmetry of the model, both slots are identical, then $Y_1 = Y_2$, $G_1 = G_2$ and $B_1 = B_2$. In general, the resistive part of the equivalent admittance consists of two components:

$$\frac{1}{G_i} = \frac{1}{G_r} + \frac{1}{G_L} \tag{2.1}$$

where $R_r = \frac{1}{G_r}$ represents the radiation resistance of the antenna and $R_L = \frac{1}{G_L}$ the loss resistance of the antenna. The resistive part of the antenna defines its radiation efficiency e_{cd}, which can be expressed as[109] :

$$e_{cd} = \left[\frac{R_r}{R_L + R_r}\right] \tag{2.2}$$

Specific expressions for the conductance G and susceptance B for the patch antenna geometry are given by [109]:

$$G_1 = \frac{W}{120\lambda_0}\left[1 - \frac{1}{24}(k_0 L)^2\right] \tag{2.3a}$$

$$B_1 = \frac{W}{120\lambda_0}[1 - 0.636\ln(k_0 L)] \tag{2.3b}$$

The expressions in (2.3) relate the geometric parameters of the patch with its equivalent admittance. These expressions can be useful to characterize quantitatively the mutual coupling between different patch emitters for example when they are arranged in arrays [110].

Another relevant characteristic of patch antennas, is that the electric field undergoes fringing at the edges. Because of the finite size of the structure, the electric field contained within the patch bends at the periphery, making the patch's electrical size

bigger compared to its physical size. To take into account this effect, an effective length of the antenna is introduced. This directly impacts the performance of patch antennas and it should be taken into account in a design procedure. The amount of fringing is directly related to the dimensions of the patch and the height of the substrate. For thicker substrates, the fringing spans greater lengths. Also, electric field lines are mostly contained within the substrate but also exist in the air. So, an effective dielectric constant needs to be defined. The effective dielectric constant of a rectangular patch antenna is given approximately by [111]:

$$\epsilon_{eff} = \frac{\epsilon_r + 1}{2} + \frac{\epsilon_r - 1}{2} \frac{1}{\sqrt{1 + 12L/W}} \tag{2.4}$$

The length of the patch is extended by an amount Δs at each end, and is a function of the effective dielectric constant ϵ_{eff} and the width to height ratio W/L. A practical approximate relation for the calculation of Δs is given by [112]:

$$\frac{\Delta s}{L} = 0.412 \left(\frac{\epsilon_{eff} + 0.3}{\epsilon_{eff} - 0.258} \right) \left(\frac{W/L + 0.262}{W/L + 0.813} \right) \tag{2.5}$$

Then, the effective length of the patch is:

$$s_{eff} = s + 2\Delta s \tag{2.6}$$

By using equations (2.4) and (2.6), the resonant frequency of the dominant TM_{010} mode can be calculated, according to:

$$(fr)_{010} = \frac{c}{2s_{eff}\sqrt{(\epsilon_{eff})}} \tag{2.7}$$

It can be noted that the designed resonant frequency based on the fringing effect is lower as the patch looks longer.

The simplified formulation outlined can be used to elaborate a practical procedure for designing rectangular patch antennas.

2.1.2 Cavity model

A patch antenna can be considered as a dielectric-loaded cavity with dimensions slightly larger than the actual patch to account for the fringing fields, as shown in Figure 2.2 (a). The equivalent cavity is delimited by two conductive walls on the top and bottom and four walls at the edges of the antenna acting as aperture slots. The cavity model provides good physical insight into the antenna operation as it provides analytical expressions for the radiated and intracavity fields (intracavity fundamental and higher-order modes).

The cavity model makes two fundamental assumptions:

- Only z-component of the electric field exists
- Cavity walls are considered perfect magnetic conductors (PMC)

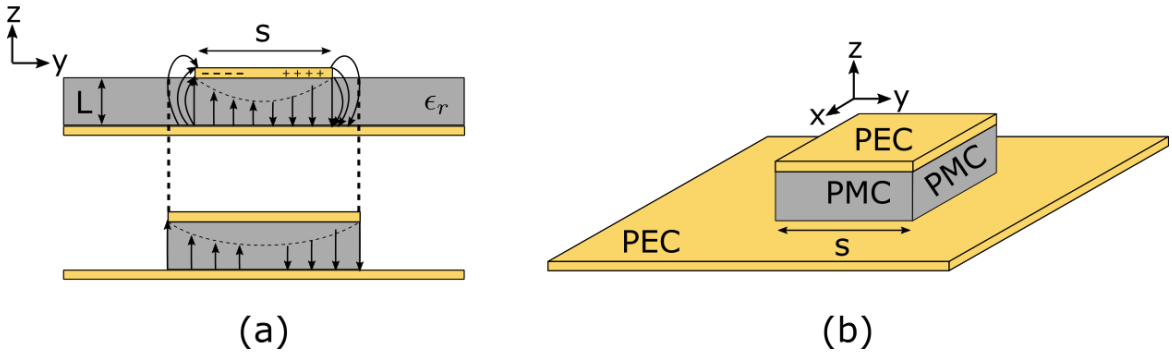

Figure 2.2: Cavity model. (a) Cross-sectional view of the equivalent cavity model of the patch antenna. (b) Patch antenna cavity with PMC walls at the edges and PEC at the bottom and top.

The first assumption is based on the fact that $L \ll \lambda_0$. When the waves traveling inside the dielectric cavity encounter the edges, considerable reflections are generated due to the impedance mismatch between the metal-dielectric-metal and single metal regions. Therefore, the field below the metallic patch form standing waves. Since we are considering a small cavity of subwavelength scales ($L \ll \lambda_0$), the modes with variations in the z-direction are not excited. Therefore, only transverse magnetic (TM^z) field distributions will be considered within the patch cavity.

The TM^z field distributions can be calculated by using the magnetic vector potential approach [113]. Since we will focus only on the z-component of the field, the vector potential A_z must satisfy the wave equation:

$$\nabla^2 A_z + k^2 A_z = 0 \tag{2.8}$$

The solution, by using separation of variables, can be written as:

$$\begin{aligned} A_z = &[C_1 \cos(k_x x) + D_1 \sin(k_x x)] \cdot [C_2 \cos(k_y y) + D_2 \sin(k_y y)] \\ &\cdot [C_3 \cos(k_z z) + D_3 \sin(k_z z)] \end{aligned} \tag{2.9}$$

where $k_x^2 + k_y^2 + k_z^2 = k^2 = \omega^2 \mu\epsilon$. The electric and magnetic fields within the cavity in

terms of A_z can be expressed as [113]:

$$\begin{aligned} E_x &= -j\frac{1}{\omega\mu\epsilon}\frac{\partial^2 A_z}{\partial x \partial z}, & H_x &= \frac{1}{\mu}\frac{\partial A_z}{\partial y} \\ E_y &= -j\frac{1}{\omega\mu\epsilon}\frac{\partial^2 A_z}{\partial y \partial z}, & H_y &= -\frac{1}{\mu}\frac{\partial A_z}{\partial x} \\ E_z &= -j\frac{1}{\omega\mu\epsilon}\left(\frac{\partial^2}{\partial^2 z} + k^2\right) A_z, & H_z &= 0 \end{aligned} \tag{2.10}$$

Now, we assume that the current density on the walls of the patch are negligible, then we set the tangential magnetic fields to zero (PMC condition). Also, it is assumed that the top and bottom plates of the cavity are perfect electric conductors. Therefore, we can express the boundary conditions of this system as:

$$\begin{aligned} H_y(x = 0, y = s) &= 0 \\ H_x(y = 0, y = W) &= 0 \\ E_y(z = 0, z = L) &= 0 \\ E_x(z = 0, z = L) &= 0 \end{aligned} \tag{2.11}$$

By applying the boundary conditions (2.11) into (2.9) and (2.10), we find the vector potential A_z to be:

$$A_z = A_{mnp}\cos(k_x x)\cos(k_y y)\cos(k_z z) \tag{2.12}$$

where

$$k_x = \frac{m\pi}{s}, \quad k_y = \frac{n\pi}{W}, \quad k_z = \frac{p\pi}{L} \tag{2.13}$$

A_{mnp} represents the amplitude of the modes excited in the cavity, k_x, k_y, k_z the wavenumbers and m, n and p are the number of half-cycles per mode in the x, y and z directions respectively. Under the assumption that modes varying along the z-direction are not excited, we can set $p = 0$. then, the field distribution under the patch cavity can be expressed as:

$$\begin{aligned} E_z &= \frac{-j}{\omega\mu\epsilon}\left[\left(\frac{n\pi}{W}\right)^2 + \left(\frac{m\pi}{s}\right)^2\right]\cos\left(\frac{m\pi}{s}x\right)\cos\left(\frac{n\pi}{W}y\right) \\ H_x &= -\frac{1}{\mu}\left(\frac{n\pi}{W}\right)\cos\left(\frac{m\pi}{s}x\right)\sin\left(\frac{n\pi}{W}y\right) \\ H_y &= \frac{1}{\mu}\left(\frac{m\pi}{s}\right)\sin\left(\frac{m\pi}{s}x\right)\cos\left(\frac{n\pi}{W}y\right) \\ H_z &= 0 \end{aligned} \tag{2.14}$$

Substituting the expression of the wavenumbers (2.13) into $k_x^2 + k_y^2 + k_z^2 = k^2 = \omega^2\mu\epsilon$, leads to the expression for the resonance frequencies of the patch cavity:

$$(fr)_{mn}^{TM} = \frac{1}{2\pi\sqrt{\mu\epsilon}}\sqrt{\left(\frac{m\pi}{s}\right)^2 + \left(\frac{n\pi}{W}\right)^2} \tag{2.15}$$

2.1.3 Radiated Fields

The walls on the periphery of the patch cavity can be thought of aperture slots from which radiation takes place. Every slot represents a source current with equivalent magnetic current density $\mathbf{M}_i = -2\hat{n} \times \mathbf{E}_i$. The radiated fields from each slot in the far-field can be calculated using the equivalent current densities $\mathbf{M}_i$ and the intracavity field modes given by (2.14). Referring to Figure 2.3 (a), for the dominant mode TM_{01} the equivalent magnetic current densities $\mathbf{M}$ at the slots located in the XZ-planes are of the same magnitude, direction and phase. Therefore, the radiation from these sources will add up in broadside direction (perpendicular to the patch). Owing to this fact, these slots are referred to as *radiating* slots. On the other side, the equivalent magnetic currents for the other two slots are of the same magnitude but with opposite direction (Figure 2.3 (b)). Then, their fields cancel each other in the far-field and there is no contribution to the total electric field from these slots. In view of this, they are named as *nonradiating* slots.

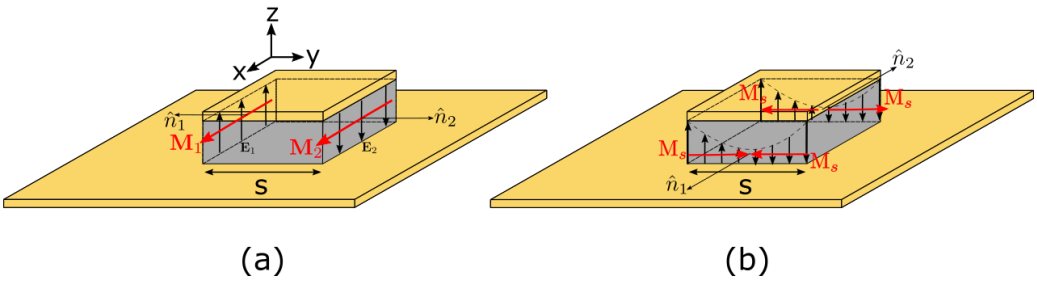

Figure 2.3: Current densities on aperture slots for the TM_{01} mode. Equivalent magnetic current densities at the slots aligned in the (a) $y-$ direction and (b) $x-$direction for the fundamental TM_{01} mode.

The electric fields radiated by each of the radiating slots is [109]:

$$\begin{aligned} E_r &\simeq 0 \\ E_\theta &\simeq 0 \\ E_\phi &= j\frac{k_0 LW E_0 e^{-jk_0 r}}{2\pi r}\left[\sin\theta \frac{\sin(X)}{X}\frac{\sin(Z)}{Z}\right] \end{aligned} \tag{2.16}$$

where

$$\begin{aligned} X &= \frac{k_0 L}{2}\sin\theta\cos\phi \\ Z &= \frac{k_0 W}{2}\cos\theta \end{aligned} \tag{2.17}$$

The slots on each side of the patch form a two-element array with a spacing of $s \approx \lambda/2$ between the elements. The total electric field produced by the two slots in

the far-field is the product of the field of a single element and its *array factor* (refer to section 2.2). According to (2.23), the array factor for an array of two elements placed along the $y-$ direction spaced by a distance s is:

$$(AF)_y = \cos\left(\frac{k_0 s}{2}\sin\theta\sin\phi\right) \tag{2.18}$$

Thus, the total electric field radiated by a patch antenna in the far-field is given by:

$$E_\phi^T \simeq j\frac{k_0 LW E_0 e^{-jk_0 r}}{2\pi r}\left[\sin\theta\frac{\sin(X)}{X}\frac{\sin(Z)}{Z}\right] \times \cos\left(\frac{k_0 s}{2}\sin\theta\sin\phi\right) \tag{2.19}$$

2.1.4 Field distribution and Radiation from Square Patch cavities

In this thesis, we study patch antennas of square shape ($W = s$). For this geometry, the fundamental TM_{01} and TM_{10} modes are degenerate, with resonant frequencies given by:

$$(fr)_{01,10}^{TM} = \frac{1}{2s\sqrt{\mu\epsilon_{eff}}} \tag{2.20}$$

As the lateral length of the patch is increased, the resonance frequency shifts towards lower frequencies. Emission spectra for different lateral lengths s are plotted in Figure 2.4.

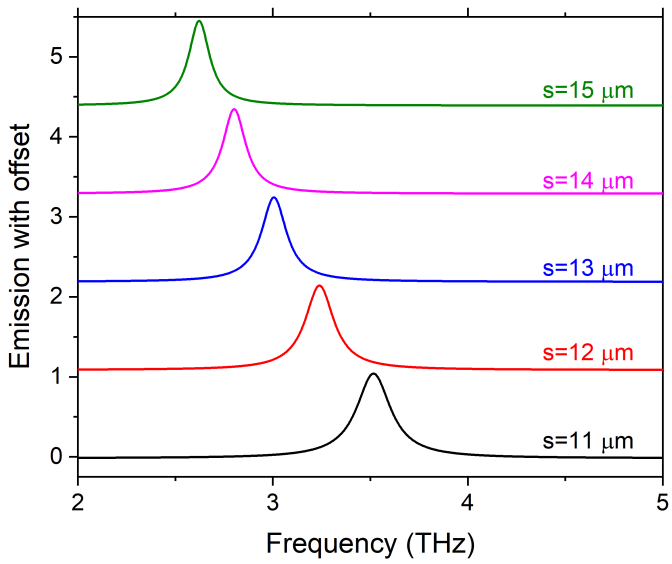

Figure 2.4: Simulated emission spectra of a square patch cavity. Spectra calculated for various s. Frequency shifts towards lower values as the size of s increases.

The electric fields of the degenerated TM_{01} and TM_{10} modes are cross-polarized,

and follow a cosinusoidal distribution approximated by:

$$(E_z)_{01}^{TM} \approx E_0 \cos\left(\frac{\pi}{s}y\right)$$
$$(E_z)_{10}^{TM} \approx E_0 \cos\left(\frac{\pi}{s}x\right) \tag{2.21}$$

The field distribution of these modes are depicted in Figure 2.5. The fundamental modes sustain half-wavelength oscillations in the $x-$ and $y-$ directions simultaneously. In section 2.4 it will be shown how the fundamental degenerated modes can be frequency-detuned. The controlled detuning allows the coherent the manipulation of the polarization states of the radiated fields by the patch antenna microcavity. An experimental demonstration of the polarization control will be shown in section 4.1.

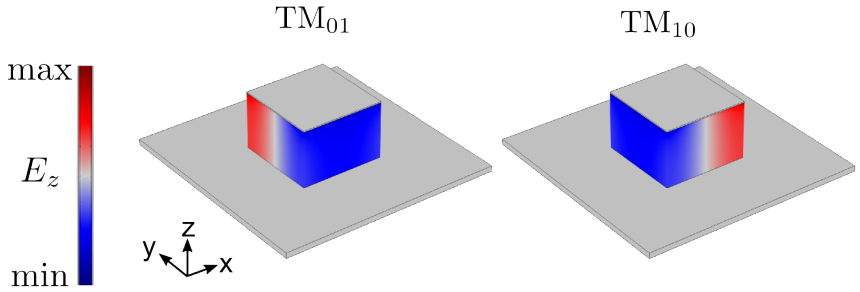

Figure 2.5: Square patch intracavity fields. The field distributions follows cosinusoidal behaviour. Only one cycle per mode is propagated in the cavity in the $y-$direction for the TM_{01} mode and in the $x-$direction for the TM_{10} mode. Color scale represents the amplitude of the electric field E_z.

To illustrate the usefulness of the cavity model for studying antennas in the THz regime, the 2D principal E-plane ($\theta = 90°$) pattern was calculated at $f = 3.2$ THz using (2.19); and was compared with full-wave numerical simulations. These are shown in Figure 2.6. As it is observed, there exists a good agreement between the simulations and the cavity model. For the simulation model, a square patch cavity (GaAs used as the dielectric filling material) was placed over a finite ground plane (refer to section 3.5.2 for a detailed description of the far-field simulation method).

2.2 Antenna Array Theory

In the RF and microwave bands, arrays of antennas are used to manipulate the transmitted or received signals for example by producing directive patterns or canceling out energy from undesired directions. These features have been exploited in modern communications systems to provide high degree control capabilities such as beam shaping, beam steering, enhanced gain, path diversity and direction-finding [114–116]. The mechanism enabling this handling of the field is the constructive and destructive interferences occurring in specific directions at the far-field. In general, for an array of antennas, there are five control parameters that can be used to construct these interferences:

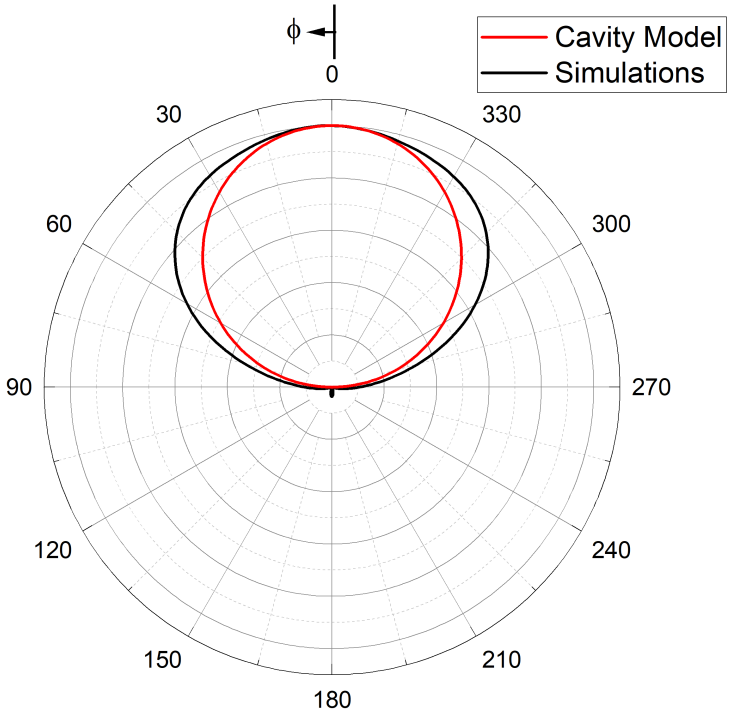

Figure 2.6: Cavity model vs Simulations. Normalized 2D patterns in the principal $E-$plane of a patch antenna in the THz regime ($s = W$ =15 μm, f =3.2 THz and GaAs as dielectric material).

1. the geometrical configuration of the array (linear, planar or circular array)
2. the total number of antennas composing the array
3. the distance between elements
4. the excitation amplitude of individual elements
5. the excitation of their relative phases

Given that the studied devices in this thesis are based on patch antenna arrays, the same analysis used in conventional microwave antenna theory can be used to understand the basic trend of the beam shaping from our microcavity structures. For an array of antennas, the angular distribution of the total emitted power in the far-field can be approximated by

$$P_{tot}(\theta, \phi) = P_0(\theta, \phi) \left|AF(\theta, \phi)\right|^2 \tag{2.22}$$

Here, P_0 corresponds to the power emitted from a single antenna element. The term following this quantity is known as the array factor, and it contains the dependence of the far-field emitted power on the array parameters. Considering a planar array formed by positioning individual antennas along a $M \times N$ rectangular grid, spaced by

distances d_x and d_y respectively, and assuming the same excitation (both magnitude and phase) for all the elements, the array factor takes the form [109]:

$$AF(\theta,\phi) = \left\{ \frac{1}{M} \frac{\sin\left(\frac{M}{2}\psi_x\right)}{\sin\left(\frac{\psi_x}{2}\right)} \right\} \left\{ \frac{1}{N} \frac{\sin\left(\frac{N}{2}\psi_y\right)}{\sin\left(\frac{\psi_y}{2}\right)} \right\} \tag{2.23}$$

where

$$\begin{aligned} \psi_x &= k d_x \sin\theta \cos\phi \\ \psi_y &= k d_y \sin\theta \sin\phi \end{aligned} \tag{2.24}$$

This simple model allows to intuitively understand the general trends and the influence of array parameters on the far-field. We used the array factor expression to investigate the main trend of the far-field pattern emitted by a planar array of antennas emitting at 3.2 THz (λ=94 μm). Figure 2.7 shows the calculated FWHM divergence angles for various arrays containing different number of elements M=N along the $x-$ and $y-$ direction (N=2,4,6,8 and 10) as a function of the separation distance between individual elements. The curves were extracted along the constant plane θ= 0 from the 2D array factor term. The FWHM divergence angle shows a monotonic decrease with the separation distance between elements, but as the number of elements N increases, a saturation of the divergence angle occurs.

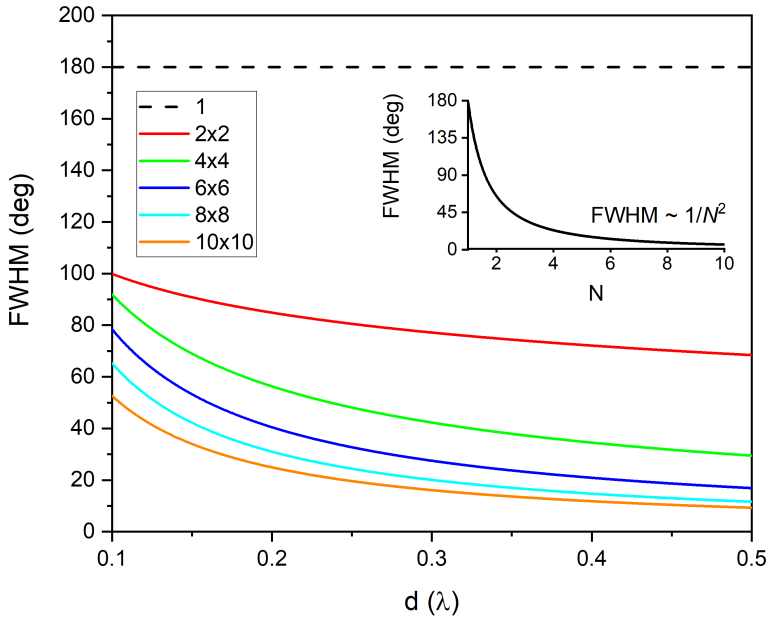

Figure 2.7: Divergence of planar arrays. FWHM divergence angles as a function of the separation distance between antennas calculated from the array factor term for planar arrays containing $N \times N$ elements (where N = 2,4,6,8 and 10). Dashed line represents the single element isotropic case. Inset: FWHM as a function of the numbers of elements for an array with elements distanced by a half wave.

2.3 Engineering the losses

Considering the patch antenna as a cavity with lossless upper and lowers bounds is insufficient to describe the behavior of the electromagnetic fields. An electrical equivalent of this approximation would correspond to a circuit with purely-susceptive admittances. By doing so, the antenna will not be able to radiate, as $R_r = R_L = 0$. To account for radiation, a lossy element should be included in the model. To describe the losses, an effective loss tangent δ_{eff} is introduced. The loss tangent will represent the loss mechanisms of the cavity, and it is defined as the inverse of the quality factor Q of the cavity: $\delta_{eff} = 1/Q$. To evaluate the losses in the system, we performed numerical simulations based on the finite element method [117] . The results of this numerical study are published in Dr. Madéo's work: *"Engineering the Losses and Beam Divergence in Arrays of Patch Antenna Microcavities for Terahertz Sources"*, Journal of Infrared, Millimeter, and Terahertz Waves 38, 1321-1330 (2017) [118].

First, to investigate the general trends of the losses in an array of patch microcavities, we performed 2D simulations, as the underlying physics can be captured accurately within this approximation. Also, previous work has demonstrated good agreement between experimental reflectivity spectra of patch antenna microcavity arrays and 2D simulations of infinite arrays [15]. Section 2.4.1 extends the treatment of the losses considering a more realistic 3D model.

The model for this study is shown in Figure 2.8. It consists of N identical resonators of thickness L separated a distance d. Every resonator is modeled with one dielectric (GaAs) and one metallic (Au) layer, placed over a ground metallic (Au) plane, all of them contained within an air domain half circle. Complex refractive indices we taken from [119]. Internal ports with TM polarization were placed in the boundary between the metallic and the dielectric layers to simulate the radiation from the structure. Radiation from the structures is collected by a second port placed at the circular boundary between the air half circle and a perfectly matched. layer. The length of every resonator was fixed to s= 10 μm, defining a resonant frequency of 3.8 THz.

In general, the different contributions to the total losses, in terms of the quality factor, can be expressed as:

$$\frac{1}{Q} = \frac{1}{Q_{rad}} + \frac{1}{Q_{nr}} \tag{2.25}$$

where Q refers to the total quality factor, and Q_{rad}, Q_{nr} are the quality factors associated to the radiative and non-radiative losses.

First, numerical simulations were performed to obtain the total quality factors for different arrays (various N) with three different resonator thicknesses L = 1, 2 and 5 μm, and compared them to the single resonator case. Quality factors were obtained by simulating the transmission spectra and by fitting then with a Lorentzian curve. Figure 2.9 (first row) shows the main results of the simulation study. In the big picture, the quality factors for all the cases are similar and follow an analogous trend: increasing Q for larger separation between elements d. For all the cases, the array quality factors for arrays with $d \leq 20\mu$m are lower than for the single resonator case. This is attributed to a strong inter-element coupling, known to have an enhancement effect in the fractional bandwidth for arrays with elements spaced by $d \leq \lambda/4$ [120]. For $d \geq 20$ μm, the array

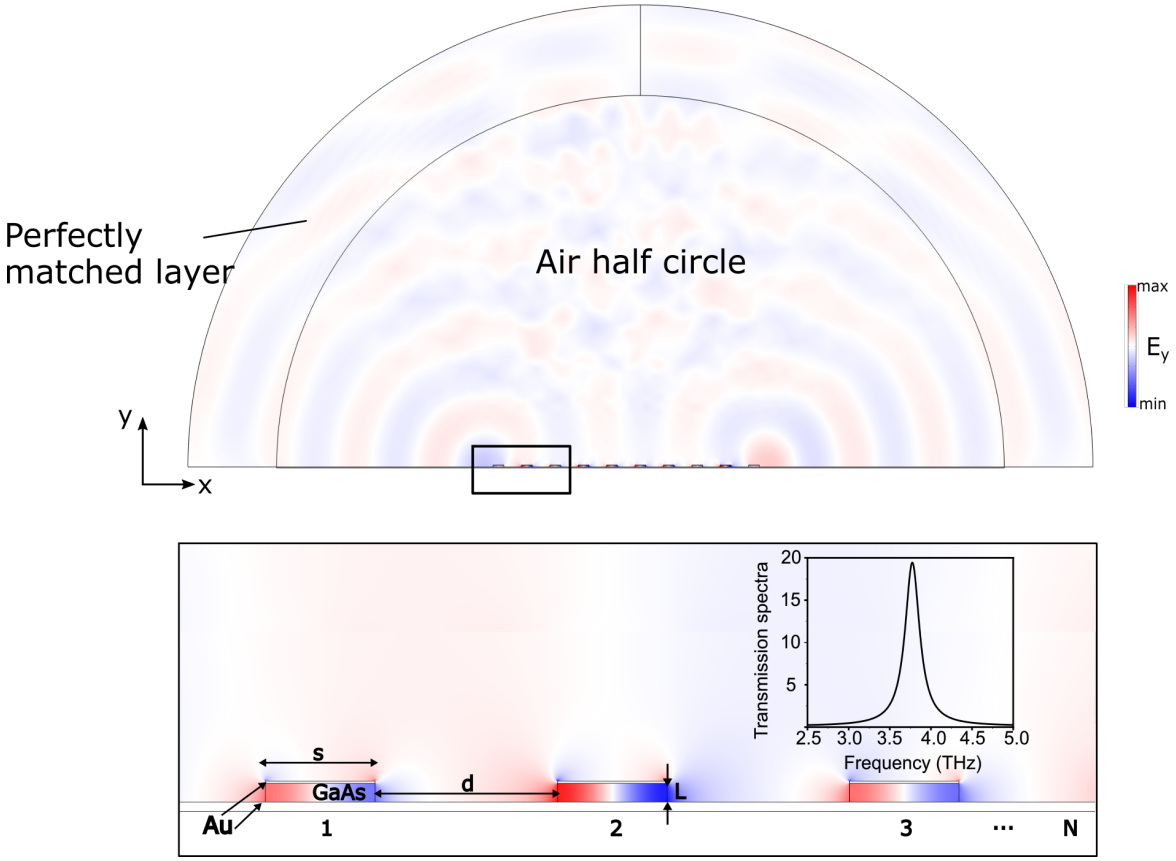

Figure 2.8: 2D simulation model. Model consists of a half circle air domain containing a linear array of N patch antenna microcavities of length s composed of GaAs domains bounded by two Gold layers. Color code represents the mode intensity. Inset: transmission sepctrum.

provides greater quality factors (smaller losses) than for a single resonator. The highest quality factor is obtained for arrays with elements of thickness $L = 2\mu$m, because at this thickness the radiative and non-radiative losses are balanced.

A deeper insight into the losses of the system can be obtained when examining the different contributions to the total losses. In the simulations, when we replace the lossy metallic plates by perfect conductors, we can extract the radiative and non-radiative contributions. The second row of Figure 2.9 displays the total quality factors and the radiative and non-radiative contributions for an array of N=10 resonators. We can distinguish three different regimes. For L= 1 μm, the mode is tightly confined into the cavity, then the electric field strongly overlaps with the lossy metallic layers. A result, Q_{rad} is always higher than Q_{nr} so the total contributions are dominated by non-radiative losses. The opposite case takes place when L= 5 μm. It is observed that there is no dependence of the non-radiative losses with the distance between resonators. Further, the large thicknesses of the structures lead to better coupling of the confined modes with the radiated modes. Then, the system is dominated by its radiative losses. Finally, a thickness of L= 2 μm corresponds to an intermediate regime. In this case, both contributions have similar magnitudes, and by tuning the period of the array, the

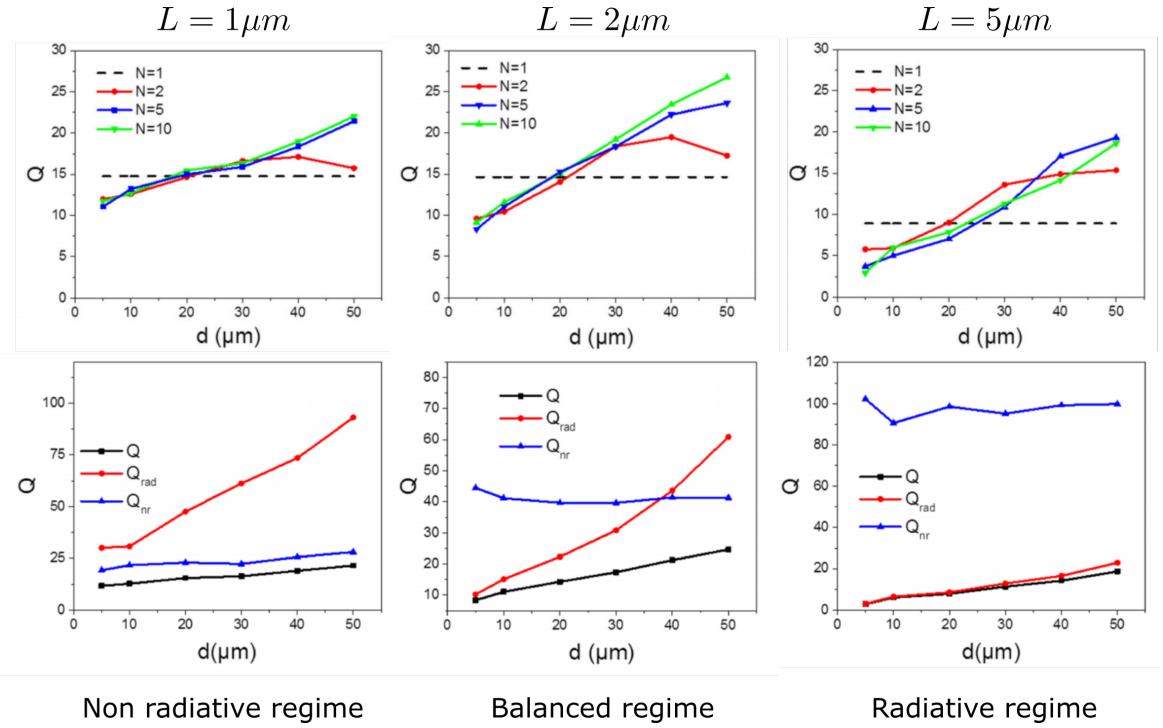

Figure 2.9: Quality factors vs distance between resonators. First row: quality factors of the system as a function of the separation distance d between resonators for various N. Second row: comparison between total, radiative and non-radiative quality factors vs d for an array with $N = 10$ elements. Plots taken from [118] .

radiative and non-radiative losses can be perfectly balanced.

Another relevant quantity to consider is the photon extraction efficiency η, defined as:

$$\eta = \frac{Q}{Q_{rad}} \tag{2.26}$$

This quantity provides the ratio of photons that can escape the resonator. In Figure 2.10, this quantity is plotted for the case of N=10 and various L= 1, 2 and 5 μm. Overall, it can be seen that increasing the thickness of the substrate leads to higher extraction efficiencies. In fact, this could be inferred from the previous results, since we observed that in the case of L=5 μm the radiative losses dominate. Conversely, lower extraction efficiencies are calculated for extended arrays, in account of the increase of Q_{rad} with d, as demonstrated in Figure 2.9. For denser arrays, the photon outcoupling gets higher due to larger radiative losses. Extraction efficiencies as high as $\eta \sim 90\%$ can be obtained for example, with a device with an active region of L= 5 μm and an array with d= 20 μm which presents an out-coupling efficiency above 90% which is much higher than what can be achieved with metal-metal planar waveguides [121].

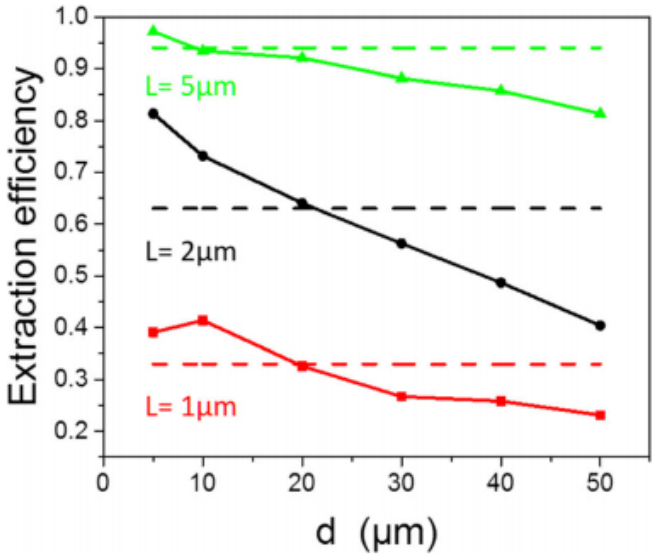

Figure 2.10: Photon extraction Efficiencies. Calculated photon extraction efficiencies as a function of d compared to a single resonator case (dashed lines) for arrays of N= 10 elements and varied L. Plot taken from [118] .

2.4 Arrays of Patch Antenna Microcavities coupled with plasmonic wires

Arrays of RF patch antennas are the most widely used antenna configuration in modern telecommunication systems as they offer a flexible platform to send, receive and manipulate electromagnetic waves [122, 123]. High degree control capabilities such as beam shaping, beam steering, enhanced gain, path diversity and direction finding are some of the achievable features offered by patch antenna arrays [114–116].

To mimic in the THz range the control features demonstrated in the RF, we use in this thesis arrays of square patch antennas adapted to this frequency range. In an initial approximation, identical subwavelength patch resonators are aligned in a planar configuration as shown in Figure 2.11 (a). The basic parameters in this scheme are the lateral size of the patch microcavities s, the separation between resonators d, their thickness L and the number of elements aligned in the $x-$ and $y-$directions. With reference to equation (2.20), the patch microcavities have their resonance condition determined by the patch size s according to $s = \lambda/2n_{eff}$, where $n_{eff} = \sqrt{\epsilon_{eff}}$. Also in Figure 2.11 (a) (right panel) the simulated intracavity electric fields E_z of the the fundamental degenerate modes TM_{10} and TM_{01} are shown. The array of unwired elements serves only as an illustrative example for presenting this model. No practical device could be realized with it, as there is no way to provide electrical inputs to the array elements. The most straightforward way to provide bias to all elements is by interconnecting the antennas to contact pads along one direction with subwavelength wires of length d and width w as depicted in Figure 2.11 (b).

The addition of the interconnecting wires has an important effect in the microcavities' mode confinement. First, as revealed in Figure 2.11, enhancement of the electric

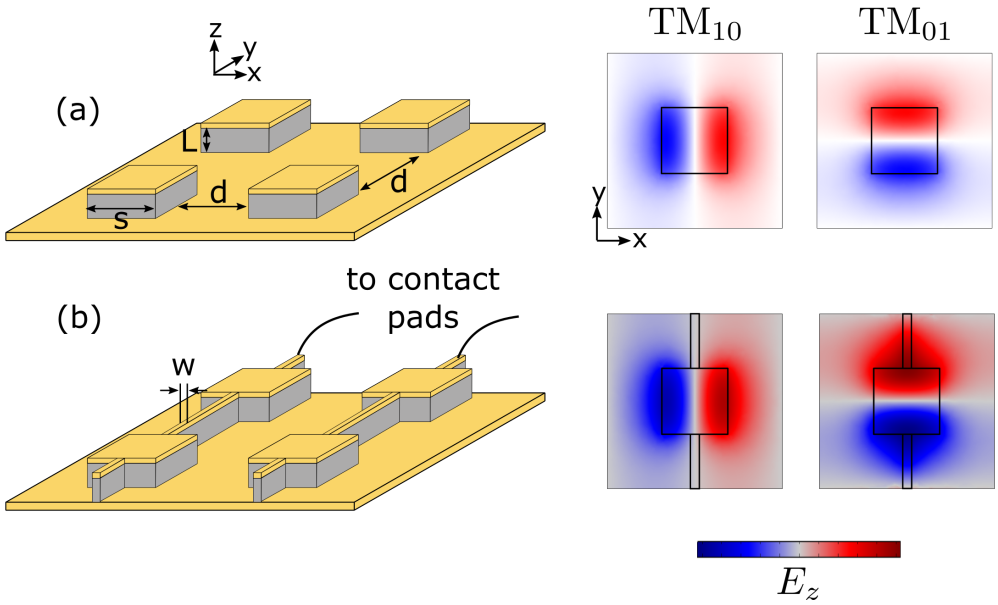

Figure 2.11: Patch Antenna Microcavity array schematic. Schematic and distribution of the intracavity field E_z for the degenerate modes TM_{10} and TM_{01} of (a) an unwired array and (b) a wired array of patch antenna microcavities.

field E_z occurs for arrayed structures. The wires are purely confinement elements and do not radiate due to the canceling effect of the counter-directional magnetic currents at the wires' lateral facets, as noted in section 2.1.3.

The interconnection direction relative to the intracavity mode symmetry also dictates the spectral behavior of the patch cavities. Reflectivity simulations were carried out to evaluate this effect (refer to section 2.4.1 for details about the reflectivity simulations). For arrays subjected to interconnection in the $y-$direction, the TM_{10} resonant frequency and quality factor remain unaffected compared to isolated resonators, as shown in Figure 2.12. In this case, the position of the wires coincides with the field node of the half-wave resonance of E_z. Conversely, the TM_{01} is coupled to the wires resulting in an enhancement of the quality factor. This is attributed to lower radiative losses from the wires, as previously reported for THz nanoantennas [124] and mid-IR detectors [125].

Another advantageous effect introduced by the subwavelength wires is that they provide a new degree of freedom for tuning the resonant frequency of the patch antenna array. Specifically, for an array of square patch antennas with side length $s = 15$ μm interconnected along the $y-$direction and spaced apart $d = 25$ μm, the natural fundamental degenerate modes resonate at $f_r = 3.2$ THz. By varying the length d of the wire, one can design the frequency detuning between the TM_{10} and TM_{01} modes as shown in Figure 2.13. For a given patch size, the TM_{10} remains fixed at the resonant frequency, as there is no spatial overlap between the mode and the wire. On the other hand, the TM_{01} mode is coupled to the wires and the mode extends spatially along the same direction. This effect becomes stronger as the wire is made longer, shifting the mode to lower frequencies and increasing the array quality factor as noted in the 2D simulations (Section 2.3). This effectively introduces a control parameter to detune

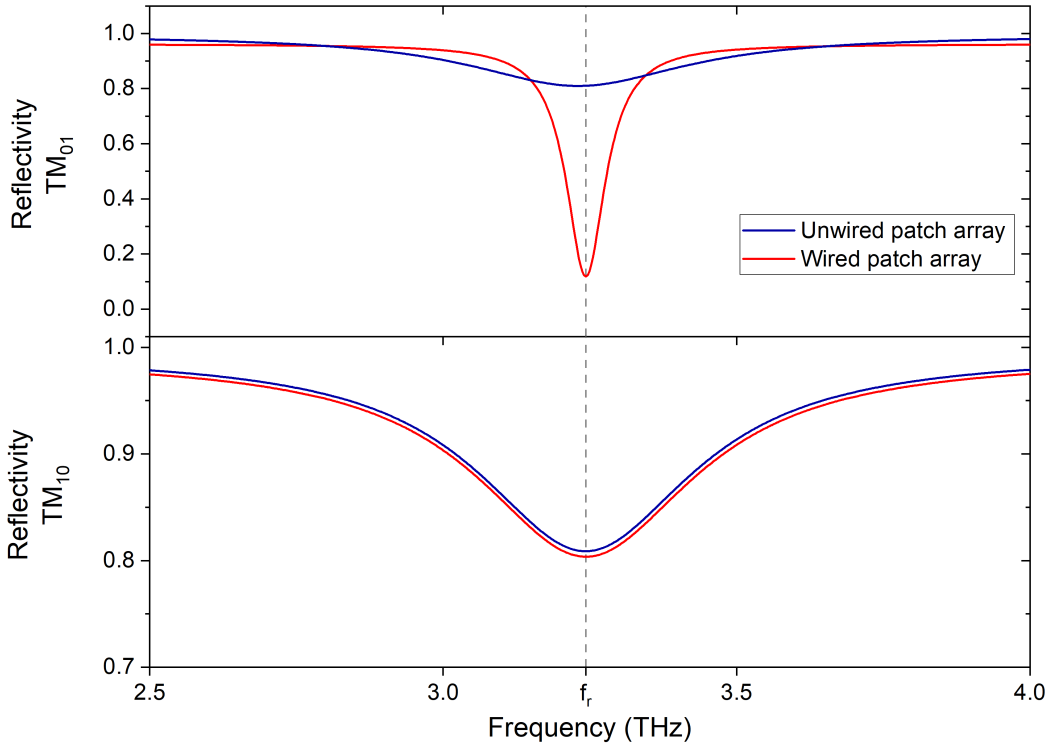

Figure 2.12: Effect of wires in an array of patch antenna microcavities. Simulated reflectivity spectra of two array configurations of patch antenna microcavities: unwired (blue curves) and wired (red curves) for the degenerate TM_{01} and TM_{10} modes. Array parameters: s= 15 μm, d= 25 μm, w= 2 μm, f_r= 3.2 THz. Plots adapted from [126].

one mode with respect to the other. In section 4.1 it will be demonstrated how one can use this detuning control to design the polarization state of the array [126].

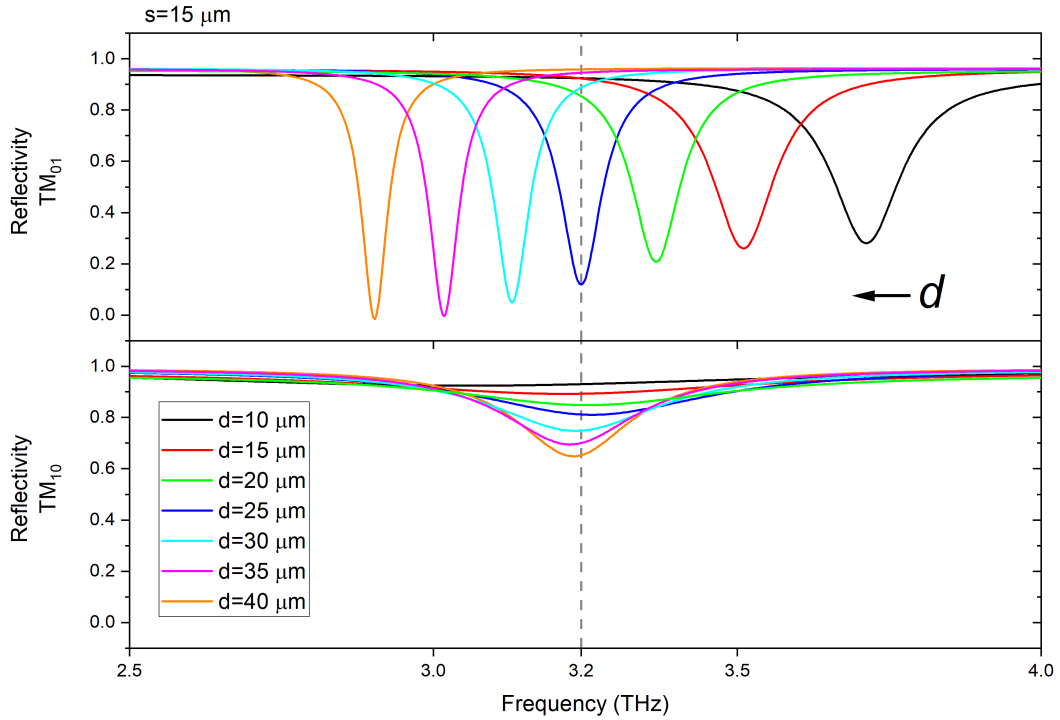

Figure 2.13: Tuning the resonant frequency of wired arrays. Reflectivity spectra for patch arrays of side length $s = 15$ μm interconnected along the $y-$direction with wires of varied lengths.

2.4.1 Losses and extraction efficiencies in wired arrays

The 2D simulations provide good insight and a valid trend of the nature of the losses in patch microcavity arrays. However, the effect of the interconnecting wires cannot be captured within this approximation. To investigate the losses in wired arrays of patch microcavities, we performed 3D reflectivity simulations.

As previously mentioned, the interconnecting wires frequency-decouple the patches transverse fundamental modes. To look into the effect caused in each of the TM cavity modes, we performed reflectivity simulations with (1) the electric field of the incident wave parallel to the interconnecting wires and (2) with the electric field perpendicular to the wires. Each of these configurations excites a TM_{01} and a TM_{10} mode in the cavities respectively. Figure 2.14 shows the simulation model. It consists of an air-box domain that contains a wired patch microcavity, representing the unit cell of an infinite array. The box's top boundary is utilized as an excitation port from where a TE-polarized wave is propagated with an electric field of $E = \{0, E_0 e^{-j(k_x x + k_z z)}, 0\}$ and wave vector $k = \{k_x, 0, k_z\}$ for the case (1); and $E = \{E_0 e^{-j(k_y y + k_z z)}, 0, 0\}$ with $k = \{0, k_y, k_z\}$ for the case (2). We simulated only the case of normal incidence ($\theta = 0$). The wired patch microcavity consists of two stacked block domains: Au and GaAs. Complex refractive indices were taken from [119]. To simulate an infinite array, the air-box was flanked with Floquet periodic boundary conditions with periodic wave vectors k_F equal to the wave vectors of the propagating wave.

Quality factors were extracted by fitting the reflectivity spectra to a Lorentzian

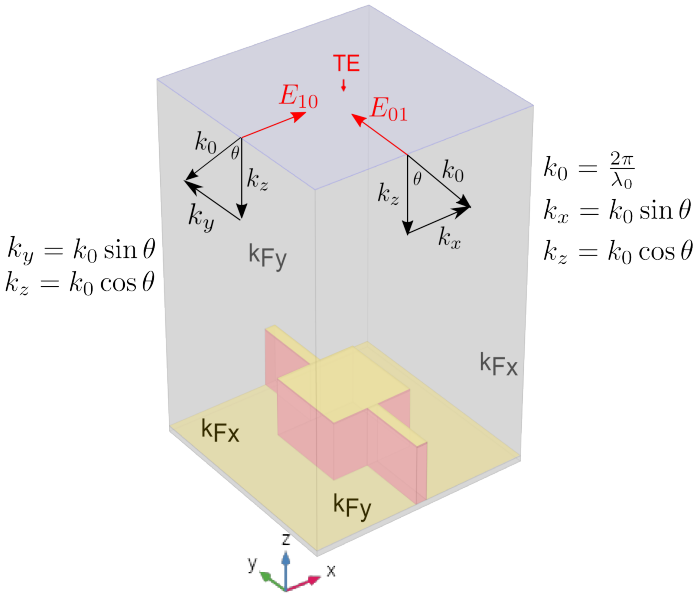

Figure 2.14: 3D Model for reflectivity simulations. An air-box domain contains a wired patch microcavity. Yellow areas depict the gold domains and red the GaAs domain. An excitation port with TE polarization was placed at the top of the air-box to simulate a plane wave propagating in the $z-$direction. The box is flanked with Floquet periodic boundary conditions with wave vectors $k_F = k$.

profile. In Figure 2.15 the TM_{10} and TM_{01} total quality factors Q for several array configurations are plotted as a function of the separation distance between the array elements.

As a general trend, we observe that the quality factors for the transverse mode along the wires (TM_{01}) are always greater than the perpendicular TM_{10} mode. The presence of the wires provides stronger confinement for the TM_{01} mode, and as the wire length increases, the losses further decrease. Since the width of the wires was fixed in all the simulations, the losses of the TM_{10} mode remain invariant for different s.

In order to assess the different contributions to the system losses, the radiative and non-radiative contributions were extracted in a similar way as it was done in section 2.3. Figure 2.16 shows a comparison between the different system losses as a function of d for the TM_{01} and TM_{10} modes for arrays with patch size $s = 16$ μm. By examining the figure, one can see that the radiative losses govern the system for the two transversal modes. Further, a small dependence of the non-radiative losses with d is observed in the TM_{01} mode. On the other hand, the non-radiative losses vary with the geometry of the array in the orthogonal TM_{10} mode. Here, for very dense arrays, the mode couples between neighboring microcavities which enhances the interaction between the mode and the lossy metallic boundaries, causing higher non-radiative losses. Nonetheless, Q_{rad} is always larger than Q_{nr} and almost overlaps with the total quality factor.

Finally, the photon extraction efficiencies were calculated by evaluating equation (2.26). Results are plotted in Figure 2.15. High extraction efficiencies as high as

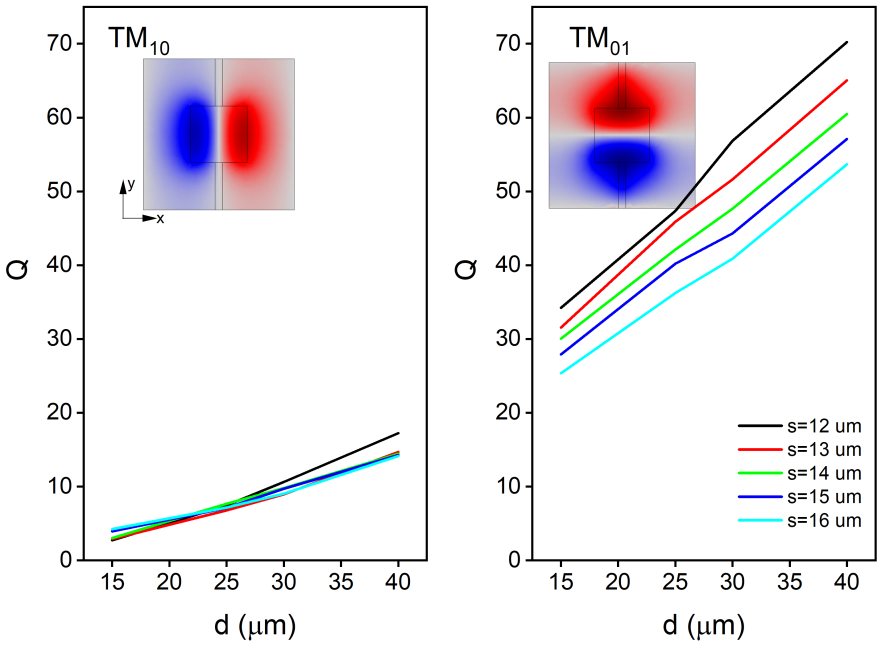

Figure 2.15: Quality factors in wired arrays of patch microcavities. Total quality factors Q as a function of the distance between array elements for the resonant modes TM_{10} and TM_{01} for various patch lateral sizes s.

90% are obtained for both modes, and they exhibit steady values which are almost independent from the parameter d. These results show that, in the case of emitters, the high extraction efficiencies allow the device to radiate in the two orthogonal modes with similar photon outcoupling efficiency. Therefore, the length of the wires can be used as an independent parameter to control the frequency detuning of the orthogonal modes to design the polarization state as will be shown in chapter 4.

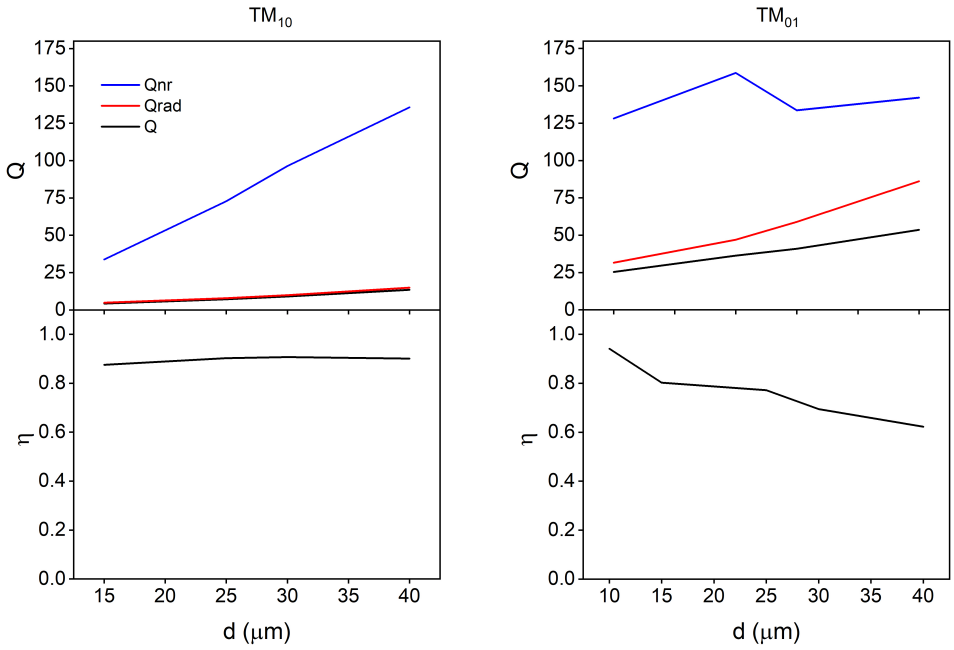

Figure 2.16: Comparison between total, radiative, and non-radiative quality factors vs distance d in wired arrays and extraction efficiencies. Comparison between the TM_{10} and TM_{01} modes for s =16 μm.

2.5 Summary

This chapter presented an in-depth review of patch antennas. Section 2.1 presented the two most used models to describe the electric properties of patch antennas from the point of view of the microwave regime, among which the *cavity model* proved useful to characterize the radiation from patch antennas scaled to operate in the THz regime. Section 2.2 provided useful concepts of antenna array theory, showing that, for the particular case of a planar array of antennas, the divergence of the beam in the far-field follows an asymptotic behavior with a $\sim 1/N^2$ dependence, where N^2 is the total number of antenna elements in the array. Next, section 2.3 examined the losses in arrays of patch antennas. Numerical simulations of linear arrays revealed that the array geometry can be used to tune the different contributions to the total losses in the system, providing engineered quality factors and photon extraction efficiencies. Finally, section 2.4 presented a study of the behavior of wired arrays of square patch antennas via full-wave finite element simulations. Subwavelength wires crossing the structure of the patch in one direction introduce a plasmonic effect which enhances the intracavity field and the quality factor of the patch structure in the direction parallel to the wire. Moreover, the simulations results showed that the geometry of the wire introduces an additional degree of freedom to control the resonance frequency of the patch fundamental modes. The chapter concludes with a study of the losses and photon extraction efficiencies of wired arrays of patch antennas. Results showed that high photon extraction efficiencies can be obtained in the two orthogonal transversal

microcavity modes, allowing emitters based on this architecture to radiate in the two TM regimes. These features enable the design of any arbitrary polarization state via controlled mode detuning.

Chapter 3

Patch Antenna Microcavity THz QCL

In the previous chapters, we introduced the fundamental concepts and operational principles of THz QCLs and the basic notions of patch antenna microcavity structures and their behavior in a wired array configuration. This thesis merges both elements to demonstrate *patch antenna microcavity* (PAM) THz QC lasers. This chapter starts by presenting the QC active region used throughout the project. It then continues by describing in detail the fabrication techniques and the fabrication procedure of the physical devices. Characterization methods and results from selected samples are presented. These results are compared with the emission characteristics of a standard double metal ridge waveguide. Finally, the chapter shows a study of the far-field radiation from the fabricated QCLs by comparing experimental results with numerical full-wave simulations from finite arrays.

3.1 L1157 sample

The Quantum Cascade active region used in this project (sample L1157) was grown by molecular beam epitaxy (MBE) by the group of Prof. Edmund Linfield at the University of Leeds. The active region is based on a hybrid LO-phonon, bound-to-continuum design with a central operating frequency of 3.2 THz. This design combines the advantages of the bound-to-continuum approach of demanding low current for lasing, and the LO-phonon depopulation scheme, providing good temperature performance and high output power. This active region was first proposed by Scalari, et al. [128]. Later, this growth was revisited to achieve optimized lower threshold current densities and operating voltages [127]. The L1157 sample is a re-growth of this later study. The heterostructure consists of alternating layers of GaAs/AlGaAs forming a cascade of alternating photon and LO-phonon assisted transitions between two minibands. The epitaxial growth was performed on a semi-insulating host GaAs substrate, starting with a 300 nm-thick $Al_{0.5}Ga_{0.5}As$ sacrificial etch stop layer (which allows the processing of the device into double-metal configuration) followed by a 700 nm-thick highly doped GaAs contact layer ($n = 2 \times 10^{-8}$ cm^{-3}). The active region comprises 85 periods of nine quantum wells composed of a GaAs/$Al_{0.15}Ga_{0.85}As$ heterostructure, totaling a thickness of 11 μm. A single period comprises **3**/9.5/**3**/11.8/**2**/12.9/**1**/16.2/**0.5**/10.1/**4**/14.5/**3**/<u>17</u>/**3**/7.1/**3**/8.6 (all in nm), where bold

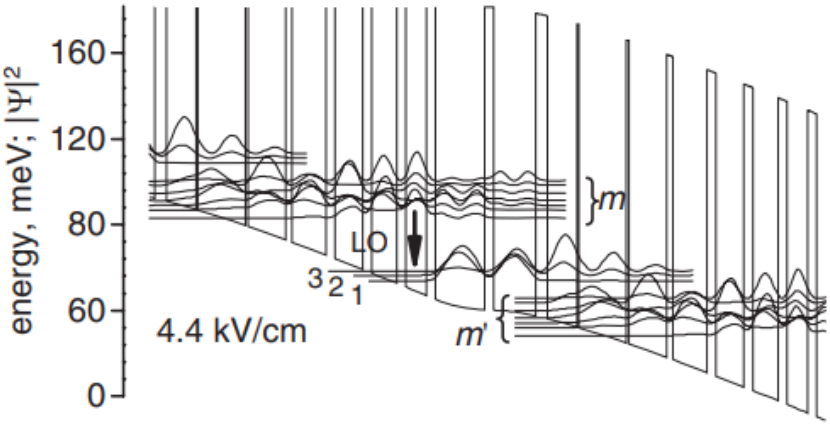

Figure 3.1: Conduction band and squared moduli of the wavefunctions of the L1157 sample. Minibands for two different cascades are denoted as m and m'. Lasing transition occurs from one of the states 3 or 2 to the miniband m'. Taken from Ref [127].

numbers refer to the thickness of the $Al_{0.15}Ga_{0.85}As$ barriers, and the underlined number denotes a Si-doped GaAs layer (3×10^{16} cm^{-3}). Figure 3.1 shows the calculated conduction band profile and the square moduli of the wavefunctions for the active region for an electric field of 4.4 kV/cm. Lasing transitions occur from one of the states 3 or 2 to the miniband m', whereas LO-phonon-assisted transition occurs from the miniband m to one of the states 1 or 2.

To form the double metal structure, the sample was wafer-bonded to a n^+ GaAs receptor wafer via Au-Au thermocompression bonding. After this, the sample was processed into arrays of patch antenna microcavities using standard photolithography techniques and dry etching. A detailed description of the fabrication procedure is shown in the next sections.

3.2 Fabrication

The fabrication of PAM arrays is a multi-step process which requires the combination of diverse techniques for selectively adding/subtracting material as the fabrication is carried out. Methods like photolithography, material deposition, etching and *lift-off* were used to define the PAM structures in the QC samples. With the exception of the QC growth and wafer-bonding, all the fabrication process took place at the cleanroom facility of OIST. This section provides an overview of the fabrication techniques while presenting the instrumentation employed in every step. Following, the protocol designed for the device fabrication is described. Appendix A summarizes the steps of the fabrication procedure.

3.2.1 Fabrication techniques

Photolithography

Photolithography is a technique which consists on transferring a pattern to a photosensitive resin by exposure to a light source. We utilized a maskless lithography system [NANO SYSTEM SOLUTIONS Dlight DL-1000]. This instrument uses a telecentric optics illumination system [129] and a digital micromirror device (DMD) to directly expose onto a photoresist a desired pattern. One of the most convenient characteristics of Dlight DL-1000 is the monitoring system composed of CCD cameras, which permit the direct visualization of the substrate and the exposure optic path. This allows an easy and accurate alignment of the different layers of which the device is composed.

The most generic sequence for photolithography and patterning transfer proceeds as follows:

1. Substrate cleaning. Contaminants such as particles, dust or solvent stains can lead to adverse effects during the process. Chemical treatment (acetone and isopropanol bath), O_2 plasma cleaning and N_2 blow-drying must be performed at the very first stage.

2. Spin coating. A thin film of an organic polymer sensitive to light (photoresist) is uniformly deposited on the surface of the substrate by spinning the sample at a velocity ω. The thickness T of the deposited layer is inversely proportional to ω by the relation $T \propto \frac{C\eta}{\omega}$ [130], where C is the polymer concentration (in g/100-mL) and η is its intrinsic viscosity. A good rule of thumb for the thickness T of the spin-coated photoresist is to be at least 33 % thicker than the thickness of the material to be deposited.

3. Exposure. Typically, UV light (λ =405 nm for NANO SYSTEM SOLUTIONS Dlight DL-1000) is used to expose the photoresist. Depending on whether the photoresist is positive or negative, the exposed part of the resist will soften or harden.

4. Develop. The sample is rinsed in a developing chemical which removes the exposed areas in samples coated with a positive photoresist (in the case of a negative photoresist the unexposed areas) and leaves a bare area which is the positive (or negative) image of the pattern to be transferred.

Material Deposition

In the fabrication process of PAMs, materials were deposited by physical vapor deposition (PVD). PVD refers to vacuum deposition techniques where the material is converted into a vapor phase, to be then transported to the sample where it finally condensates forming a thin film. Normally, samples are held upside down facing the target (material to be deposited) in a direct line. The material is then deposited over the entire surface of the sample simultaneously. This process takes place in a high-vacuum chamber (10^{-6} Torr) to assure a large mean free path for the vapor molecules and to avoid chemical reactions (e.g. formation of oxide impurities) at the source or at

the sample's surface. We utilized two types of PVD coating methods: vacuum sputter deposition for oxides and thermal evaporation for metals.

- **Vacuum Sputter Deposition**. In this technique, the target is bombarded by Ar ions which are accelerated by a high voltage creating a glow discharge or plasma. The target material (cathode) is sputtered away as neutral atoms by momentum transfer, and the ejected atoms reach the sample's substrate placed on the anode where they condensate creating a thin film. The amount of material W sputtered from the target is inversely proportional to the distance between the anode and cathode d and the pressure from the gas P by the relation $W \propto \frac{VI}{Pd}$, where V is the bias voltage and I the discharge current [130]. We used the instrument ULVAC CAM-S for depositing thin films of SiO_2. The system is equipped with a rotating stage, which allows for a uniform deposition.

- **Thermal Evaporation**. For the metalization, electron beam (e-beam) evaporation was used [PLASSYS BESTEK MEB550S2-HV]. In this technique, metals are evaporated by bombarding the target with a high-intensity e-beam gun under high vacuum. This causes the atoms of the metal to travel inside the vacuum chamber without colliding, coating everything inside the chamber within the line of sight of the expelled metal atoms. The instrument features a substrate treatment consisting of low-energy Ar ions bombardment, which removes the native oxide layer on the surface of the substrate, then promoting adhesion of metals to the sample.

Lift-off

Lift-off refers to the process of dissolving the photoresist underneath the deposited material, then lifting it up and leaving the desired pattern on the sample. For this step, it is important to consider the wall profile of the photoresist after development. In general, two wall profiles can be obtained as it is shown in Figure 3.2. An undercut profile is characterized by having inward wall-angles >90°. For negative resists, this angle is the most typical profile. Contrarily, overcut profiles are characterized by outward sloping resist profiles with angles <90°. For the process of lift-off, it is important that a discontinuity in the deposited material exists, so that the solvent can get to the uncoated walls. This is achieved by having an undercut profile of the photoresist combined with using a line-of-sight deposition method. By doing this, the inward sloping photoresist walls will receive little or no material deposit, as depicted in Figure 3.2 b), creating the necessary gap for the solvent to dissolve the photoresist and lift off the material on top of it (Figure 3.2) c).

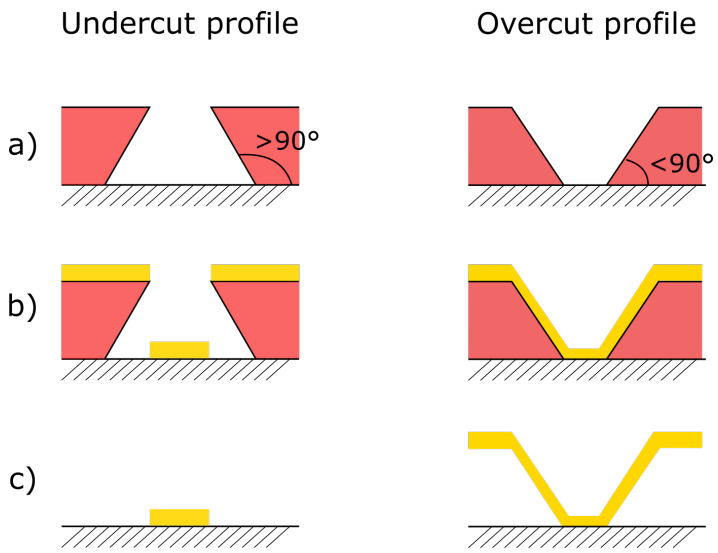

Figure 3.2: Lift-off for different resist profiles. On the left side, the lift-off process for a resist with an undercut wall profile; and on the right side, lift-off process for a resist with an overcut wall profile. a) Resist development. b) Material deposition. c) Lift-off.

Etching

Generally, there exit two different methods for etching materials: dry etching and wet etching. The first of them refers to etching with a plasma of reactive gases which bombards a patterned sample. It allows an anisotropic (directional) etching which is appropriate for achieving vertical sidewalls leading to a good image transfer. Inductively coupled plasma [Oxford Instruments Plasmalab 100] was used for engraving the PAM structures in the QC sample. The instrument is equipped with active temperature control at the sample's position consisting of a helium backside cooling system and a thermal coolant circulator. This permits to maintain a specific temperature at the sample during the etching process. On the other hand, wet etching refers to etching with liquid etchants. It allows removing material with high selectivity. Different acids were used to initially remove the substrate base of the QC sample.

3.2.2 Fabrication Protocol

We fabricated planar arrays (10×10 elements) of wired patch antenna microcavities in the QC sample. Figure 3.3 presents the design layout. The array is bounded at its top and bottom by rectangular contact pads for current bias. The contact pads are insulated from the QC active region by a 200-nm-thick SiO_2 layer to avoid current contribution from these structures. Arrays of different patch sizes s and distances d were fabricated to evaluate the geometrical influence on the radiation properties of the laser. In the next sections, we will describe in detail the fabrication process. A summarized schematic of the fabrication procedure is depicted in the Figure A.1 of appendix A.

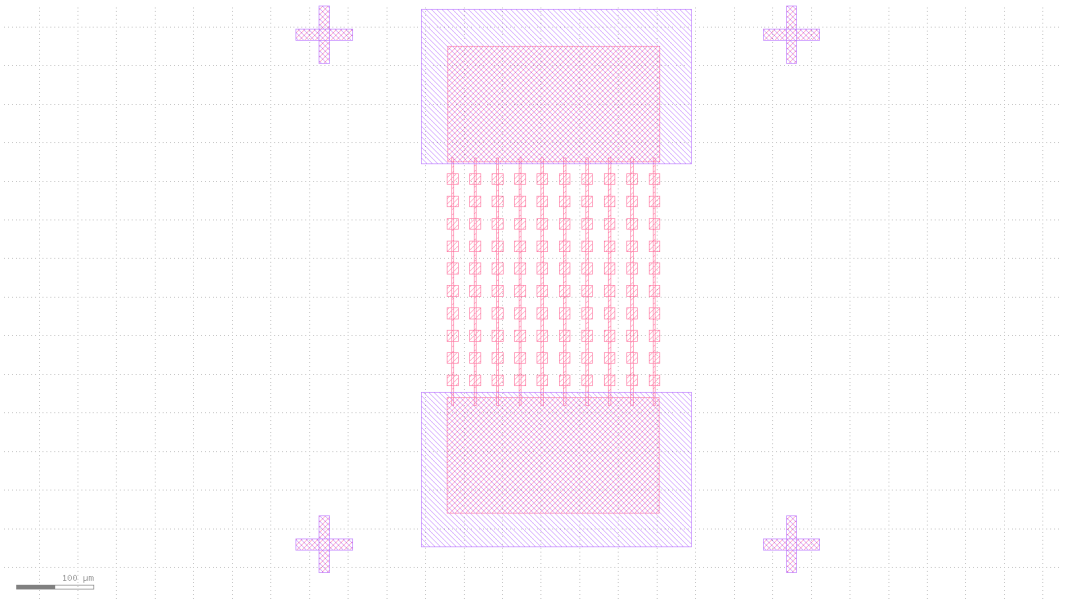

Figure 3.3: PAM array layout. The layout consists on a planar array of 10 × 10 square patches of lateral size s separated away a distance d and interconnected by subwavelength wires with width w. Blue rectangles (1st layer) represent the the insulating SiO_2 pads, whereas red areas represent the metal Au parts (2nd layer). Crosses at the corners (on both 1st and 2nd layers) serve as reference marks for layer alignment.

1. Substrate removal

To define the double metal structure, the MBE growth and a n^+ GaAs receptor wafer were coated with a thin film of gold to bond them together by Au-Au thermo-compressive wafer bonding [131, 132].

After this, all the fabrication process took place at OIST's cleanroom facility. The first step consisted on removing the 300 μm-thick host GaAs wafer on which the QC was grown. For this, mechanical lapping and selective etching were used. First, the sample was mounted on a glass slide using clear wax. Via mechanical lapping and using sheets of decreasing grit size, the sample was thinned until approximately ∼100 μm remained, as controlled by a micrometer. The remaining material was etched with a citric acid (100 gr): H_2O_2 (40 ml): H_2O (100 ml) solution at an etch rate of ∼300 nm/min. When the etch-stop layer is reached, the surface becomes mirror-like, and when exposed to air oxidation of this layer occurs quickly and reflection fringes appear in the surface [133]. Next, the sample was immersed for 2 minutes into 25 % HF acid to remove the $Al_{0.5}Ga_{0.5}As$ etch stop layer. Because of the high selectivity for $Al_{0.5}Ga_{0.5}As$ over GaAs [134], there is negligible damage to the highly doped GaAs contact layer which is beneath the sacrificial etch stop layer. After this process is completed, the sample was cleaved into rectangles of ∼5x7 mm.

2. Photolithography for the 1st layer and SiO_2 deposition

The first step for the lithography process is the elaboration of the mask defining the array structures. The software KLayout was used to create the necessary GDSII files of the layout shown in Figure 3.3. The first layer consists of rectangular shapes (blue parts in Figure 3.3) and cross-shaped reference marks for alignment of the next layer. An undercut profile is desired after development of the photoresist for lift-off. Undercut profiles are difficult to achieve in positive resists, because the optical exposure dose is higher in the surface than in the resist/substrate interface, resulting in an overcut profile after development [130]. So, a negative photoresist (ARN 4450) was used for the photolithography of all the layers. Figure 3.4 shows schematically this fabrication step (for detailed parameters refer to appendix A).

a) After thoroughly cleaning the QC sample, the photoresist ARN 4450 was spin-coated on the surface of the QC samples. Following, a soft bake was conducted using a hotplate to harden the resist.

b) The sample is exposed using a maskless lithography system ($\lambda = 405$ nm).

c) Immediately after exposure, a hard bake is done to promote the cross-linking of the resist (a process for rendering the exposed parts insoluble). Development of the unexposed areas followed by immersing the sample into a TMAH solution. Undercut profiles are achieved.

d) Next, vacuum sputter deposition is used to deposit a 200 nm film of SiO_2.

e) After the sputtering process is finished, the sample is immersed into the solvent *Remover PG* for lift-off. Two beakers filled with this solvent heated at 60° are used. The first of them is used to begin the stripping of the resist. To avoid re-depositing of the lifted particles on the substrate, the sample is immersed into the second beaker. After lift-off finishes, the pattern is imprinted on the QC sample's surface.

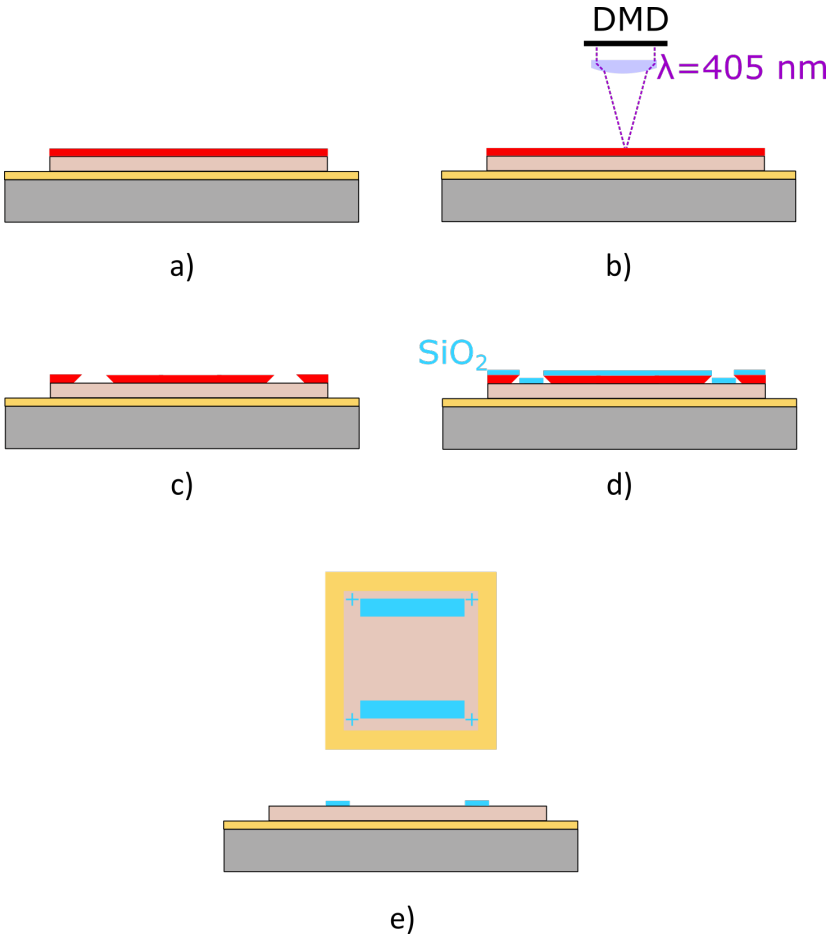

Figure 3.4: Photolithography for the 1st layer and SiO_2 deposition. a) A negative photoresist (ARN 4450) is spin-coated on the surface of the QC sample. b) Exposure of the resist using a maskless lithography system [NANO SYSTEM SOLUTIONS Dlight DL-1000]. c) Development of the photoresist, undercut profiles are achieved. d) A thin film of SiO_2 is sputtered on the sample's surface. e) Lift-off. Insulating pads and reference marks are created on top of the QC sample.

3. Photolithography for the 2nd layer and Au metalization

The photolithography of the second layer was performed in the same way as the first layer. With the help of the reference marks and the positioning system of the maskless DL-1000 instrument, the layout for the second layer was aligned with the 1st layer's patterns. After development, a thin film of titanium (10 nm), followed by a gold layer (400 nm) is coated using e-beam evaporation [PLASSYS BESTEK MEB550S2-HV]. Finally, the sample is soaked in *Remover PG* for liftoff. Quick rounds of ultrasonic action were executed to improve the resist removal efficiency. Figure 3.5 summarizes these steps and presents a microscope image of the fabricated samples at this point.

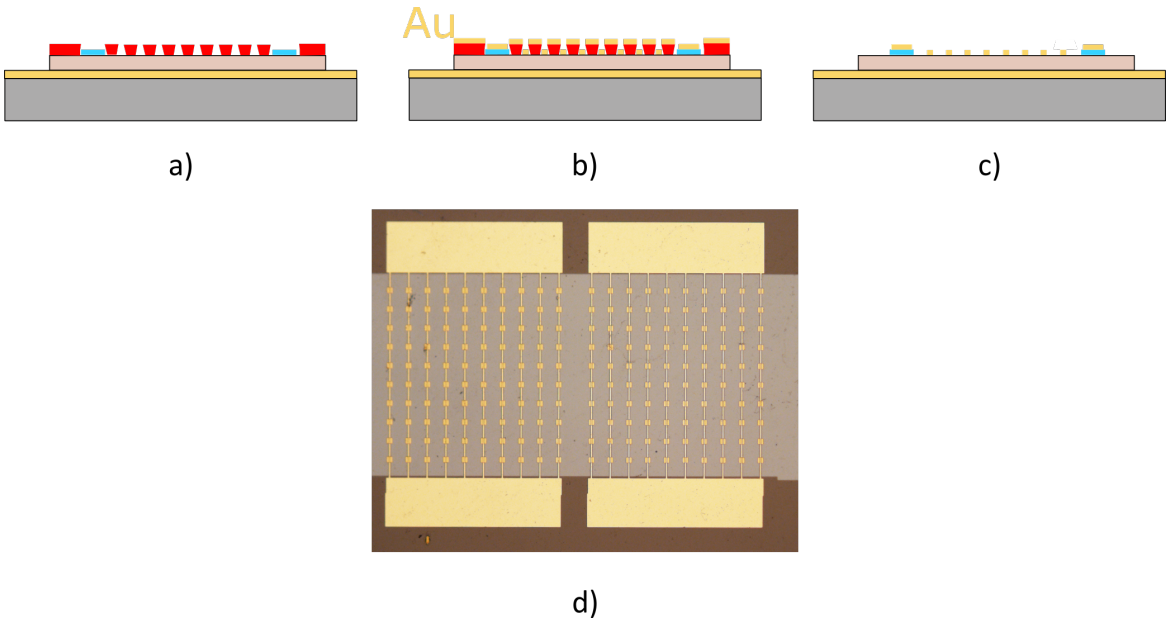

Figure 3.5: Photolithography for the 2nd layer and metalization. a) Photolithography and development of the second layer. b) Deposition of Ti/Au: 100 nm/ 400 nm. c) Lift-off. d) Optical microscope image of two arrays after metalization.

4. Final etch

The metalized structure on the QC sample performed in the previous step functions as a self-aligned mask for the etching process. We utilized the ICP system Oxford Instruments Plasmalab 100. The sample is mounted on a silicon carrier wafer using a thermally conductive mounting paste to improve thermal contact between the QC sample and the carrier wafer. In the etching process, line-of-sight-impacting ions bombard the surface of the sample, milling the zones which are unprotected by the gold layer. For etching GaAs/AlGaAs, a combination of chlorine gases (Cl_2 and BCl_3) was used [135]. The etching time was empirically determined by running trial processes of 30 seconds and monitoring afterwards the etched depth with a profilometer. This process was repeated until the gold layer underneath the QC active region was reached. With a gas flow of 10 sccm for BCl_3 and 20 sccm for Cl_2, an etch rate of 1μm /min was achieved. Figure 3.6 shows the finalized sample.

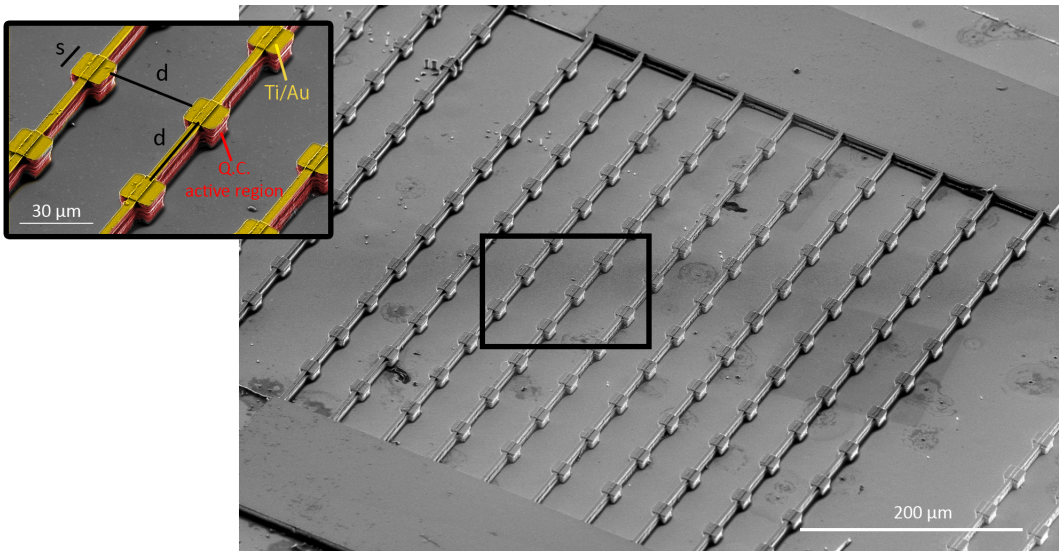

Figure 3.6: SEM image of a fabricated device.

5. Mounting

Samples were mounted onto copper heatsink blocks with dimensions 20×7×2 mm. At the ends of the block, two square gold-coated ceramic pads were glued to act as electrical contacts. The fabricated QCLs were mounted on the copper mount in between the contact pads using indium sheets. To do this, the copper mounts were placed on a hotplate at the melting point of indium (150° C). The indium sheet was placed in between the contact pads and as it melted, the QC sample was placed on top and pushed downwards with two metal needles. After this, the temperature of the hotplate was reduced to let the indium solidify, soldering in this way the QC sample to the mounting surface. Finally, the sample was wire-bonded to the ceramic contact pads using gold wires. A picture of a mounted sample is shown in Figure 3.7.

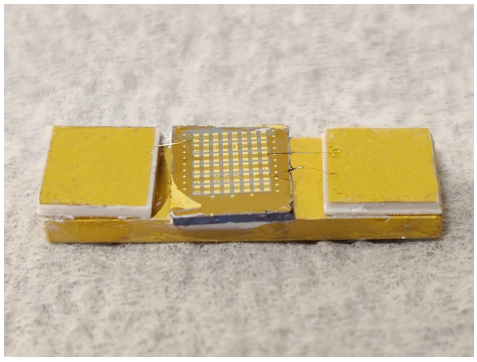

Figure 3.7: Mounted sample.

3.3 Characterization

Device characterization consisted of measuring their electrical, optical and spectral responses. For this, the fabricated devices were mounted on the cold finger of a continuous flow liquid helium cryostat [Oxford Instruments Optistat HE CF-V] using a high-thermal-conductivity silicone paste. The cryostat was equipped with a polyethylene window of 23 mm diameter aperture, through which the radiation from the devices was outcoupled. The measured transmittance from this window is 83% in the 3-4 THz range. The electrical connections to the devices are provided via a 10-pin electrical feed wire to coaxial connectors. The cryostat was aligned relative to the specific experimental setup by fixing the cryostat to a specifically designed mount attached to an XYZ translation stage. The cryostat chamber was pumped down to a pressure of 10^{-4} Torr and then cooled using liquid Helium or Liquid Nitrogen. All the measurements were performed on pulsed mode operation. Next sections will present the electrical, optical and spectral characterization methods used to evaluate the performance of the fabricated devices.

3.3.1 Electrical and Optical characterization

The electrical and optical characteristics of the fabricated QCLs were evaluated by measuring the the voltage across the device's terminals and the output THz power as a function of the applied current (L-I-V characteristics). Figure 3.8 shows a schematic of the experimental setup for the electrical and optical characterization.

L-I-V data was taken while driving the QCL with electrical pulses. To this end, we utilized a pulse generator [Avtechs AVR-2B-B] to provide a 50 kHz pulse train with a 10% duty cycle. The pulse generator was electrically gated at 15 Hz to allow the signal to be detected with a Golay cell. The output from the Golay cell gives a signal proportional to the THz output power. This signal was read by a lock-in amplifier that was also referenced to the 15 Hz electrical signal and was connected to a computer through a GPIB interface. Power levels were calibrated using a Thomas Keating absolute power meter and by taking into account the transmittance from the cryostat window. For the measurements, no additional focusing optics were placed in between the QCL and power meter. To measure the current through the QCL a wideband current probe [Integrated sensors Model 71] was used. The probe was connected to channel 1 of an oscilloscope [Tektronix TDS 3034C] using the 50 Ω termination. The voltage across the device was measured by adding a BNC cable at the electrical terminals of the cryostat and by connecting it to Channel 2 of the oscilloscope. Channels 1 and 2 were triggered by the synchronous output signal of the pulse generator. A LabView program was used to control the instruments and to read the values from the oscilloscope and lock-in amplifier.

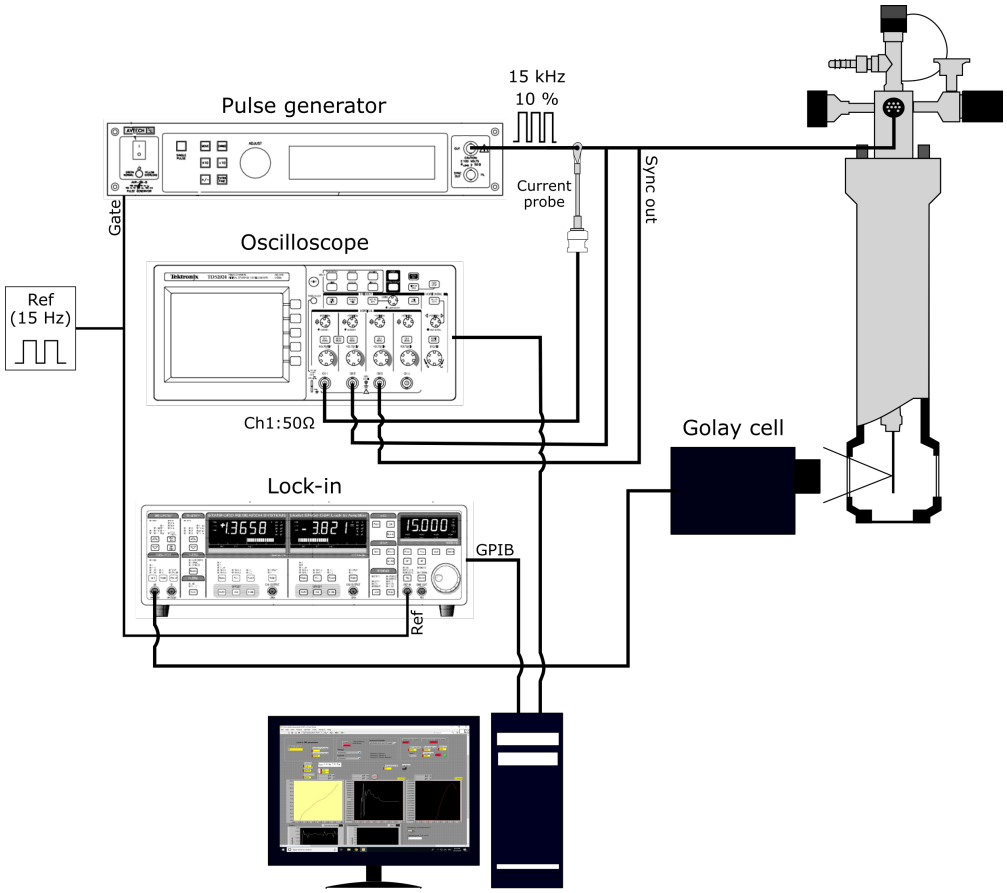

Figure 3.8: Experimental setup for electrical and optical characterization.

L-I-V characteristic curves for an array containing PAMs of lateral size s=15 μm, distanced apart d=40 μm for three different heat sink temperatures (10 K, 77 K and 100 K) are plotted in Figure 3.9. The maximum peak optical power reaches 25 mW with a threshold current density J_{th}=270 A/cm^2, slope efficiency of $\sim$ 111 mW A^{-1} and a wall-plug efficiency of 1.2%. The variation of the threshold current density with temperature is presented in the inset.

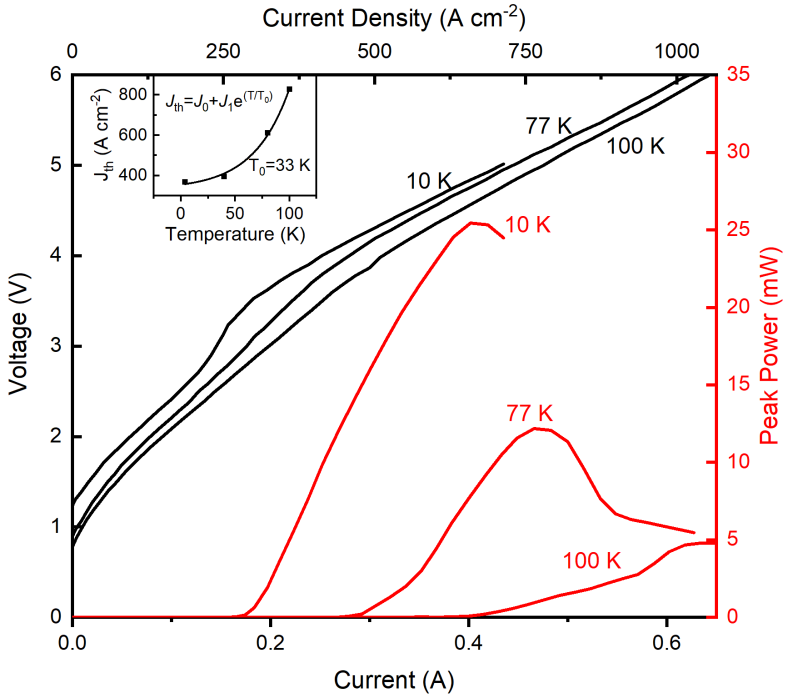

Figure 3.9: LIV data for a PAM array. Array parameters: s=15 μm, d=40 μm. Data taken for three different operating temperatures: 10 K, 77 K and 100 K. Black curves represent the voltage-current data, while red curves the power-current data. Inset: threshold current density as a function of the heat sink temperature (fit based on the empirical formula $J_{th} = J_0 + J_1 e^{T/T_0}$). Adapted from [126].

3.3.2 Spectral characterization

To characterize the spectral response of the fabricated devices, we utilized a Fourier Transform Infrared (FTIR) Spectrometer Vertex 80v Bruker. FTIR spectroscopy is a common technique to measure the frequency components of a light source. Figure 3.10 illustrates the experimental setup.

The QCL biasing is done in the same way as previously described. The radiation from the QCL was collected with a set of parabolic mirrors and focused into the backward input of the FTIR. The FTIR contains a Michelson interferometer which, in the first place, collimates the radiation of the QCL with the backward input mirror. The collimated light impinges upon a beamsplitter (Mylar multilayer) which transmits 50% of the light to a moving mirror and reflects the remaining 50% of the light to a fixed mirror. The light reflected off these mirrors is transmitted/reflected by the beamsplitter one more time and the beams recombine after the beamsplitter, and are ultimately focused onto a detector (RT-DTGS FIR). By varying the path of the moving mirror, the intensity of the composite beam at the detector is an interference pattern known as interferogram. The spectrum of the QCL output signal can then be retrieved by obtaining the Fourier transform of the interferogram signal.

FTIR measurements performed on the patch microcavity array with parameters

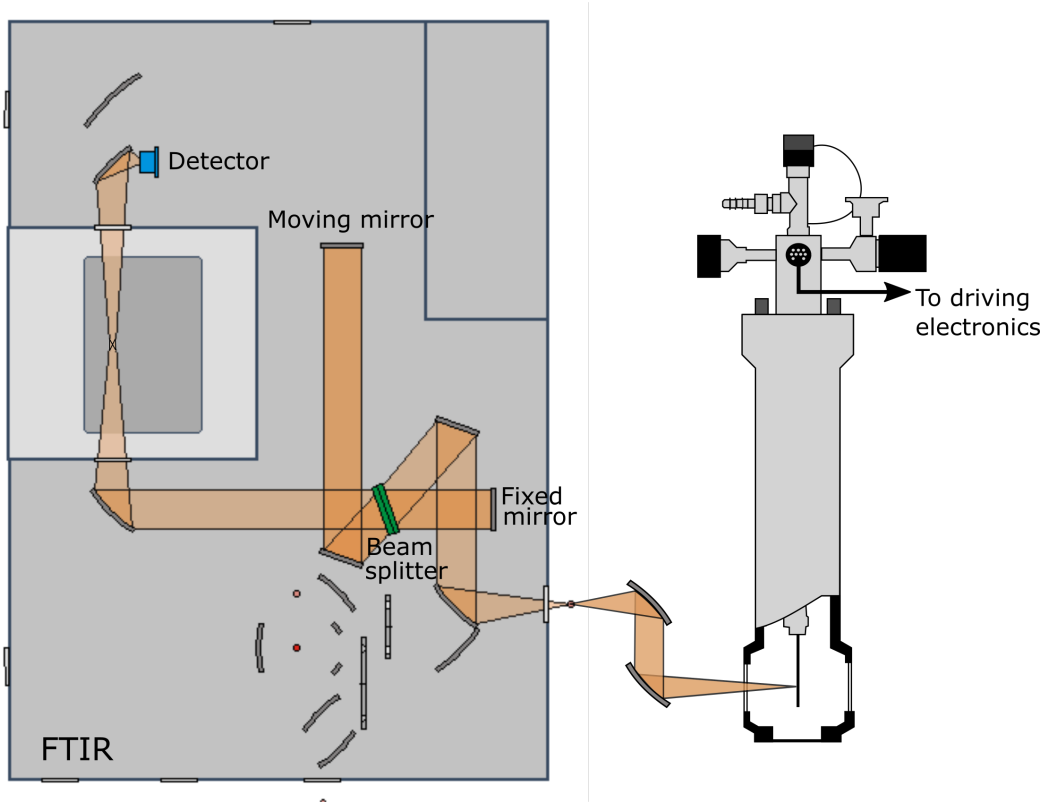

Figure 3.10: Experimental setup for spectral characterization.

s=15 μm, d=40 μm, taken in *Rapid Scan* mode are plotted in Figure 3.11. The measurements were performed at a heat sink temperature of 77 K and for three different bias conditions. The device sustains a robust single mode operation along all the lasing regime.

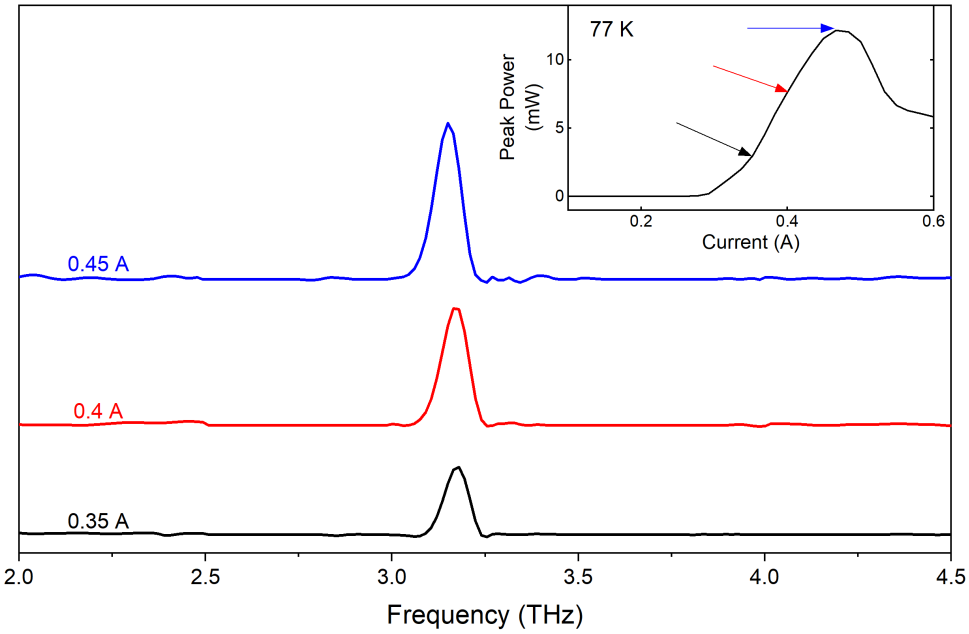

Figure 3.11: Spectra of a PAM THz QCL. Array parameters: s=15 μm, d=40 μm. Data taken at a heat sink temperature of 77 K for three different bias currents. Inset: Sample's L-I curve. Arrows indicate the intensities at which FTIR measurements were taken.

3.4 Comparison of PAM array with standard DM ridge waveguide

For comparative purposes, we processed a sample into a standard double metal ridge waveguide (100 μm-wide, 1.5 mm long). Figure 3.12 shows the L-I-V characteristics of the ridge waveguide and the PAM array (only L-I) presented before.

Data were acquired in pulsed mode operation (50 kHz, 10% duty cycle) at a heat-sink temperature of 10 K. The maximum peak power achieved by the ridge waveguide reaches 19 mW with a threshold current density J_{th}=238 A/cm^2. To compare the performance between the PAM array and the ridge waveguide laser, we calculated the power delivered per unit of electrically pumped area (P_A) for both devices. For the ridge, we calculated P_A= 0.08 W·mm^{-2}, whereas a P_A= 0.4 W·mm^{-2} was obtained for the PAM array. These values correspond to a 5-fold better performance of the patch antenna microcavity device compared to the conventional ridge waveguide laser. The significant enhancement of the emission properties is a signature of an improved extraction efficiency from PAMs provided by the engineering of the losses through the array geometry.

The inset of Figure 3.12 contains the multimode spectrum from the ridge waveguide device. The Fabry-Pérot laser emits on high-order lateral modes over a bandwidth of 400 GHz.

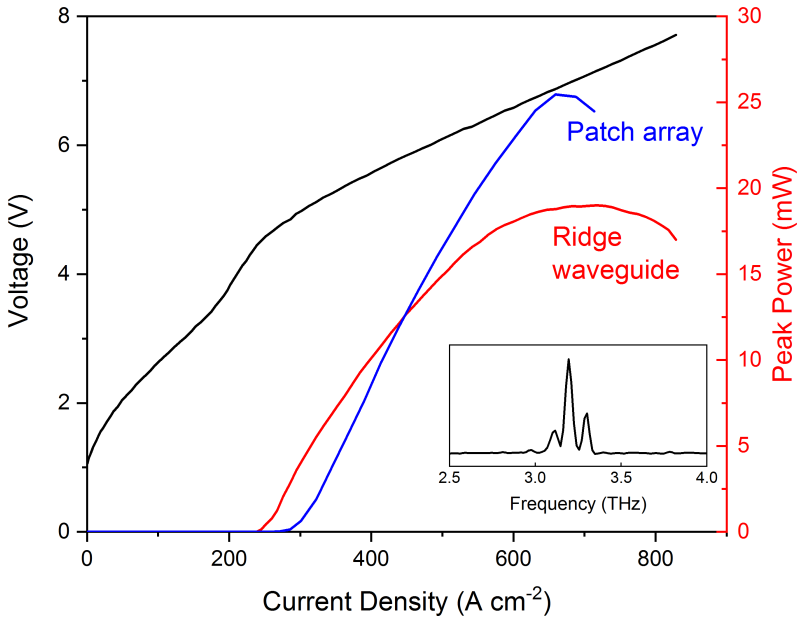

Figure 3.12: Comparison between ridge waveguide QCL and PAM array QCL. Pulsed L-I-V characteristics of a double metal ridge waveguide (100 μm-wide, 1.5 mm long) and L-I characteristics (light blue) of a patch microcavity array (s=15 μm, d= 40 μm). Inset shows the FTIR spectrum of the ridge waveguide QCL.

3.5 Far-field

Terahertz quantum cascade lasers in the double metal waveguide configuration have shown to be the best performing THz QCLs in terms of temperature operation, power and frequency coverage [55, 57]. However, the subwavelength cross-section of the waveguide sandwiching the active medium results in a highly divergent non-directional far-field beam pattern. Numerous efforts have been attempted to circumvent this issue, including the integration of planar horn-type shape structures [81], two-dimensional photonic crystals [83], the use of higher-order DFB gratings [82, 136, 137], wire lasers [138], antenna-feedback [139] and antenna-coupled [86, 140] schemes. Patch antenna microcavities have been also explored, demonstrating the potential of the structure's abilities of acting as reliable antennas to shape the beam. However, their practical demonstration so far has been limited to their implementation in QCLs with external cavities [16–19] and when used as passive out-couplers in association with ridge waveguide lasers [13].

Electrical, optical and spectral characteristics presented in Section 3.3 proved PAM arrays embedding THz QCLs efficient for achieving lasing by means of losses engineering through the array geometry. In this section, we demonstrate that PAM arrays can also be used to obtain shaping of the beam. As stated in section 2.2, there are five control parameters that can be used to manipulate the far-field pattern of an antenna array: (1) the geometrical configuration of the array, (2) the total number of

antennas composing the array, (3) the distance between elements, (4) the excitation amplitude of individual elements, and (5) their relative phases. In an array of antenna-coupled QCLs, it is not possible to directly impose a controlled phase on individual elements just by electrical inputs, since laser action is initiated by spontaneous emission. Also, in large antenna arrays, individual amplitude excitation would require a complex feeding system. Then, these two parameters were not evaluated in this thesis. For measurements purposes, we only varied the distance between individual elements in planar arrays of a fixed number of elements. In the following sections, we first provide the measured far-field beam profiles for selected samples. Then, simulations based on the finite element method for finite arrays of patch antenna microcavities taking into account variations for (1), (2) and (3) are presented.

3.5.1 Far-field measurements

Measurements were performed in pulsed mode operation (50 kHz, 10% duty cycle) at 77 K, using a Golay cell with a small aperture on its entrance window. The Golay cell was mounted on a 2-axis spherical setup (θ, ϕ) placed a distance of 10 cm away from the cryostat. Figure 3.13 presents a typical far-field measurement scanned over a range of $\pm 30°$ with a $1°$ angular resolution in the elevation and azimuthal directions. A single collimated narrow beam is observed with minimal parasitic radiation, confirming the ability of the PAM array to shape the beam.

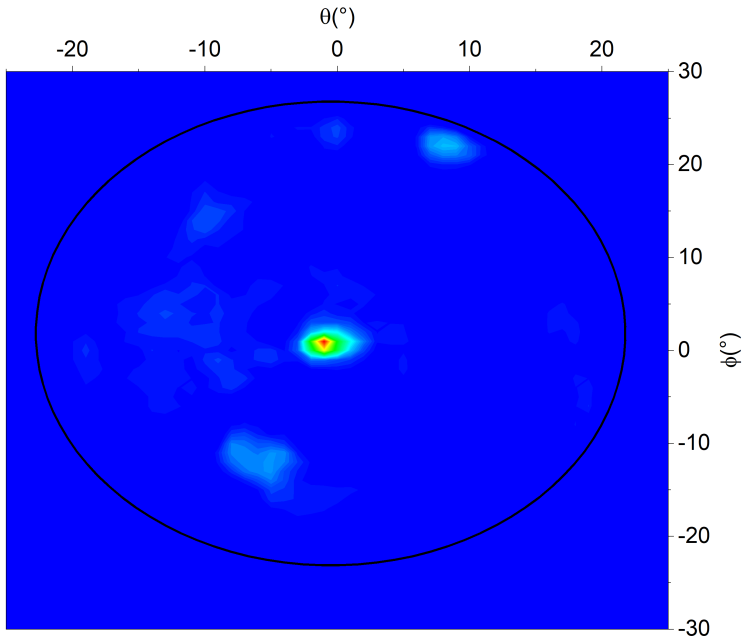

Figure 3.13: Typical far-field profile of a PAM array THz QCL. Scan range: $\pm 30°$ in θ and ϕ with $1°$ angular resolution. An aperture of $\sim$3 mm was placed at the entrance window of the Golay cell. Circle shape indicates the position of the cryostat window.

To evaluate the dependence of the far-field profile with the array configuration, we measured the far-field for three different samples: s=15 μm d= 15 μm, s=15 μm d= 25 μm and s=15 μm d= 40 μm. Samples were scanned over a range of $\pm 6°$ in both elevation and azimuthal directions with 0.3° angular resolution by using an aperture of $>$ 1 mm diameter. Far-field intensity maps were taken for various biasing conditions, to evaluate the quality of the beam along the lasing regime.

The measured far-field intensity maps of sample s=15 μm d= 15 μm are plotted in Figure 3.14.

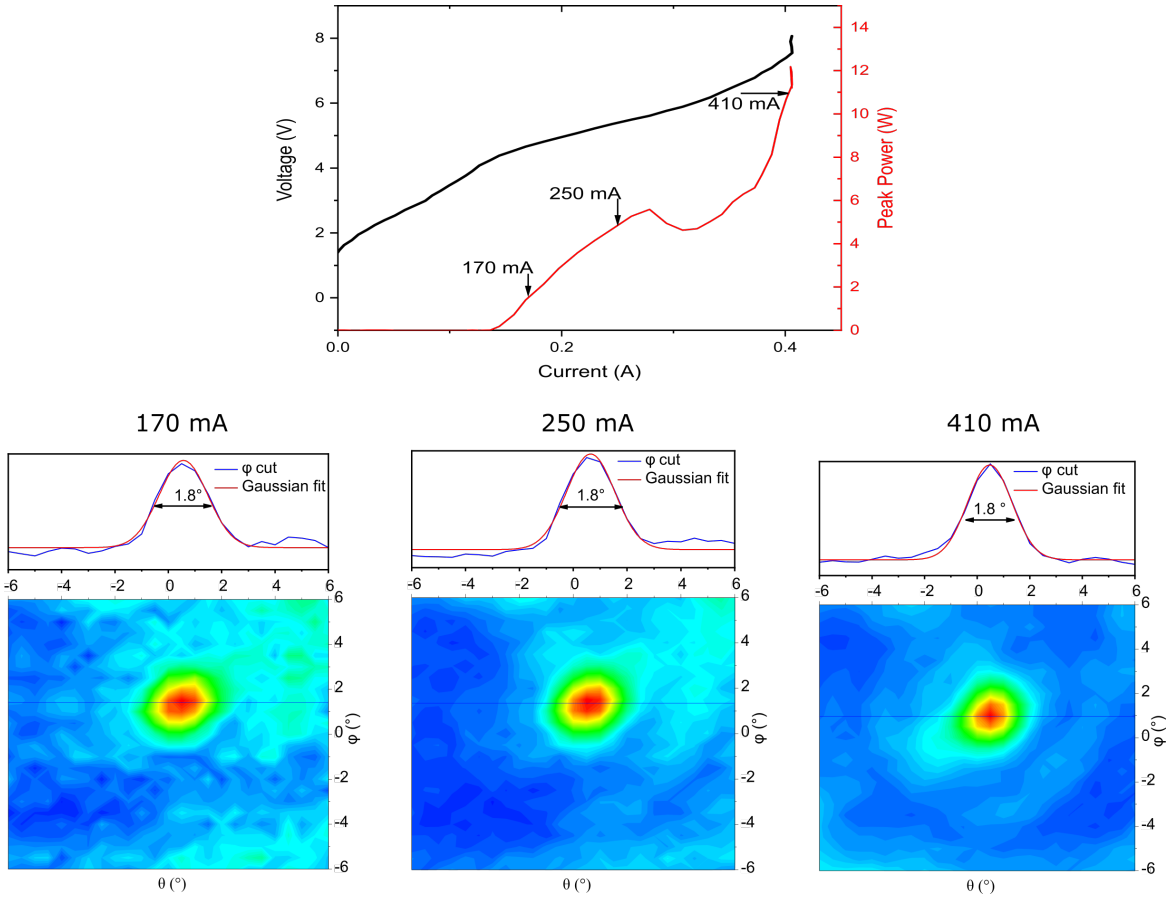

Figure 3.14: LIV curves and far-field intensity maps for sample s=15 μm, d= 15 μm. Data taken for three different bias currents. Profile taken in the ϕ direction. FWHM values calculated by fitting the ϕ cut with a Gaussian fit.

Shaping of the beam is observed for any current excitation. Full width half maximum (FWHM) divergence values were found by extracting 1D cuts along the ϕ direction from the far-field intensity maps and by fitting with a Gaussian curve. Narrow circular beams with divergence as low as FWHM= 1.8° are measured. We also observed clean beams with minimal background noise for measurements taken at higher power (higher excitation currents). In the case of excitation near the lasing threshold, parasitic noise contributes significantly to the far-field intensity profile. An intuitive explanation for this is that the low pumping does not provide enough overall gain to phase-lock all the elements in the array. Slight variations of the physical dimensions among the ar-

ray elements induce an asymmetric onset of the lasing regime from different elements, and at low pump current only a limited fraction of the patch elements may lase. The far-field is then a superposition of large beamwidth radiation from decoupled lasing elements with a coupled fraction. As all resonators lase (higher pumping currents), the entire array becomes phase-locked and the desired narrow beamwidth is achieved. Nonetheless, even at a low pumping regime, partial shaping of the beam occurs, and the shape and FWHM values remain constant at any given excitation.

Similar results are observed for samples s=15 μm d= 25 μm (Figure 3.15) and s=15 μm d= 40 μm (Figure 3.16). For all cases, the far-field has the shape of a narrow Gaussian circular beam and its shape is preserved along all the lasing regime. These results represent the narrowest divergence ever measured in THz QCLs in a double metal monolithic configuration.

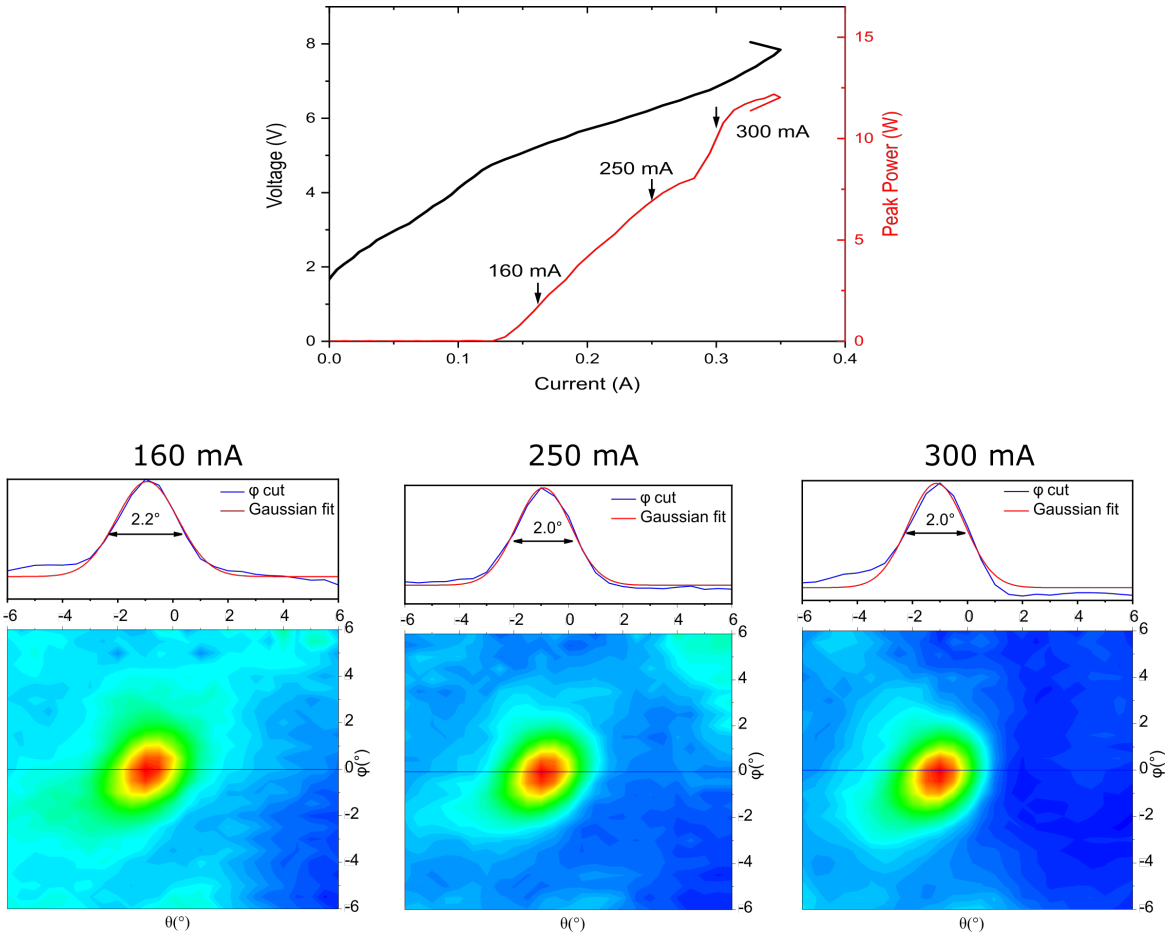

Figure 3.15: LIV curves and far-field intensity maps for sample s=15 μm, d= 25 μm. Data taken for three different bias currents. Profile taken in the ϕ direction. FWHM values calculated by fitting the ϕ cut with a Gaussian fit.

Another result of particular importance is that the inter-element spacing d does not have a significant impact on the beam shaping. For all tested configurations, a Gaussian circular beam shape with FWHM $\sim 2°$ is consistently measured. This allows the parameters d and s to be adjusted independently to achieve other functionalities,

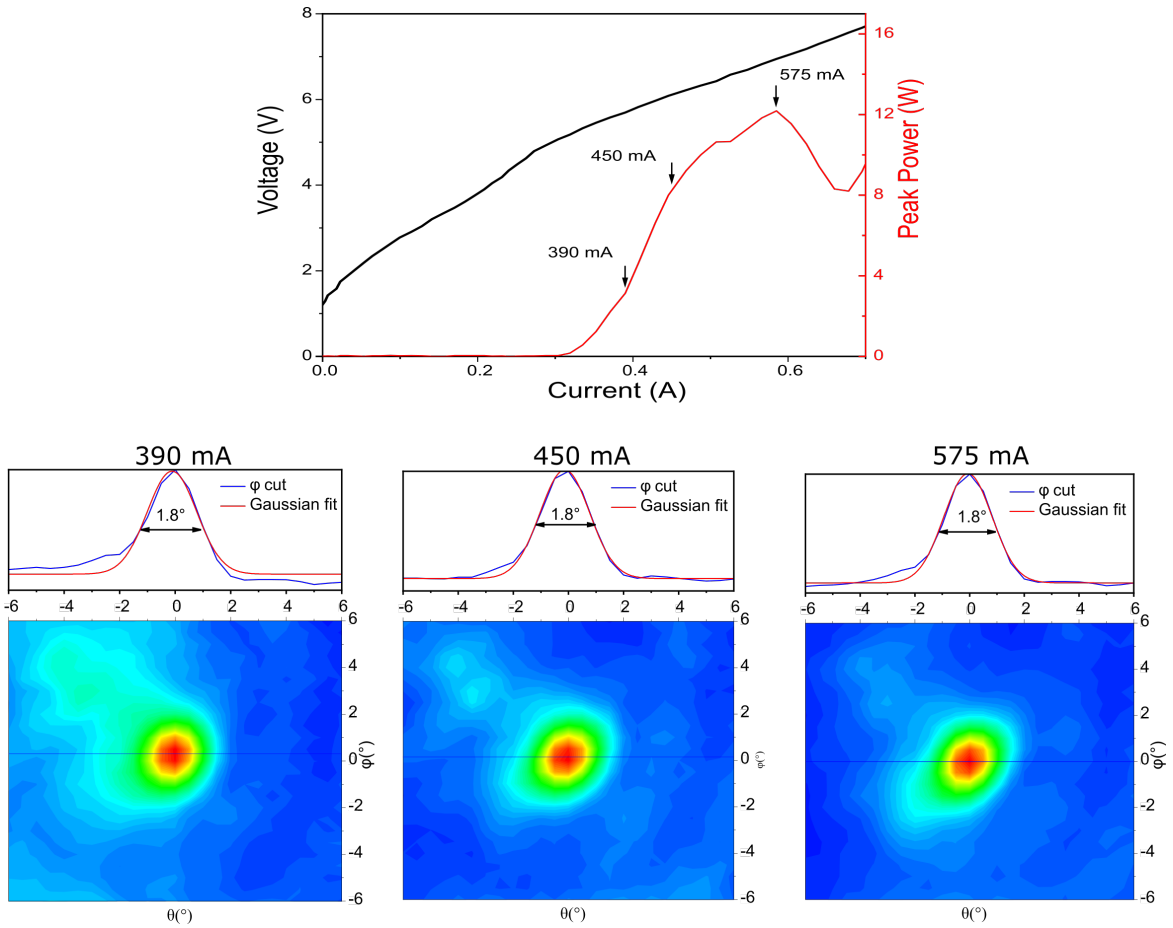

Figure 3.16: LIV curves and far-field intensity maps for sample s=15 μm, d= 40 μm. Data taken for three different bias currents. Profile taken in the ϕ direction. FWHM values calculated by fitting the ϕ cut with a Gaussian fit.

without affecting the quality of the far-field pattern. In the next sections, simulations will support this finding, and will show that the dominant factor involved in the far-field shaping is the total number of antenna elements.

3.5.2 Far-field simulations

In order to understand the constructive interference mechanism in the far-field which gives rise to the observed narrow beams with the PAM arrays, full-wave 3-dimensional numerical simulations were performed using COMSOL Multiphysics. The model consists of a planar array of $N \times N$ wired resonators of thickness 10 μm, separated a distance d. Figure 3.17 shows the model used for the simulations. Patch antenna microcavities and interconnecting wires consist of two block domains: a semiconductor (GaAs) and a metallic one (Au), which are placed over a ground metallic disc. We used the complex refractive indices for gold and GaAs as in Ref [119]. Internal ports with TM polarization were placed at the boundaries of the radiating slots of every patch antenna element to simulate the radiation from the structures. Every port is configured with the same amplitude and phase, with the intention that radiated fields are calculated for a phase-locked array. The planar array was enclosed into a sphere domain (air) terminated with a perfectly matched layer (PML) in the far-field zone to truncate the computational region. Radiation was collected at the far-field domain, created at the boundary between the air domain and the PML. The far-field pattern is calculated at this boundary.

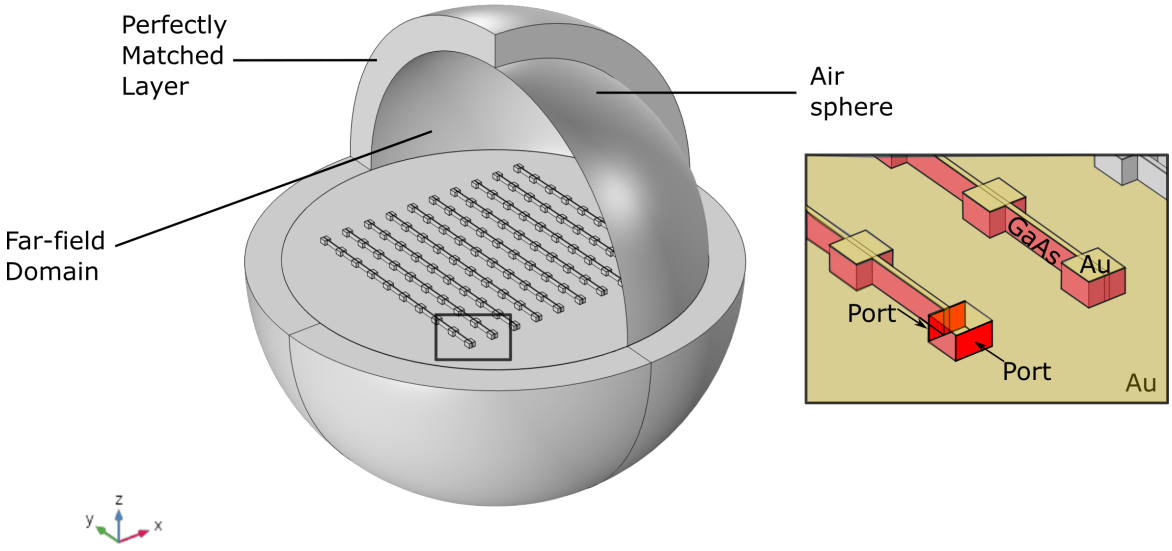

Figure 3.17: 3D simulation model. Model consists a wired patch antenna microcavity array enclosed by an air sphere domain bounded by a perfectly matched layer. Black rectangle contains a close-up view of a section of the array.

The air sphere and all the elements included within this domain were discretized with tetrahedral mesh elements of 0.2 wavelengths of size. For the metallic ground plane, a coarser mesh automatically calibrated by the program's *Physics-Controlled Mesh* feature was chosen. Finally, the mesh elements at the border of the air sphere domain were swept into triangular prisms to mesh the PML domains. A typical criterion for the meshing of PMLs and other absorbing layers is to cover the entire domain with at least 5 elements distributed along an edge in the absorbing direction [141]. The

finalized model contains $\sim 20 \times 10^6$ degrees of freedom to be solved. As this model required significant computational resources, we performed parallel computation (MPI) on the HPC clusters (DEIGO) of the Okinawa Institute of Science and Technology.

To compare the results obtained with the real devices, we first simulated arrays with N= 10 elements. Figure 3.18 shows a comparison between the simulated and experimental far-field intensity maps for an array with parameters s=15 μm, d= 40 μm. The simulated and measured far-field patterns are in excellent agreement. This observation confirms the phase-locking of the structure. Here, the phase-locking is ensured by the coupling with the plasmonic wires along the y-direction as well as other mutual coupling mechanisms known in antenna arrays, such as surface waves [142, 143] and far-field global coupling [86].

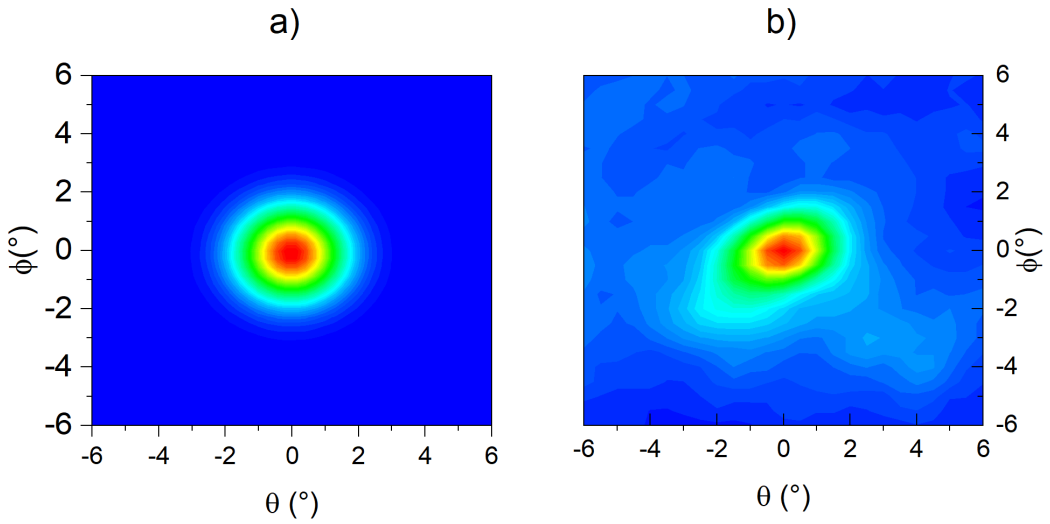

Figure 3.18: Comparison of the far-field intensity map between the simulated and measured results. Far-field intensity map of a 10 × 10 patch antenna microcavity array with parameters: s=15 μm, d= 40 μm obtained with a) full-wave finite element simulations and b) measurements. Adapted from [126].

The next task in the simulation study was to obtain the far-field profiles from arrays varying the parameters d and N. In Figure 3.19 a), the main trend is shown. The radiated far-field pattern narrows as the number of elements in the array is increased. For larger arrays, N is the dominant parameter, outweighing other parameters in the array, such as the periodicity $(s+d)$. This can be seen in panel b) of Figure 3.19 where the FWHM divergence is calculated for several array configurations. For a 10 × 10 array, simulations predict a saturation of the FWHM, whereas for others arrays the calculation shows a monotonic decrease with d.

A natural question arising from these results is how to make devices with an even narrower beam divergence. Considering N as the control parameter governing the beam shaping, one could select N as large as desired to get narrower beams. In fact, N defines the aperture size of the device, which can be defined as the electrical area that the radiator utilizes to emit electromagnetic waves (i.e. $N \times N \cdot s^2$) [109, 144]. The relation between the emitted electric field pattern in the far-field and the aperture

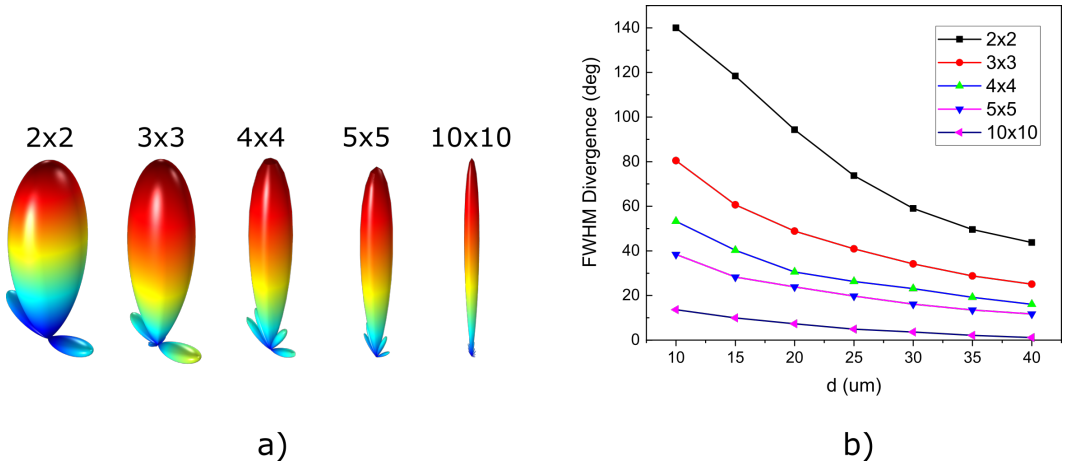

Figure 3.19: Far-field simulations for varying d and N. a) 3D far-field patterns emitted by $N \times N$ planar arrays with N= 2,3,4,5 and 10. (Distance is fixed to d= 40 μm). b) Calculated FWHM for different array configurations as a function of the distance of separation between elements d.

distribution is given by the spatial-frequency two-dimensional Fourier transformation (Fraunhofer diffraction principle). Then, if the aperture of the device is of infinite extent, the radiation pattern would take the form of a Dirac delta in the direction of the main lobe. Nevertheless, the limiting factor for achieving usable devices is rather practical. Figure 3.20 shows a simulation of the FWHM divergence for finite antenna arrays, where $1 \geq N \geq 50$. The beam divergence, as expected from the antenna theory, shows an asymptotic behavior following a $\sim 1/N^2$ dependence.

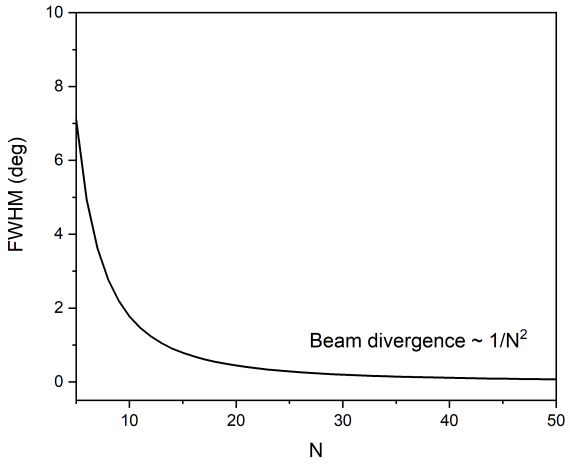

Figure 3.20: Simulated FWHM divergence as a function of N.

In practice, we found that an array consisting of 10×10 antenna elements delivered good electrical and optical characteristics while providing an excellent beam quality. In principle, one could increase the number of resonators, however this could come with a

higher probability of meeting lithographic errors and would also require a higher power current supply and possibly larger cryogenic consumption.

3.5.3 Side Lobes

One consequence of grouping antenna elements into arrays is the appearance of side lobes. This is a direct result of the beam formation by the constructive interference and a very general result of antenna arrays. For a planar array of $N \times N$ identical antenna elements separated by a distance dx and dy in the $x-$ and $y-$ direction respectively, the far-field radiation pattern can be approximated by the array factor (2.23):

$$AF(\theta,\phi) = \left\{ \frac{1}{M} \frac{\sin\left(\frac{M}{2}\psi_x\right)}{\sin\left(\frac{\psi_x}{2}\right)} \right\} \left\{ \frac{1}{N} \frac{\sin\left(\frac{N}{2}\psi_y\right)}{\sin\left(\frac{\psi_y}{2}\right)} \right\}$$

Due to the periodic nature of this expression, local maxima appear on the entire domain of the space coordinates. Thus, the appearance of side lobes (local maxima) is a direct sequel of arraying antennas. Figure 3.21 a) shows the measured far-field pattern of the sample s=15 μm, d= 40 μm taken for a window of $\pm 20°$ in both elevation and azimuthal directions. Within this range we observed two lateral lobes located at $\sim 5°$ and 10° from the main lobe, with intensities of -7 dB and -6 dB relative to the main beam, as shown by Figure 3.21 b). 3D numerical simulations reveal the formation of lateral lobes at similar distances with an order of magnitude lower intensity, which is in fairly good agreement with our experimental data (Figure 3.21 c)).

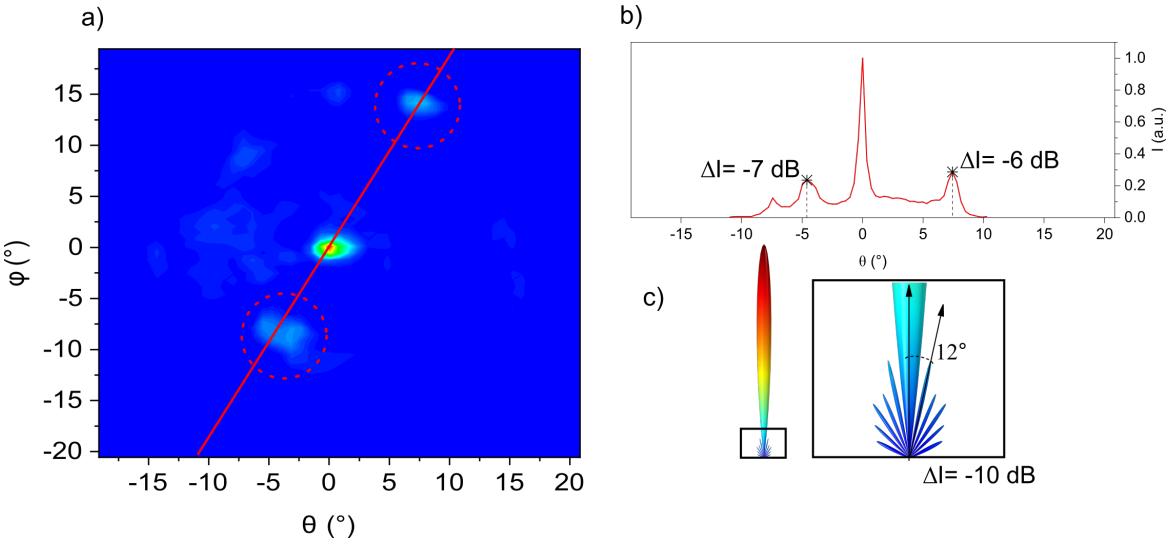

Figure 3.21: Presence of side lobes in arrays of patch-antenna microcavities. a) Identification of lateral lobes (circled in red) in the measured far-field pattern. b) Slice taken along the red line shown in panel a) showing the side lobes and their intensities relative to the main beam. c) 3D far-field pattern obtained by numerical simulations. A close-up view of the secondary lobes is shown in the black square to indicate the direction of the first lateral lobe.

One way to reduce the side lobes consists of arranging the antenna elements in a circular configuration as depicted in Figure 3.22. The figure presents the simulation model and the 2D far-field profiles compared to the planar array case. First, it is observed that the net gain of the far-field intensity for the circular array case is lower compared to the planar array. This is a logical consequence, as a planar array of $N \times N$ elements contains $\sim \sqrt{2}$-times more antenna elements than a circular array circumscribed in the square delimited by the perimeter of the planar array. Associated with this fact, the beam emitted by the circular array is broader. However, a reduction of the side-lobe levels for a circular array is evident. A quasi-suppression of the secondary lobes is observed for all the simulated configurations as seen in the red curves of Figure 3.22.

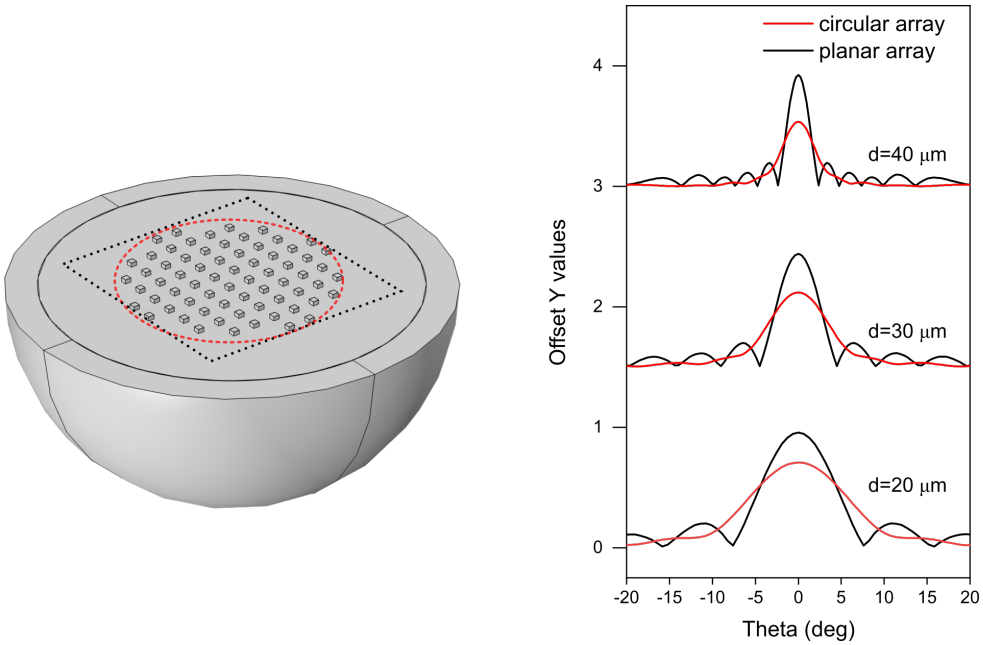

Figure 3.22: Study of the emission from a circular array. Left: simulation model. Dotted lines denotes the area occupied by a planar (black) and circular (red) array configurations. Right: comparison of the far-field profiles between circular and planar arrays. Parameters: $N = 10$, s=15 μm, d= 20,30, 40 μm.

The RF analogue of this effect is the method of the non-uniform excitation among the antenna elements [145, 146]. Binomial arrays with element spacing less than $\lambda/2$, typically produce far-field patterns with no side lobes [109]. However, this comes at the cost of broadening the beam. In a binomial distribution for a planar array, the amplitude of the antenna elements increases towards the center of the array and vanishes at the extremes. Our circular model mimics this configuration by having the larger concentration of antennas in the center. The applicability of this model could be useful for applications requiring low side-lobe levels. However, a compromise between side-lobe level and main lobe beamwidth must be made.

3.6 Summary

Chapter 3 combined the concepts of patch antenna arrays with quantum cascade active regions to demonstrate patch antenna microcavities THz QC lasers. First, a description of the QC sample used in this thesis was provided. Section 3.2 detailed the fabrication process followed to create the devices, and their full characterization was presented in section 3.3. Lasers emitting at 3.2 THz providing up to 25 mW output power with robust single mode frequency and spatial mode were demonstrated. Arrays of PAMs allow the beam shaping in the far-field, and unprecedented beam divergences, better than $2^\circ \times 2^\circ$ were measured consistently throughout various samples. Large-scale full-wave simulations of the emission from entire arrays presented in section 3.5.2 supported the experimental results by showing excellent agreement between simulated and measured data. Importantly, the beam shaping in the far-field depends only on the number of resonators, allowing the device to be functionalized through other array geometric parameters while preserving a high-quality far-field pattern.

Chapter 4

Advanced functionalities in Patch Antennas THz QCLs

This chapter discusses advanced functionalities that can be implemented in PAM THz QCLs. As anticipated from Chapter 2, the interconnecting wires introduce a degree of freedom to detune the degenerate fundamental modes, allowing polarization control. The first part of this chapter presents a study of the coherent control of the polarization states of PAMs via simulations and experimental demonstrations. The second part of this chapter presents ideas to pursue for a future work using the PAM design to achieve monolithic intracavity second harmonic generation THz QCLs, room temperature operation exploiting nonlinear down conversion from Mid-IR QCLs and an integrated beam-steering scheme for THz QCLs.

4.1 Polarization

Controlling the polarization state of a coherent light source is very useful for a wide variety of applications. For example, satellite communication systems use dual polarization antennas to double the channel capacity [147], circularly polarized light is of great importance in chemistry and biology for detecting molecules exhibiting circular dichroism [148] and laser sources with a variety of polarization states are used for manipulating quantum states, relevant for quantum cryptography [149, 150]. However, semiconductor lasers are mostly TE- or TM- linearly polarized, which is determined by the optical selection rules of the gain medium; and different polarization states are difficult to achieve. Typically, external optical elements such as polarizers and waveplates or other movable optics mounted in electromechanical piezoelectric components are used to control the polarization of light, which are bulky and expensive. Compact semiconductor lasers with polarization control capabilities integrated on chip are desirable, especially in the terahertz range, because many basic optical components are not readily available.

Elliptically polarized radiation from THz QCLs has been achieved in devices with orthogonally-oriented slot antennas patterned at the top metalized part of a DM ridge waveguide [151]. The grating-like structure enables surface emission with polarization control depending on the period of the grating. However, since the architecture is

based on a wide ridge waveguide, the grating outcoupling is influenced by the lasing on higher-order transverse modes in the structure. Then, the wide far-field profile presents multiple high-intensity peaks, and the polarization state strongly depends on the emission angle.

Dynamic control of the polarization states has also been achieved in THz QCLs [152]. By using two QCLs, each of them consisting of a waveguide coupled to an antenna array of subwavelength elements, a desired polarization state can be created by the superposition of two linearly polarized beams. The two QCLs are phase-locked with cross-polarized beams phase-shifted by $\pi/2$, achieved by the positioning of the elements in the array. By independently controlling the intensity of each QCL, the polarization of the overlapping beam can be tuned from linear to near-circular. However, due to the waveguide-antenna array configuration, single mode operation is not possible along all the lasing regime and higher order modes are excited for increased bias currents.

Elliptically or circularly polarized light can be treated as the superposition of two orthogonally polarized components. To obtain different polarization states, it is necessary to make the electric field oscillate in orthogonal directions. In this thesis, we use the well-defined orthogonal fundamental modes of PAMs to engineer different polarization states in THz QCLs, while preserving an excellent far-field profile and robust single mode operation. By means of numerical simulations, we identified the necessary conditions to obtain different polarization regimes and performed the corresponding measurements to experimentally validate the predictions obtained through simulations.

4.1.1 Simulations

Patch antenna microcavities support TM modes with resonant frequencies dictated by the equation (2.15). For a square patch microcavity, the fundamental TM_{01} and TM_{10} modes are degenerate, and the electric field distribution under the patches follows a half-wave resonance of E_z in the $x-$ direction for TM_{10} mode and in the $y-$ direction for the TM_{01} mode. As studied in section 2.4, the degeneracy is lifted when the microcavities are crossed at their center with interconnecting subwavelength wires, and the detuning between the TM_{01} and TM_{10} modes can be designed by varying the length d of the interconnecting wires. Figure 4.1 shows a reflectivity simulation study of the mode detuning for several array configurations varying the size of the patch antenna microcavities s and length of wires d. Black curves indicate the reflectivity spectra of the TM_{01} (parallel to the wires), and red curves indicate the reflectivity spectra corresponding to the TM_{10} mode (perpendicular to the wires).

To select a specific polarization state, one has to consider how each mode resonance is tuned relative to the frequency of the QCL active region Ω. A large detuning of one mode relative to Ω inhibits lasing from one mode, resulting in linear polarization. A small detuning of the modes with Ω allows to adjust their respective losses and thus the relative emitted intensity along x and y to achieve an elliptical polarization. The degenerate state (spectral overlap of the two modes at Ω) leads to circular polarization. Figure 4.2 provides a map of the resonant peaks of the fundamental modes plotted in Figure 4.1, which will help visualize the three regimes mentioned before. Blue shaded areas represent the gain region of the QCL. This region spans a bandwidth of 400 GHz. We assume the bandwidth of the ridge waveguide QCL plotted in the inset of Figure

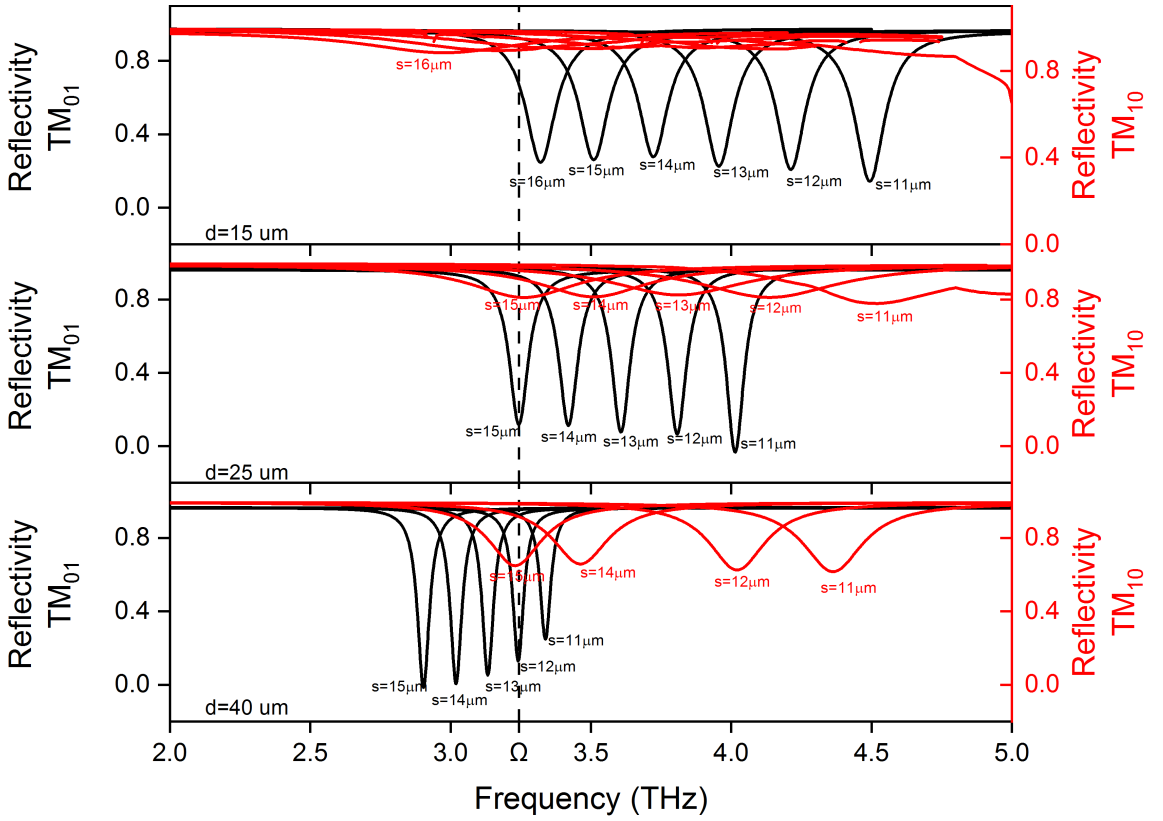

Figure 4.1: Detuning of the fundamental TM_{01} and TM_{10} modes. . Simulated reflectivity spectra of the TM_{01} modes (black), and reflectivity spectra of the TM_{10} mode (red). Ω represents the central frequency at which the QC active region presents gain.

3.12 to be close to the QCL active region spectral gain, which is in the range of what has been previously reported for bound-to-continuum and LO-phonon depopulation designs using Time-Domain Spectroscopy [153, 154]. Modes whose resonant frequencies fall within the gain area of the QCL will be excited.

An array of PAMs of size $s = 12$ μm interconnected with wires of length $d = 40$ μm (Figure 4.2 a)), sets the TM_{01} mode at the resonant frequency Ω while shifting the TM_{10} mode to a region where no intersubband gain is present. Therefore, linear polarization aligned with the direction of the wires is expected. Figure 4.2 b) indicates that an array of patches with $s = 16$ μm and $d = 15$ μm sets the fundamental TM_{01} and TM_{10} modes in the gain region of the QCL but slightly detuned one from each other. An elliptically polarized signal is expected from this device configuration. Lastly, mode degeneracy can be restored with an array with parameters $s = 15$ μm and $d = 25$ μm as shown in Figure 4.2 c). Here, the orthogonal modes are resonant at Ω, and the separation distance between the resonators is $\lambda/4$, producing a phase difference of $\pi/2$. Thus, a device with array parameters $s = 15$ μm and $d = 25$ μm will introduce a circular polarization.

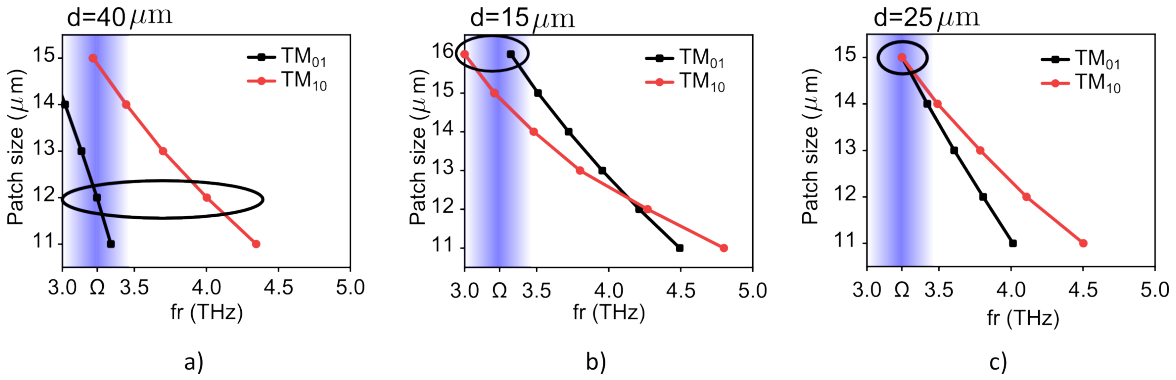

Figure 4.2: Map of the TM_{01} and TM_{10} resonant frequency peaks. Resonant frequency peaks obtained from reflectivity simulations, for arrays with different patch sizes s interconnected with wires of length $d = 40$ μm. Background blue colormap illustrates the gain of the QCL active region with its maximum located at $\Omega = 3.2$ THz. Points circumscribed in the oval indicate the fabricated and measured array. (b) and (c) same as (a) for wire lengths $d = 15$ and 25 μm, respectively.

4.1.2 Experimental demonstration

The devices identified via simulations showing the desired polarization states were fabricated and characterized. Polarization measurements were taken at the center of the far-field radiation pattern by rotating a wire-grid analyzer in front of a Golay cell detector. An aperture was set in between the detector and the analyzer to collect only the FWHM of the THz beam. All measurements were performed at a heat sink temperature of 77 K.

The first row of Figure 4.3 shows the polarization measurements for arrays with parameters a) $s = 12$ μm, $d = 40$ μm; b) $s = 16$ μm, $d = 15$ μm and c) $s = 15$ μm, $d = 25$ μm. For the first case, we measured a linear polarization (∼10:1) along the direction of the wires. As expected from the simulations, only the TM_{01} mode is resonant with the QCL gain. For this case, the electric field oscillates in the direction parallel to the wires, thus obtaining a linear polarization oriented in the same direction. Column b) shows the measurements performed for the sample exhibiting a slight detuning of the modes around Ω. For this condition, we obtained an elliptical polarization with the semi-major axis in the perpendicular direction of the wires. In column c) it is presented a device showing circular polarization. The mode degeneracy is restored and it's in resonance with Ω. For this case, we successfully measured a circular polarization achieving a degree of circular polarization (DOCP=$2\sqrt{I_{max} \cdot I_{min}}/(I_{max} + I_{min})$ [152]) as high as 99%.

The second row of Figure 4.3 incorporates the electrical and optical characterization of the selected devices. All measurements were taken in pulsed mode at a temperature of 77 K. A wired-grid analyzer was set in between a Golay cell detector and the cryostat containing the devices. Measurements were performed in the same way as detailed in section 3.3.1. Red and blue curves display the THz output power for two cross-polarized signals. Column a) exhibits the characteristics of the device emitting with linear polarization. As expected, maximum emission occurs in the direction parallel to

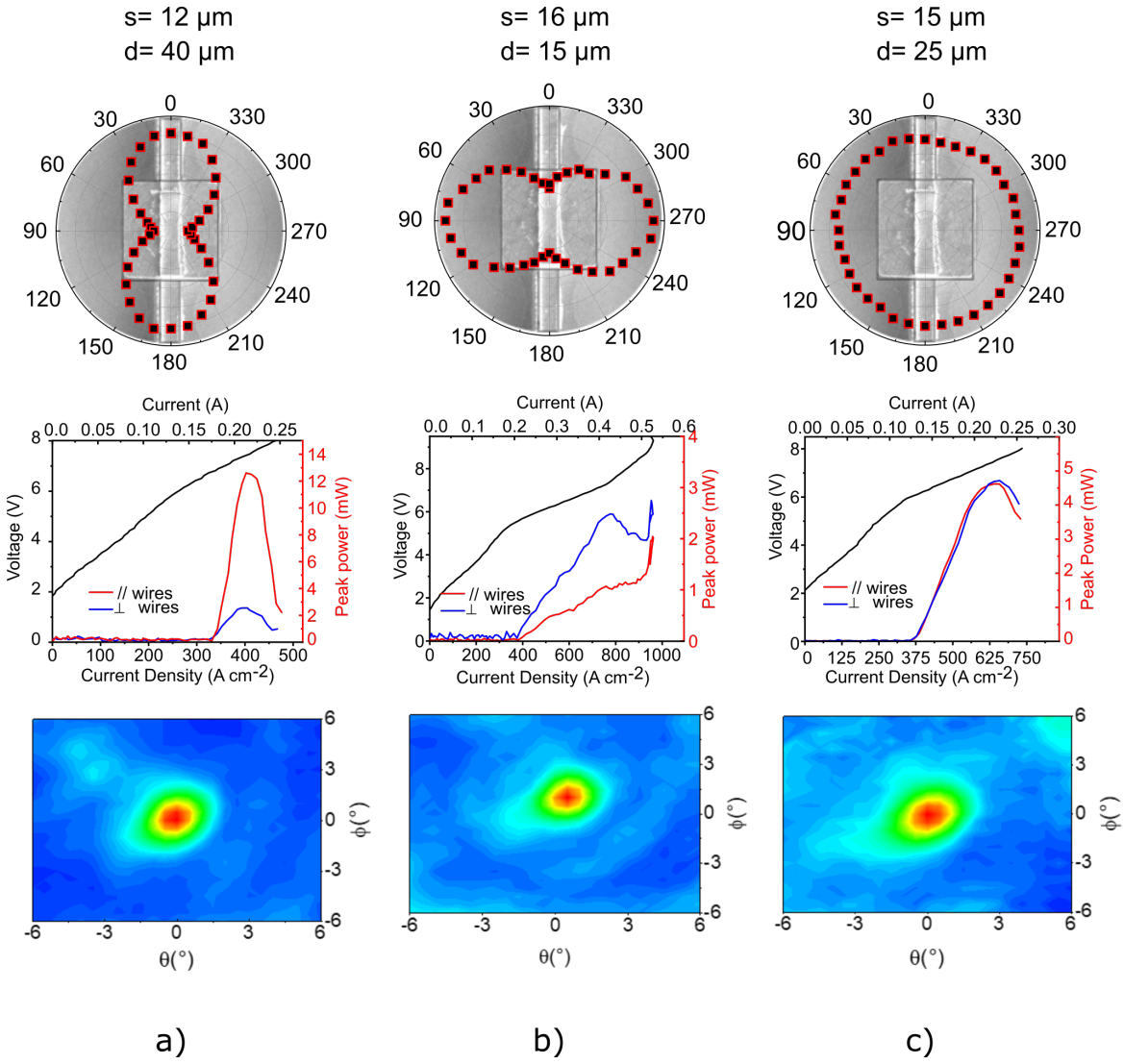

Figure 4.3: Measured polarization states and characterization from selected devices. Column a) contains data for an array with parameters $s = 12$ μm, $d = 40$ μm; column b) parameters: $s = 16$ μm, $d = 15$ μm and column c) $s = 15$ μm, $d = 25$ μm. 1st row: polar graph of the measured THz intensity showing the polarization of the device. An SEM image of the top of a single wired PAM is placed in the background of the polar plots to indicate the direction of the emitted THz signal relative to the PAM structure. 2nd row: Pulsed L-I-V characteristics (50 kHz, 25% duty cycle). The THz peak power of two cross-polarized signals are shown in red (polarization parallel to the wires) and blue (polarization perpendicular to the wires). 3rd row: measured far-field radiation pattern. All measurements were conducted at a heat sink temperature of 77 K.

the interconnecting wires. It is noted that there is a residual cross-component of the polarization. This is due to the patch antenna itself. It is very well known in the RF regime that for patches where the dielectric medium is of comparable size to the patch width, the fringing fields allowing the patch antenna to radiate bend at the corners providing a non-zero orthogonal polarization component [155, 156]. The amount of cross-polarization increases as the medium and resonant frequency increases. This can be mitigated, for example, by using a thinner active region. It is noteworthy to mention that cross-polarization suppression in arrays of patch antennas remains an active field in the RF [157, 158].

Column b) shows the measurements of the device with elliptical polarization. In this case, the signal polarized perpendicular to the wires' direction is slightly larger than the emission along the wires for all the lasing operation. Column c) corresponds to the circularly polarized array. To obtain a circular polarization, one needs to meet two conditions: same magnitude of the cross-polarized fields and a $\pi/2$ phase difference between them. These conditions are met for the device with $s = 15$ μm, $d = 25$ μm, which shows the cross-polarized emissions to be of equal magnitude at any bias current, and providing a separation between resonators of $\lambda/4$, introducing a phase difference of $\pi/2$.

Finally, the third row of Figure 4.3 collects the measured far-field measurements for the selected devices. We note that the beam shape is preserved for all the cases, confirming experimentally that the beam divergence depends essentially on the number of resonators forming the array, independent of its internal configuration.

The observation of the beam-shaping in the radiated polarized beams is evidence of the coherence of the polarization states. Our devices are phase-locked arrays which allow for beam shaping via the constructive interference of the in-phase ensemble of resonators. An incoherent emission or superposition of incoherent states would not allow for beam shaping, and instead of a narrow beamwidth, we would observe a far-field pattern that corresponds to the sum of the individual elements, namely an emission with a 180° angle.

To demonstrate that the resulting polarization state from the devices originates from the coherent superposition of both orthogonal contributions, we placed a commercial quarter waveplate (crystalline quartz and magnesium fluoride of thickness 1.4 mm) in between the wire-grid analyzer and the Golay cell detector, similar as it was done in Ref [151]. Figure 4.4 shows that adding a quarter waveplate allows retrieving a quasi-linear polarization, which would be impossible in the case of an incoherent emission.

4.2 Future work

In this section, we present three ideas for implementing advanced functionalities using the PAM array design. The subwavelength geometry of PAMs can be exploited to enhance nonlinear effects in QC active regions, such as second harmonic and difference frequency generation. Also, the array configuration can be used to mimic RF phased arrays, to achieve for example active beam steering.

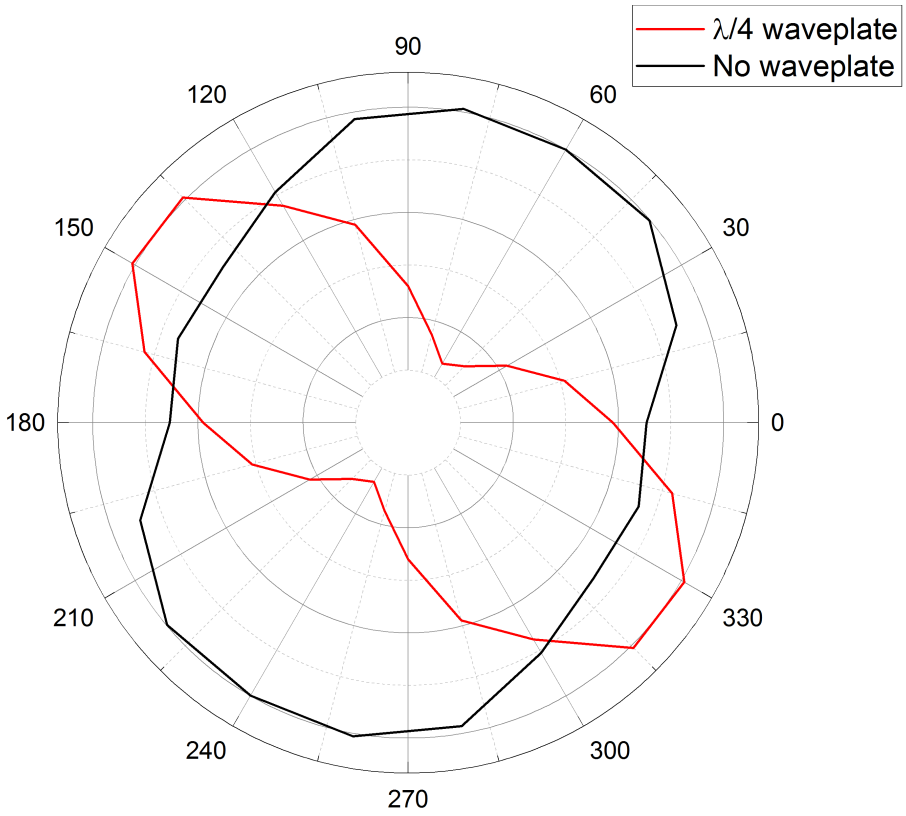

Figure 4.4: Demonstration of beam coherence. Polar plot of the polarization state from a coherent beam (black), and a linearly polarized signal (red) obtained by placing a quarter waveplate in between the wire-grid polarizer and a Golay cell detector.

4.2.1 Optical non-linearities

Second Harmonic Generation

It is known that intersubband transitions in coupled quantum wells can display giant non-linear optical susceptibilities that can trigger interesting nonlinear optical effects. [159]. For example, numerous efforts have succeeded in demonstrating efficient sum-frequency and second harmonic generation (SHG) in Mid-IR QCLs [160, 161], THz electro-optic wavelength conversion [162], THz lasers based on intracavity difference-frequency generation [163], wavelength conversion from THz to NIR [65], and most recently photonic generation of mm-waves [67]. While most of these examples use external laser sources to pump the QC active region, a monolithic approach for integrating the nonlinear optical transitions with the pump source is desirable for many applications. The QCL stands as an excellent platform to conceive this approach, as the QC material can act as both the pumping source and the mixing non-linear media, providing efficient means to couple the pump to the intersubband transitions. Further, the use of subwavelength confining microcavities can lead to high conversion efficiencies, as the small mode volumes result in increased energy density (SHG is proportional to the intensity of the electric field squared) [164].

Here, we propose to use patch antenna microcavities for THz SHG generation, as the deep subwavelength volumes ($10^{-7}\lambda^3$) provided by the microcavities could allow

efficient intracavity SHG resonant with the second-order mode of the patch antenna microcavities. Additionally, PAMs in arrays can be exploited to allow beam control and manipulation to achieve for example nonlinear beam shaping.

The idea consists in using the PAMs' fundamental and higher-order modes to be resonant simultaneously with the fundamental and SHG frequencies of the active region. Spatial overlap between the fundamental and SHG guided modes is necessary to obtain efficient SHG generation [165, 166]. Using numerical simulations, the optimized array parameters can be determined to identify the geometrical combinations that provide the overlap of the cavities' fundamental and second-order modes with the resonant frequency of the active region Ω and the second harmonic 2Ω ($TM_{01}(\Omega)$ and $TM_{20}(2\Omega)$). One of the challenges to overcome is the management of the dispersion in GaAs. Exploring non-symmetric microcavity designs like rectangular PAMs, can lead to the proper treatment of this effect.

Further, as the intensity of the mode confinement scales proportionally to the microcavities volumes, it would be interesting to explore SHG in THz QCLs with thin active regions (e.g. 5 μm and 2 μm). Exploiting the nonlinearities of QC active regions to achieve intracavity THz SHG would extend the frequency range accessible to THz QCLs.

Room temperature Patch Antenna Microcavity THz QCLs based on difference-frequency generation

High-temperature operation in THz QCLs is very challenging to achieve due to the onset of thermally activated LO phonon scattering causing the lifetime of the laser's upper state to decrease exponentially with temperature, thus suppressing the necessary population inversion condition. Various efforts to improve the temperature performance in THz QCLs by exploring novel active region designs and waveguide engineering have led to the realization of THz QCLs operating at 250 K (-23 °C), which is within the reach of thermoelectric cooling [57]. However, room temperature operation on these devices has not yet been reached. An alternative approach for generating THz radiation operating at high temperature in a monolithic configuration is based on the down-conversion from Mid-IR QCLs with high second-order susceptibilities. THz QCLs based on intra-cavity difference frequency generation (DFG) are the only electrically driven semiconductor sources covering a frequency range from 1 to 6 THz at room temperature [167]. The operating principle consists of stacking two sets of active regions optimized to emit at two closely spaced Mid-IR frequencies, then through the nonlinear process of difference-frequency mixing, the two Mid-IR frequencies interact in the active region producing an output in the THz range equal to the difference of the two Mid-IR signals [168]. In these devices, surface-emission schemes for the THz extraction have proven to improve the DFG outcoupling efficiency without affecting the properties for the mid-infrared pumps [163]. In consequence, it would be interesting to implement our PAM array design in THz-DFG-QCLs to obtain surface emission of THz radiation at room temperature with integrated beam shaping and control.

An idea to implement the PAM array configuration in DFG active regions consists in using rectangular PAMs, where one of the lateral sides, s_1 defines a resonant frequency f_1; and the other side, s_2 is designed to define a closely spaced resonant frequency f_2. By

interconnecting the PAM elements along two perpendicular directions, as schematically depicted in Figure 4.5 a balanced contribution from the fundamental TM(f_1) and TM(f_2) can be engineered with the wires geometry d_x and d_y, providing an optimized mode overlap in the active region.

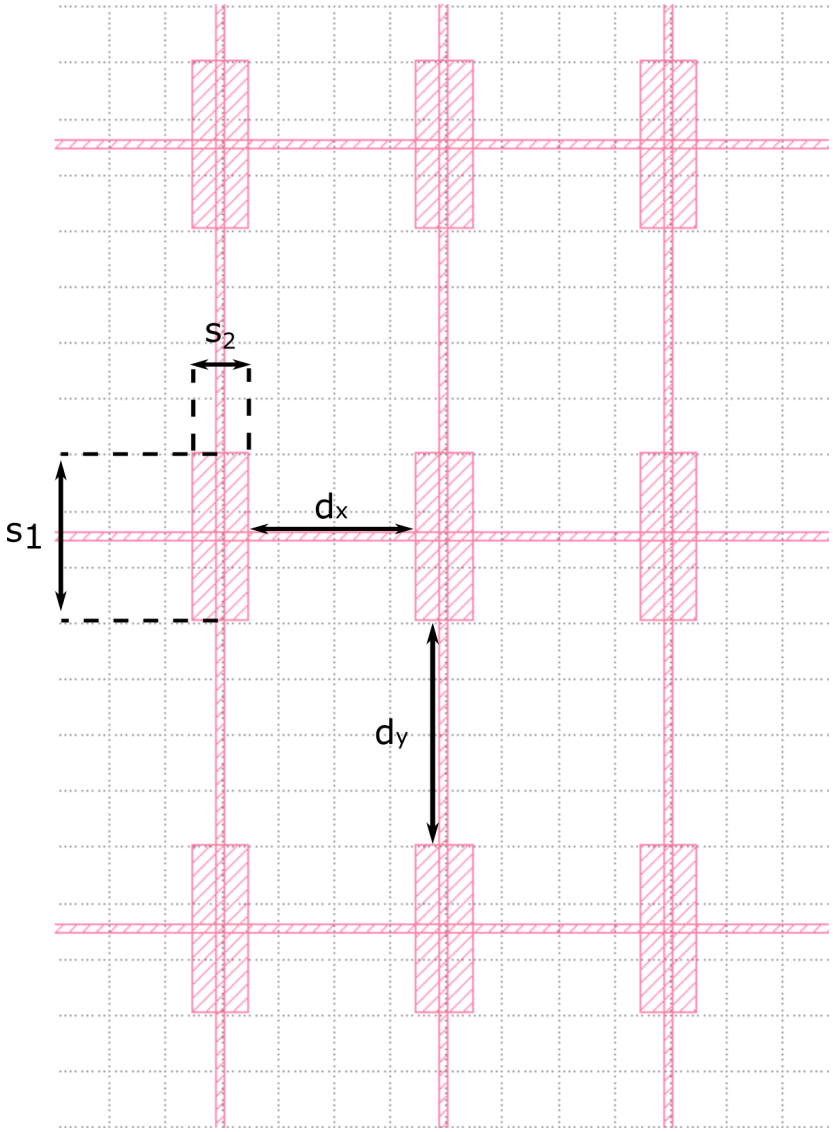

Figure 4.5: Idea for implementing PAM arrays in DFG active regions.

4.2.2 Beam steering

Beam steering refers to changing the direction of the main lobe of a radiation pattern of an antenna or antenna array. For current 5G and future 6G telecommunication systems, directional steerable antennas operating in the sub-mm and THz range will be essential for enabling energy-efficient smart wireless communication between the two ends of a communication link [169, 170]. In the most basic approach, beam steering can be accomplished by using mechanical bulky reflector dishes, lenses or programmable

diffraction gratings to re-direct the beam [171, 172]. These optomechanical components tend to be complex, low reliable, speed-limited and require critical alignment. A common approach in the RF for achieving beam steering in arrays of antennas relies on electronically changing the relative phase between the elements in the array. The angular dependence of the radiated total power from a planar array of antennas is proportional to the array factor (2.23). To account for the relative phase between elements, a phase term is added in expression (2.24):

$$\begin{aligned} \psi_x &= kd_x \sin\theta \cos\phi + \beta_x \\ \psi_y &= kd_y \sin\theta \sin\phi + \beta_y \end{aligned} \tag{4.1}$$

where β_x and β_y represent the difference in phase excitation between the elements along the $x-$ and $y-$ axis respectively. By controlling the phase difference between the elements, the beam can be scanned in any desired direction to form a scanning phased array, as illustrated in Figure 4.6

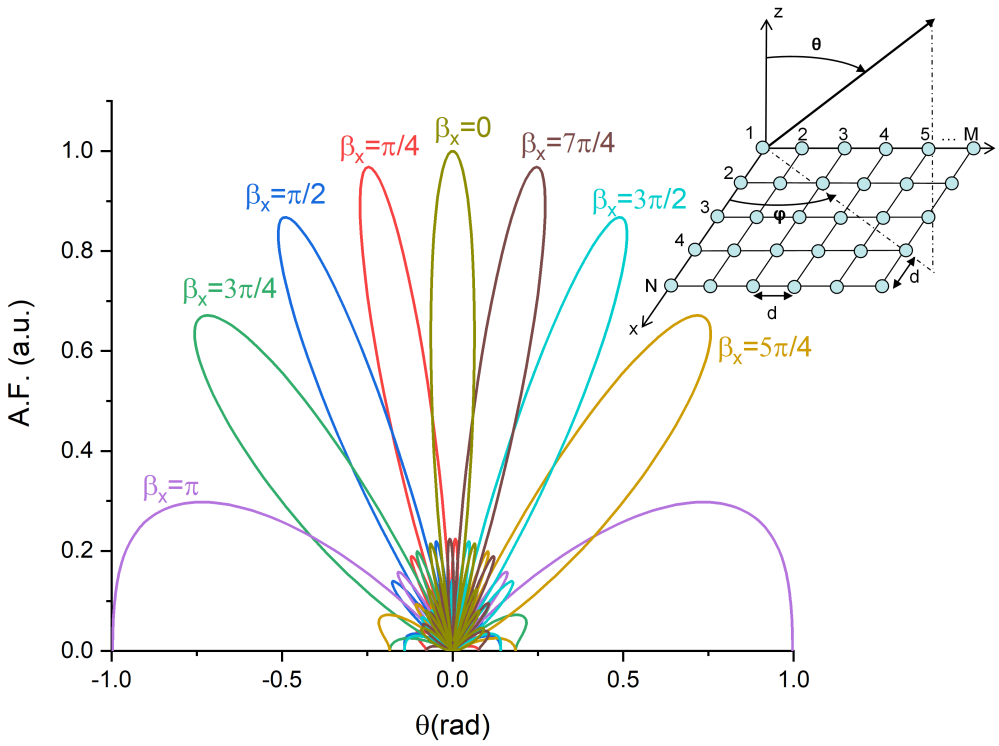

Figure 4.6: Beam steering in a planar array of antennas. Two dimensional array factor computed at the constant plane $\phi = \pi$ for a planar array of 10×10 antennas with a spacing of $d = \lambda/2$ for various progressive phase shift values between the elements. In the case of equal phase excitation between elements ($\beta_x = \beta_y = 0$), the main lobe points in the broadside direction (surface direction).

However, in THz, phase shifting is a non-trivial problem. Various attempts to achieve phase shifting have been made consisting on modulating the signal in another frequency band and then converting to THz [173]; phase shifters composed of reflectarrays made from tunable materials (e.g. liquid crystals [174]); or by using external

steering metasurfaces fabricated with tunable phase transition materials [175].

While these attempts involve the integration of multiple elements to achieve a beam scanning system, a monolithic integrated solution remains elusive. In the optical range, beam steering can be achieved by changing the refractive index of the medium through which the beam is transmitted. For example, in Ref [176] the authors utilize two closely spaced ridge lasers, each of them biased with independent injection currents to create beam scanning. Here, scanning is achieved by varying the pumping currents which creates an asymmetric variation in gain and refractive index, thus deflecting the beam. It would be interesting to apply this principle in our devices to achieve monolithic THz lasers with integrated polarization and beam scanning control. The main idea is to divide the array of patch antenna microcavities into two sections and bias them with independent currents, as depicted in Figure 4.7. By varying the ratio of the pump currents I_1/I_2, beam steering should occur without impacting significantly the beam characteristics imposed by the geometry of the array (low beam divergence and polarization).

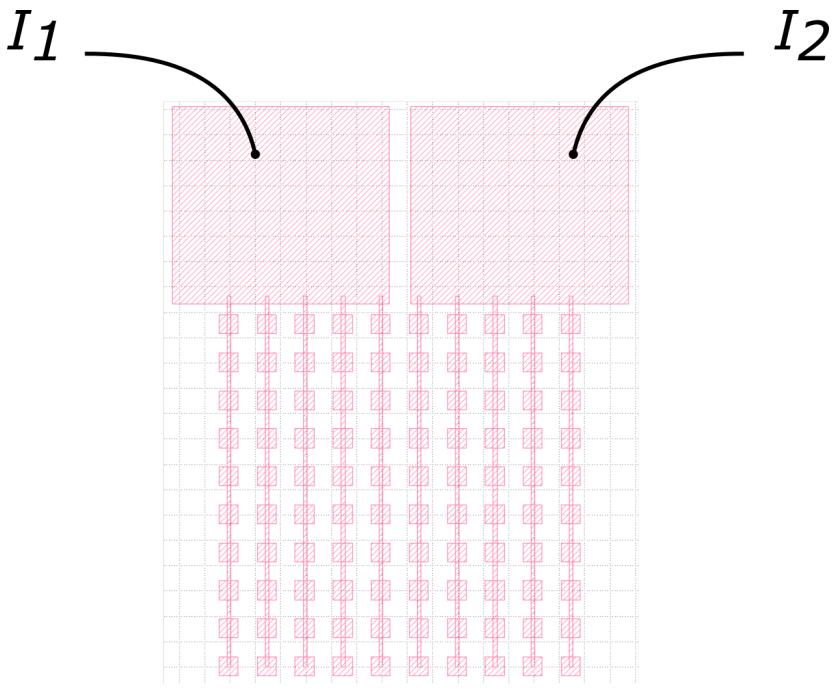

Figure 4.7: Idea for beam steering with patch antenna microcavity arrays. The array is splitted into two equal parts, each of them biased with an independent injection current I_1 or I_2. Beam steering is expected by varying the ratio I_1/I_2 as observed in ridge-waveguide NIR lasers [176].

4.3 Summary

Advanced functionalities which can be monolithically integrated into arrays of PAM THz QCLs were discussed. Section 4.1 explored the use of the interconnecting wires as a control parameter to design the polarization states of the lasers through detuning of

the PAMs' orthogonal fundamental modes. For linear polarization, a large detuning of one mode with the active region gain center frequency Ω needs to be set. A slight detuning of the modes within the intersubband gain region leads to elliptical polarization. An overlap of the two modes (degenerate case) at Ω results in circular polarization. Numerical simulations were used to identify the different combinations of the design parameters s and d that enabled the different polarization regimes to be observed. Experimental results (section 4.1.2) confirmed the effectiveness of the mode-detuning approach to generate any desired coherent polarization state, with high-quality beam properties. Finally, section 4.2, discussed three different ideas to enable further functionalities integrated into PAMs THz QCLs, such as intracavity SHG THz QCLs, room temperature patch antenna microcavity THz QCLs exploiting nonlinear down conversion from Mid-IR QCLs and THz QCLs with integrated active beam steering.

Conclusion

The purpose of this thesis was to study the emission from arrays of patch antenna microcavities incorporating a quantum cascade active region in the THz range. Patch antennas in arrays are among the most popular antenna schemes used in microwave technologies due to their versatility and ability to engineer and manipulate the emitted radiation. In this thesis, we aimed at transferring the beam engineering capabilities of patch antenna arrays into the THz range. Chapter 2 discussed in detail the characteristics of patch antennas from the microwave point of view, validating the *cavity model* as an accurate model to describe the radiation of patch antennas scaled for operation in the THz regime. Treatment of the losses at THz frequencies was evaluated via electromagnetic simulations. A first approach based on 2D simulations revealed that arrays of THz patch antenna microcavities provide precise control of the losses leading to engineered quality factors providing high photon extraction efficiencies. Further, a more realistic scenario considering 3D wired patch microcavity structures unveiled the potential of using the interconnecting subwavelength plasmonic wires as an additional degree of freedom to control the losses and frequency detuning of the initially degenerate and cross-polarized fundamental TM_{10} and TM_{01} modes. Chapter 3 presented the synthesis of patch antenna microcavity arrays and quantum cascade active regions. Via standard micro-fabrication methods, monolithic devices comprising 100 patch antenna microcavities embedding quantum cascade active regions were fabricated. The fabricated devices showed robust single mode lasing with an unprecedented low-divergence ($<2°$x$2°$) beam. Full-wave 3D numerical simulations supported the observed radiation characteristics and showed that the emitted beams depend only on the number of resonators contained in the array. This finding allowed to functionalize the device by using the array geometry to design advanced functionalities without altering the high-quality optical properties. Chapter 4 examined the integration of advanced functionalities in the conceived devices. First, coherent control of the polarization states was successfully demonstrated by exploiting the frequency detuning of the patch microcavities' fundamental modes, allowed by the geometry of the interconnecting wires. Identification of the array configuration yielding a desired polarization state was done through numerical simulations, and experimental demonstrations confirmed the validity of the model; obtaining polarization states from linear to circular in collimated narrow beams. Finally, the chapter discussed perspectives for implementing further functionalities using PAM arrays, such as intracavity SHG THz QCLs, room temperature patch antenna microcavity THz QCLs exploiting nonlinear down conversion from Mid-IR QCLs and THz QCLs with integrated active beam steering.

Integrated THz photonics, where a mixture of different features and capabilities

merge together in a laser source onto a monolithic device represents a significant technological step that could pave the path towards the long-standing goal of reaching a technological maturity in the THz range.

Bibliography

[1] T. J. Seok, A. Jamshidi, M. Kim, S. Dhuey, A. Lakhani, H. Choo, P. J. Schuck, S. Cabrini, A. M. Schwartzberg, J. Bokor, E. Yablonovitch, and M. C. Wu, *Radiation Engineering of Optical Antennas for Maximum Field Enhancement*, Nano Letters **11**, 2606–2610 (2011).

[2] A. E. Çetin, A. A. Yanik, C. Yilmaz, S. Somu, A. Busnaina, and H. Altug, *Monopole antenna arrays for optical trapping, spectroscopy, and sensing*, Applied Physics Letters **98**, 111110 (2011).

[3] X. Liu, T. Starr, A. F. Starr, and W. J. Padilla, *Infrared Spatial and Frequency Selective Metamaterial with Near-Unity Absorbance*, Phys. Rev. Lett. **104**, 207403 (2010).

[4] H. T. Miyazaki, T. Kasaya, H. Oosato, Y. Sugimoto, B. Choi, M. Iwanaga, and K. Sakoda, *Ultraviolet-nanoimprinted packaged metasurface thermal emitters for infrared CO2 sensing*, Science and Technology of Advanced Materials **16**, 035005 (2015).

[5] I. Puscasu and W. L. Schaich, *Narrow-band, tunable infrared emission from arrays of microstrip patches*, Applied Physics Letters **92**, 233102 (2008).

[6] D. R. Matthews, H. D. Summers, K. Njoh, S. Chappell, R. Errington, and P. Smith, *Optical antenna arrays in the visible range*, Opt. Express **15**, 3478–3487 (2007).

[7] D. Palaferri, Y. Todorov, A. Bigioli, A. Mottaghizadeh, D. Gacemi, A. Calabrese, A. Vasanelli, L. Li, A. G. Davies, E. H. Linfield, F. Kapsalidis, M. Beck, J. Faist, and C. Sirtori, *Room-temperature nine-microm-wavelength photodetectors and GHz-frequency heterodyne receivers*, Nature **556**, 85–88 (2018).

[8] Y. Todorov, A. M. Andrews, R. Colombelli, S. De Liberato, C. Ciuti, P. Klang, G. Strasser, and C. Sirtori, *Ultrastrong light-matter coupling regime with polariton dots*, Phys Rev Lett **105**, 196402 (2010).

[9] T. J. Cui, M. Q. Qi, X. Wan, J. Zhao, and Q. Cheng, *Coding metamaterials, digital metamaterials and programmable metamaterials*, Light: Science & Applications **3**, e218–e218 (2014).

[10] J. S. McLean, *A re-examination of the fundamental limits on the radiation Q of electrically small antennas*, IEEE Transactions on Antennas and Propagation **44**, 672– (1996).

[11] J. Madéo, Y. Todorov, and C. Sirtori, *Antenna-coupled microcavities for terahertz emission*, Applied Physics Letters **104**, 031108 (2014).

[12] A. J. L. Adam, I. Kašalynas, J. N. Hovenier, T. O. Klaassen, J. R. Gao, E. E. Orlova, B. S. Williams, S. Kumar, Q. Hu, and J. L. Reno, *Beam patterns of terahertz quantum cascade lasers with subwavelength cavity dimensions*, Applied Physics Letters **88**, 151105 (2006).

[13] M. Justen, C. Bonzon, K. Ohtani, M. Beck, U. Graf, and J. Faist, *2D patch antenna array on a double metal quantum cascade laser with >90Gaussian beam and selectable facet transparency at 1.9 THz*, Opt Lett **41**, 4590–4592 (2016).

[14] Y. Todorov, I. Sagnes, I. Abram, and C. Minot, *Purcell Enhancement of Spontaneous Emission from Quantum Cascades inside Mirror-Grating Metal Cavities at THz Frequencies*, Phys. Rev. Lett. **99**, 223603 (2007).

[15] J. Madéo, Y. Todorov, A. Gilman, G. Frucci, L. H. Li, A. G. Davies, E. H. Linfield, C. Sirtori, and K. M. Dani, *Patch antenna microcavity terahertz sources with enhanced emission*, Applied Physics Letters **109** (2016).

[16] L. Xu, D. Chen, T. Itoh, J. L. Reno, and B. S. Williams, *Focusing metasurface quantum-cascade laser with a near diffraction-limited beam*, Opt Express **24**, 24117–24128 (2016).

[17] C. A. Curwen, J. L. Reno, and B. S. Williams, *Broadband continuous single-mode tuning of a short-cavity quantum-cascade VECSEL*, Nature Photonics **13**, 855–859 (2019).

[18] C. A. Curwen, J. L. Reno, and B. S. Williams, *Terahertz quantum-cascade patch-antenna VECSEL with low power dissipation*, Applied Physics Letters **116**, 241103 (2020).

[19] L. Xu, C. A. Curwen, D. Chen, J. L. Reno, T. Itoh, and B. S. Williams, *Terahertz Metasurface Quantum-Cascade VECSELs: Theory and Performance*, IEEE Journal of Selected Topics in Quantum Electronics **23**, 1–12 (2017).

[20] L. E. Kreilkamp, I. A. Akimov, V. I. Belotelov, B. A. Glavin, L. V. Litvin, A. Rudzinski, M. Kahl, R. Jede, M. Wiater, T. Wojtowicz, G. Karczewski, D. R. Yakovlev, and M. Bayer, *Terahertz dynamics of lattice vibrations in Au/CdTe plasmonic crystals: Photoinduced segregation of Te and enhancement of optical response*, Phys. Rev. B **93**, 125404 (2016).

[21] K. Kitano, N. Ishii, and J. Itatani, *High degree of molecular orientation by a combination of THz and femtosecond laser pulses*, Phys. Rev. A **84**, 053408 (2011).

[22] X. Yang, C. Vaswani, C. Sundahl, M. Mootz, P. Gagel, L. Luo, J. H. Kang, P. P. Orth, I. E. Perakis, C. B. Eom, and J. Wang, *Terahertz-light quantum tuning of a metastable emergent phase hidden by superconductivity*, Nature Materials **17**, 586–591 (2018).

[23] M. Williams, D. Aschaffenburg, B. Ofori-Okai, and C. Schmuttenmaer, *Intermolecular Vibrations in Hydrophobic Amino Acid Crystals: Experiments and Calculations*, J. Phys. Chem. B **117**, 10444–10461 (2013).

[24] P. Jepsen and S. Clark, *Precise ab-initio prediction of terahertz vibrational modes in crystalline systems*, Chemical Physics Letters **442**, 275–280 (2007).

[25] K. Kawase, Y. Ogawa, Y. Watanabe, and H. Inoue, *Non-destructive terahertz imaging of illicit drugs using spectral fingerprints*, Opt. Express **11**, 2549–2554 (2003).

[26] D. M. Mittleman, R. H. Jacobsen, R. Neelamani, R. G. Baraniuk, and M. C. Nuss, *Gas sensing using terahertz time-domain spectroscopy*, Applied Physics B **67**, 379–390 (1998).

[27] A. G. Davies, A. D. Burnett, W. Fan, E. H. Linfield, and J. E. Cunningham, *Terahertz spectroscopy of explosives and drugs*, Materials Today **11**, 18–26 (2008).

[28] W. Chan, J. Deibel, and D. Mittleman, *Imaging with terahertz radiation*, Rep. Prog. Phys **70** (2007).

[29] M. Yamashita, C. Otani, T. Matsumoto, Y. Midoh, K. Miura, K. Nakamae, K. Nikawa, S. Kim, H. Murakami, and M. Tonouchi, *THz emission characteristics from p/n junctions with metal lines under non-bias conditions for LSI failure analysis*, Opt. Express **19** (2011).

[30] E. Heinz, T. May, D. Born, G. Zieger, S. Anders, V. Zakosarenko, H. Meyer, and C. Schäffel, *Passive 350 GHz Video Imaging Systems for Security Applications*, J Infrared Milli Terahz Waves **36**, 879–895 (2015).

[31] Z. Taylor, J. Garritano, S. Sung, N. Bajwa, B. Bennett, D.B. nad Nowroozi, P. Tewari, J. Ayre, J. Hubschman, S. Deng, E. Brown, and W. Grundfest, *THz and mm-Wave Sensing of Corneal Tissue Water Content: In Vivo Sensing and Imaging Results*, IEEE TRANSACTIONS ON TERAHERTZ SCIENCE AND TECHNOLOGY **5** (2015).

[32] V. Wallace, A. Fitzgerald, S. Shankar, N. Flanagan, R. Pye, J. Cluff, and D. Arnone, *Terahertz pulsed imaging of basal cell carcinoma ex vivo and in vivo*, British Journal of Dermatology **151**, 424–432 (2004).

[33] A. J. Fitzgerald, V. P. Wallace, M. Jimenez-Linan, L. Bobrow, R. J. Pye, A. D. Purushotham, and D. D. Arnone, *Terahertz Pulsed Imaging of Human Breast Tumors*, Radiology **239**, 533–540 (2006).

[34] F. Wahaia, G. Valusis, L. M. Bernardo, A. Almeida, J. A. Moreira, P. C. Lopes, J. Macutkevic, I. Kasalynas, D. Seliuta, R. Adomavicius, R. Henrique, and M. Lopes, *Detection of colon cancer by terahertz techniques*, Journal of Molecular Structure **1006**, 77–82 (2011).

[35] I. Kallfass, J. Antes, T. Schneider, F. Kurz, D. Lopez-Diaz, S. Diebold, H. Massler, A. Leuther, and A. Tessmann, *All Active MMIC-Based Wireless Communication at 220 GHz*, IEEE TRANSACTIONS ON TERAHERTZ SCIENCE AND TECHNOLOGY **1** (2011).

[36] G. Ducournau, P. Szriftgiser, A. Beck, D. Bacquet, F. Pavanello, E. Peytavit, M. Zacknoune, T. Akalin, and J. Lampin, *Ultrawide-Bandwidth Single-Channel 0.4-THz Wireless Link Combining Broadband Quasi-Optic Photomixer and Coherent Detection*, IEEE TRANSACTIONS ON TERAHERTZ SCIENCE AND TECHNOLOGY, **4** (2014).

[37] I. F. Akyildiz, J. M. Jornet, and C. Han, *Terahertz band: Next frontier for wireless communications*, Physical Communication **12**, 16–32 (2014).

[38] D. M. Mittleman, *Frontiers in terahertz sources and plasmonics*, Nature Photonics **7**, 666–669 (2013).

[39] R. A. Lewis, *A review of terahertz sources*, Journal of Physics D: Applied Physics **47**, 374001 (2014).

[40] *Instant Imaging With Terahertz Lasers.* `https://compoundsemiconductor.net/article/97378/Instant_imaging_with_terahertz_lasers/feature`. Accessed: 2021-03-22.

[41] A. Maestrini, J. Ward, J. Gill, H. Javadi, E. Schlecht, G. Chattopadhyay, F. Maiwald, N. R. Erickson, and I. Mehdi, *A 1.7-1.9 THz local oscillator source*, IEEE Microwave and Wireless Components Letters **14**, 253–255 (2004).

[42] S. Iwamatsu, Y. Nishida, M. Fujita, and T. Nagatsuma, *Terahertz coherent oscillator integrated with slot-ring antenna using two resonant tunneling diodes*, Applied Physics Express **14**, 034001 (2021).

[43] N. Kumar, U. Singh, A. Bera, and A. Sinha, *A review on the sub-THz/THz gyrotrons*, Infrared Physics & Technology **76**, 38–51 (2016).

[44] W. He, C. R. Donaldson, L. Zhang, K. Ronald, P. McElhinney, and A. W. Cross, *High Power Wideband Gyrotron Backward Wave Oscillator Operating towards the Terahertz Region*, Phys. Rev. Lett. **110**, 165101 (2013).

[45] G. P. Williams, *FAR-IR/THz radiation from the Jefferson Laboratory, energy recovered linac, free electron laser*, Review of Scientific Instruments **73**, 1461–1463 (2002).

[46] J. Niels Hovenier, M. Carmen Diez, T. O. Klaassen, W. T. Wenckebach, A. V. Muravjov, S. G. Pavlov, and V. N. Shastin, *The p-Ge terahertz laser-properties under pulsed- and mode-locked operation*, IEEE Transactions on Microwave Theory and Techniques **48**, 670–676 (2000).

[47] D. Auston, K. Cheung, and P. Smith, *Picosecond photoconducting hertzian dipoles*, Applied Physics Letters **45** (1984).

[48] P. Smith, D. Auston, and M. Nuss, *Subpicosecond Photoconductive Dipole Antennas*, IEEE Journal of Quantum Electronics **24** (1988).

[49] D. R. Bacon, J. Madéo, and K. M. Dani, *Photoconductive emitters for pulsed terahertz generation*, Journal of Optics (2021).

[50] J. B. Khurgin, *Optical rectification and terahertz emission in semiconductors excited above the band gap*, J. Opt. Soc. Am. B **11**, 2492–2501 (1994).

[51] K. H. Yang, P. L. Richards, and Y. R. Shen, *Generation of Far-Infrared Radiation by Picosecond Light Pulses in LiNbO3*, Applied Physics Letters **19**, 320–323 (1971).

[52] H. Roskos, M. Thomson, M. Kreß, and T. Löffler, *Broadband THz emission from gas plasmas induced by femtosecond optical pulses: From fundamentals to applications*, Laser & Photonics Reviews **1**, 349–368 (2007).

[53] F. Buccheri and X.-C. Zhang, *Terahertz emission from laser-induced microplasma in ambient air*, Optica **2**, 366–369 (2015).

[54] R. Köhler, A. Tredicucci, F. Beltram, H. E. Beere, E. H. Linfield, A. G. Davies, D. A. Ritchie, R. C. Iotti, and F. Rossi, *Terahertz semiconductor-heterostructure laser*, Nature **417**, 156–159 (2002).

[55] Y. Jin, J. L. Reno, and S. Kumar, *Phase-locked terahertz plasmonic laser array with 2W output power in a single spectral mode*, Optica **7**, 708–715 (2020).

[56] L. Li, L. Chen, J. Zhu, J. Freeman, P. Dean, A. Valavanis, A. Davies, and E. Linfield, *Terahertz quantum cascade lasers with >1 W output powers*, Electronics Letters **50**, 309–311 (2014).

[57] A. Khalatpour, A. K. Paulsen, C. Deimert, Z. R. Wasilewski, and Q. Hu, *High-power portable terahertz laser systems*, Nature Photonics **15**, 16–20 (2021).

[58] M. Wienold, B. Röben, L. Schrottke, R. Sharma, A. Tahraoui, K. Biermann, and H. T. Grahn, *High-temperature, continuous-wave operation of terahertz quantum-cascade lasers with metal-metal waveguides and third-order distributed feedback*, Opt. Express **22**, 3334–3348 (2014).

[59] G. Xu, L. Li, N. Isac, Y. Halioua, A. Giles Davies, E. H. Linfield, and R. Colombelli, *Surface-emitting terahertz quantum cascade lasers with continuous-wave power in the tens of milliwatt range*, Applied Physics Letters **104**, 091112 (2014).

[60] X. Wang, C. Shen, T. Jiang, Z. Zhan, Q. Deng, W. Li, W. Wu, N. Yang, W. Chu, and S. Duan, *High-power terahertz quantum cascade lasers with 0.23 W in continuous wave mode*, AIP Advances **6**, 075210 (2016).

[61] D. Burghoff, T.-Y. Kao, N. Han, C. W. I. Chan, X. Cai, Y. Yang, D. J. Hayton, J.-R. Gao, J. L. Reno, and Q. Hu, *Terahertz laser frequency combs*, Nature Photonics **8**, 462–467 (2014).

[62] M. Rösch, G. Scalari, M. Beck, and J. Faist, *Octave-spanning semiconductor laser*, Nature Photonics **9**, 42–47 (2015).

[63] T.-Y. Kao, J. L. Reno, and Q. Hu, *Amplifiers of free-space terahertz radiation*, Optica **4**, 713–716 (2017).

[64] D. Bachmann, N. Leder, M. Rösch, G. Scalari, M. Beck, H. Arthaber, J. Faist, K. Unterrainer, and J. Darmo, *Broadband terahertz amplification in a heterogeneous quantum cascade laser*, Opt. Express **23**, 3117–3125 (2015).

[65] J. Madéo, P. Cavalié, J. R. Freeman, N. Jukam, J. Maysonnave, K. Maussang, H. E. Beere, D. A. Ritchie, C. Sirtori, J. Tignon, and S. S. Dhillon, *All-optical wavelength shifting in a semiconductor laser using resonant nonlinearities*, Nature Photonics **6**, 519–524 (2012).

[66] P. Cavalié, J. Freeman, K. Maussang, E. Strupiechonski, G. Xu, R. Colombelli, L. Li, A. G. Davies, E. H. Linfield, J. Tignon, and S. S. Dhillon, *High order sideband generation in terahertz quantum cascade lasers*, Applied Physics Letters **102**, 221101 (2013).

[67] V. Pistore, H. Nong, P.-B. Vigneron, K. Garrasi, S. Houver, L. Li, A. Giles Davies, E. H. Linfield, J. Tignon, J. Mangeney, R. Colombelli, M. S. Vitiello, and S. S. Dhillon, *Millimeter wave photonics with terahertz semiconductor lasers*, Nature Communications **12**, 1427 (2021).

[68] R. N. Hall, G. E. Fenner, J. D. Kingsley, T. J. Soltys, and R. O. Carlson, *Coherent Light Emission From GaAs Junctions*, Phys. Rev. Lett. **9**, 366–368 (1962).

[69] M. I. Nathan, W. P. Dumke, G. Burns, F. H. Dill, and G. Lasher, *STIMULATED EMISSION OF RADIATION FROM GaAs p-n JUNCTIONS*, Applied Physics Letters **1**, 62–64 (1962).

[70] J. P. van der Ziel, R. Dingle, R. C. Miller, W. Wiegmann, and W. A. Nordland, *Laser oscillation from quantum states in very thin GaAs Al0.2Ga0.8As multilayer structures*, Applied Physics Letters **26**, 463–465 (1975).

[71] R. F. Kazarinov and R. A. Suris, *Possibility of the amplification of electromagnetic waves in a semiconductor with a superlattice*, Sov. Phys. Semicond. **5** (1971).

[72] J. Faist, F. Capasso, D. L. Sivco, C. Sirtori, A. L. Hutchinson, and A. Y. Cho, *Quantum Cascade Laser*, Science **264**, 553–556 (1994).

[73] C. Sirtori, J. Faist, F. Capasso, D. L. Sivco, A. L. Hutchinson, and A. Y. Cho, *Mid-infrared (8.5 μm) semiconductor lasers operating at room temperature*, IEEE Photonics Technology Letters **9**, 294–296 (1997).

[74] Y. Bai, S. Slivken, S. R. Darvish, and M. Razeghi, *Room temperature continuous wave operation of quantum cascade lasers with 12.5% wall plug efficiency*, Applied Physics Letters **93**, 021103 (2008).

[75] J. Faist, *Quantum Cascade Lasers*, OUP Oxford (2013).

[76] C. Worrall, J. Alton, M. Houghton, S. Barbieri, H. E. Beere, D. Ritchie, and C. Sirtori, *Continuous wave operation of a superlattic quantum cascade laser emitting at 2 THz*, Opt. Express **14**, 171–181 (2006).

[77] H. Luo, S. R. Laframboise, Z. R. Wasilewski, G. C. Aers, H. C. Liu, and J. C. Cao, *Terahertz quantum-cascade lasers based on a three-well active module*, Applied Physics Letters **90**, 041112 (2007).

[78] B. S. Williams, *Terahertz quantum-cascade lasers*, Nature Photonics **1**, 517–525 (2007).

[79] Y. Todorov, A. M. Andrews, I. Sagnes, R. Colombelli, P. Klang, G. Strasser, and C. Sirtori, *Strong Light-Matter Coupling in Subwavelength Metal-Dielectric Microcavities at Terahertz Frequencies*, Phys. Rev. Lett. **102**, 186402 (2009).

[80] A. W. M. Lee, Q. Qin, S. Kumar, B. S. Williams, Q. Hu, and J. L. Reno, *High-power and high-temperature THz quantum-cascade lasers based on lens-coupled metal-metal waveguides*, Opt. Lett. **32**, 2840–2842 (2007).

[81] F. Wang, I. Kundu, L. Chen, L. Li, E. H. Linfield, A. G. Davies, S. Moumdji, R. Colombelli, J. Mangeney, J. Tignon, and S. S. Dhillon, *Engineered far-fields of metal-metal terahertz quantum cascade lasers with integrated planar horn structures*, Opt Express **24**, 2174–82 (2016).

[82] M. I. Amanti, M. Fischer, G. Scalari, M. Beck, and J. Faist, *Low-divergence single-mode terahertz quantum cascade laser*, Nature Photonics **3**, 586–590 (2009).

[83] Y. Chassagneux, R. Colombelli, W. Maineult, S. Barbieri, H. E. Beere, D. A. Ritchie, S. P. Khanna, E. H. Linfield, and A. G. Davies, *Electrically pumped photonic-crystal terahertz lasers controlled by boundary conditions*, Nature **457**, 174–178 (2009).

[84] C. R. Williams, S. R. Andrews, S. A. Maier, A. I. Fernández-Domínguez, L. Martín-Moreno, and F. J. García-Vidal, *Highly confined guiding of terahertz surface plasmon polaritons on structured metal surfaces*, Nature Photonics **2**, 175–179 (2008).

[85] E. Mujagić, C. Deutsch, H. Detz, P. Klang, M. Nobile, A. M. Andrews, W. Schrenk, K. Unterrainer, and G. Strasser, *Vertically emitting terahertz quantum cascade ring lasers*, Applied Physics Letters **95**, 011120 (2009).

[86] T.-Y. Kao, J. L. Reno, and Q. Hu, *Phase-locked laser arrays through global antenna mutual coupling*, Nature Photonics **10**, 541–546 (2016).

[87] T.-Y. Kao, X. Cai, A. W. Lee, J. L. Reno, and Q. Hu, *Antenna coupled photonic wire lasers*, Opt. Express **23**, 17091–17100 (2015).

[88] G. Deschamps and W. Sichak, *Microstrip Micowave Antennas*, Proceedings of the Third Symposium on the USAF Antenna Research and Development Program. October 18-22 (1953).

[89] E. V. Byron, *A new flush-mounted antenna element for phased array application*, Phased-Array Antenna Symp (1970).

[90] R. Munson, *Microstrip Phased Array Antennas*, Proc. of the TwentySecond Symposium on the USAF Antenna Research and Development Program (1972).

[91] J. Howell, *Microstrip Antennas*, IEEE AP-S Int. Symp. Digest (1972).

[92] W. L. Barnes, A. Dereux, and T. W. Ebbesen, *Surface plasmon subwavelength optics*, Nature **424**, 824–830 (2003).

[93] E. Ozbay, *Plasmonics: Merging Photonics and Electronics at Nanoscale Dimensions*, Science **311**, 189–193 (2006).

[94] V. Giannini, A. I. Fernández-Domínguez, S. C. Heck, and S. A. Maier, *Plasmonic Nanoantennas: Fundamentals and Their Use in Controlling the Radiative Properties of Nanoemitters*, Chemical Reviews **111**, 3888–3912 (2011).

[95] L. Yousefi and A. C. Foster, *Waveguide-fed optical hybrid plasmonic patch nanoantenna*, Opt. Express **20**, 18326–18335 (2012).

[96] F. Bigourdan, F. Marquier, J.-P. Hugonin, and J.-J. Greffet, *Design of highly efficient metallo-dielectric patch antennas for single-photon emission*, Opt. Express **22**, 2337–2347 (2014).

[97] C. Belacel, B. Habert, F. Bigourdan, F. Marquier, J.-P. Hugonin, S. Michaelis de Vasconcellos, X. Lafosse, L. Coolen, C. Schwob, C. Javaux, B. Dubertret, J.-J. Greffet, P. Senellart, and A. Maitre, *Controlling Spontaneous Emission with Plasmonic Optical Patch Antennas*, Nano Letters **13**, 1516–1521 (2013).

[98] G. Lévêque and O. J. Martin, *Tunable composite nanoparticle for plasmonics*, Opt. Lett. **31**, 2750–2752 (2006).

[99] R. Esteban, T. V. Teperik, and J. J. Greffet, *Optical Patch Antennas for Single Photon Emission Using Surface Plasmon Resonances*, Phys. Rev. Lett. **104**, 026802 (2010).

[100] J. Grant, Y. Ma, S. Saha, A. Khalid, and D. R. S. Cumming, *Polarization insensitive, broadband terahertz metamaterial absorber*, Optics Letters **36**, 3476–3478 (2011).

[101] D. Palaferri, Y. Todorov, Y. N. Chen, J. Madeo, A. Vasanelli, L. H. Li, A. G. Davies, E. H. Linfield, and C. Sirtori, *Patch antenna terahertz photodetectors*, Applied Physics Letters **106** (2015).

[102] L. Xu, C. A. Curwen, P. W. C. Hon, Q.-S. Chen, T. Itoh, and B. S. Williams, *Metasurface external cavity laser*, Applied Physics Letters **107**, 221105 (2015).

[103] J. H. Wolfgang, *Equivalent Series Inductivity of a Narrow Transverse Slit in Microstrip*, IEEE Trans. On Microwave Theory and Technique **MMT-25** (1977).

[104] V. Zachou, G. Mayridis, C. G. Christodoulou, and M. T. Chryssomallis. *Transmission line model design formula for microstrip antennas with slots.* In *IEEE Antennas and Propagation Society Symposium, 2004.*, volume 4, pages 3613–3616 Vol.4, (2004).

[105] Y. Lo, D. Solomon, and W. Richards, *Theory and experiment on microstrip antennas*, IEEE Trans. Antennas Propagat. **AP-27** (1979).

[106] W. Richards, Yuen Lo, and D. Harrison, *An improved theory for microstrip antennas and applications*, IEEE Transactions on Antennas and Propagation **29**, 38–46 (1981).

[107] C. Ciracì, J. Britt Lassiter, A. Moreau, and D. R. Smith, *Quasi-analytic study of scattering from optical plasmonic patch antennas*, Journal of Applied Physics **114**, 163108 (2013).

[108] G. S. Unal and M. I. Aksun, *Bridging the Gap between RF and Optical Patch Antenna Analysis via the Cavity Model*, Scientific Reports **5**, 15941 (2015).

[109] C. A. Balanis, *Antenna Theory: Analysis and Design*, Wiley-Interscience, USA (2005).

[110] T.-Y. Kao, J. L. Reno, and Q. Hu, *Phase-locked laser arrays through global antenna mutual coupling*, Nature Photonics **10**, 541–546 (2016).

[111] D. M. Pozar, *Microwave engineering; 3rd ed.*, Wiley, Hoboken, NJ (2005).

[112] E. O. Hammerstad. *Equations for Microstrip Circuit Design.* In *1975 5th European Microwave Conference*, pages 268–272, (1975).

[113] C. A. Balanis, *Advanced engineering electromagnetics*, Wiley-Interscience, USA (1989).

[114] L. C. Godara, *Application of antenna arrays to mobile communications. II. Beamforming and direction-of-arrival considerations*, Proceedings of the IEEE **85**, 1195–1245 (1997).

[115] M. A. Jensen and J. W. Wallace, *A review of antennas and propagation for MIMO wireless communications*, IEEE Transactions on Antennas and Propagation **52**, 2810–2824 (2004).

[116] M. Bondarenko and V. Slyusar, *Influence of jitter in ADC on precision of direction-finding by digital antenna arrays*, Radioelectronics and Communications Systems **54** (2011).

[117] *An Introduction to the Finite Element Method.* `https://www.comsol.jp/multiphysics/finite-element-method`. Accessed: 2021-02-18.

[118] J. Madéo, J. Pérez-Urquizo, Y. Todorov, C. Sirtori, and K. M. Dani, *Engineering the Losses and Beam Divergence in Arrays of Patch Antenna Microcavities for Terahertz Sources*, Journal of Infrared, Millimeter, and Terahertz Waves **38**, 1321–1330 (2017).

[119] E. D. Palik. *Handbook of Optical Constants of Solids*, pages 429–443. Academic Press, Burlington, (1997).

[120] M. Wang, W. Wu, and Z. Shen, *Bandwidth Enhancement of Antenna Arrays Utilizing Mutual Coupling between Antenna Elements*, International Journal of Antennas and Propagation **2010**, 690713 (2010).

[121] S. Kohen, B. S. Williams, and Q. Hu, *Electromagnetic modeling of terahertz quantum cascade laser waveguides and resonators*, Journal of Applied Physics **97** (2005).

[122] R. N. Mitra and D. P. Agrawal, *5G mobile technology: A survey*, ICT Express **1**, 132–137 (2015).

[123] M. P. Joshi and V. J. Gond. *Microstrip patch antennas for wireless communication: A review.* In *2017 International Conference on Trends in Electronics and Informatics (ICEI)*, pages 96–99, (2017).

[124] C. Feuillet-Palma, Y. Todorov, A. Vasanelli, and C. Sirtori, *Strong near field enhancement in THz nano-antenna arrays*, Sci Rep **3**, 1361 (2013).

[125] H. T. Miyazaki, T. Mano, T. Kasaya, H. Osato, K. Watanabe, Y. Sugimoto, T. Kawazu, Y. Arai, A. Shigetou, T. Ochiai, Y. Jimba, and H. Miyazaki, *Synchronously wired infrared antennas for resonant single-quantum-well photodetection up to room temperature*, Nat Commun **11**, 565 (2020).

[126] J. Pérez-Urquizo, Y. Todorov, L. Li, A. G. Davies, E. H. Linfield, C. Sirtori, J. Madéo, and K. M. Dani, *Monolithic Patch-Antenna THz Lasers with Extremely Low Beam Divergence and Polarization Control*, ACS Photonics **8**, 412–417 (2021).

[127] M. Wienold, L. Schrottke, M. Giehler, R. Hey, W. Anders, and H. T. Grahn, *Low-voltage terahertz quantum-cascade lasers based on LO-phonon-assisted interminiband transitions*, Electronics Letters **45** (2009).

[128] G. Scalari, N. Hoyler, M. Giovannini, and J. Faist, *Terahertz bound-to-continuum quantum-cascade lasers based on optical-phonon scattering extraction*, Applied Physics Letters **86** (2005).

[129] *Telecentric Illumination.* `https://www.edmundoptics.com/knowledge-center/application-notes/imaging/telecentric-illumination-why-you-need-it-in-machine-vision-applications/`. Accessed: 2021-02-20.

[130] M. J. Madou, *Fundamentals of Microfabrication and Nanotechnology, Three-Volume Set*, Taylor & Francis, third edition (2011).

[131] M. A. Schmidt, *Wafer-to-wafer bonding for microstructure formation*, Proceedings of the IEEE **86**, 1575–1585 (1998).

[132] C. H. Tsau, S. M. Spearing, and M. A. Schmidt, *Fabrication of wafer-level thermocompression bonds*, Journal of Microelectromechanical Systems **11**, 641–647 (2002).

[133] B. S. Williams. *Terahertz quantum cascade lasers.* PhD thesis, Massachusetts Institute of Technology, (2003).

[134] E. Yablonovitch, T. Gmitter, J. P. Harbison, and R. Bhat, *Extreme selectivity in the lift-off of epitaxial GaAs films*, Applied Physics Letters **51**, 2222–2224 (1987).

[135] S. Agarwala, S. Horst, O. King, R. Wilson, D. Stone, D. Mario, and Y. Chen, *High-density inductively coupled plasma etching of GaAs/AIGaAs in BCl3/Cl2/Ar: A study using a mixture design experiment*, Journal of Vacuum Science & Technology B: Microelectronics and Nanometer Structures **16**, 511 – 514 (1998).

[136] S. Kumar, B. S. Williams, Q. Qin, A. M. Lee, Q. Hu, and J. L. Reno, *Surface-emitting distributed feedback terahertz quantum-cascade lasers in metal-metal waveguides*, Opt. Express **15**, 113–128 (2007).

[137] Y. Jin, L. Gao, J. Chen, C. Wu, J. L. Reno, and S. Kumar, *High power surface emitting terahertz laser with hybrid second- and fourth-order Bragg gratings*, Nat Commun **9**, 1407 (2018).

[138] S. Biasco, K. Garrasi, F. Castellano, L. Li, H. E. Beere, D. A. Ritchie, E. H. Linfield, A. G. Davies, and M. S. Vitiello, *Continuous-wave highly-efficient low-divergence terahertz wire lasers*, Nat Commun **9**, 1122 (2018).

[139] C. Wu, S. Khanal, J. L. Reno, and S. Kumar, *Terahertz plasmonic laser radiating in an ultra-narrow beam*, Optica **3**, 734–740 (2016).

[140] T.-Y. Kao, X. Cai, A. W. Lee, J. L. Reno, and Q. Hu, *Antenna coupled photonic wire lasers*, Opt. Express **23**, 17091–17100 (2015).

[141] *Setup and Meshing of Infinite Elements, Perfectly Matched Layers, and Absorbing Layers*. `https://www.comsol.jp/support/knowledgebase/1272`. Accessed: 2021-03-09.

[142] M. A. Khayat, J. T. Williams, D. R. Jackson, and S. A. Long, *Mutual coupling between reduced surface-wave microstrip antennas*, IEEE Transactions on Antennas and Propagation **48**, 1581–1593 (2000).

[143] C. Wang, E. Li, and D. F. Sievenpiper, *Surface-Wave Coupling and Antenna Properties in Two Dimensions*, IEEE Transactions on Antennas and Propagation **65**, 5052–5060 (2017).

[144] D. Headland, Y. Monnai, D. Abbott, C. Fumeaux, and W. Withayachumnankul, *Tutorial: Terahertz beamforming, from concepts to realizations*, APL Photonics **3**, 051101 (2018).

[145] C. L. Dolph, *A Current Distribution for Broadside Arrays Which Optimizes the Relationship between Beam Width and Side-Lobe Level*, Proceedings of the IRE **34**, 335–348 (1946).

[146] R. Chopra and G. Kumar, *Series-Fed Binomial Microstrip Arrays for Extremely Low Sidelobe Level*, IEEE Transactions on Antennas and Propagation **67**, 4275–4279 (2019).

[147] Jingshown Wu and Shan-An Yang. *Dual polarization waves reuse scheme in cross polarization channel.* In *Seamless Interconnection for Universal Services. Global Telecommunications Conference. GLOBECOM'99. (Cat. No.99CH37042)*, volume 5, pages 2714–2718 vol.5, (1999).

[148] B. Ranjbar and P. Gill, *Circular Dichroism Techniques: Biomolecular and Nanostructural Analyses- A Review*, Chemical Biology & Drug Design **74**, 101–120 (2009).

[149] T. Fujita, K. Morimoto, H. Kiyama, G. Allison, M. Larsson, A. Ludwig, S. R. Valentin, A. D. Wieck, A. Oiwa, and S. Tarucha, *Angular momentum transfer from photon polarization to an electron spin in a gate-defined quantum dot*, Nature Communications **10**, 2991 (2019).

[150] Y. Shi, S. Moe Thar, H. S. Poh, J. A. Grieve, C. Kurtsiefer, and A. Ling, *Stable polarization entanglement based quantum key distribution over a deployed metropolitan fiber*, Applied Physics Letters **117**, 124002 (2020).

[151] P. Rauter, J. Lin, P. Genevet, S. P. Khanna, M. Lachab, A. Giles Davies, E. H. Linfield, and F. Capasso, *Electrically pumped semiconductor laser with monolithic control of circular polarization*, Proceedings of the National Academy of Sciences **111**, E5623–E5632 (2014).

[152] G. Liang, Y. Zeng, X. Hu, H. Yu, H. Liang, Y. Zhang, L. Li, A. G. Davies, E. H. Linfield, and Q. J. Wang, *Monolithic Semiconductor Lasers with Dynamically Tunable Linear-to-Circular Polarization*, ACS Photonics **4**, 517–524 (2017).

[153] N. Jukam, S. S. Dhillon, D. Oustinov, Z.-Y. Zhao, S. Hameau, J. Tignon, S. Barbieri, A. Vasanelli, P. Filloux, C. Sirtori, and X. Marcadet, *Investigation of spectral gain narrowing in quantum cascade lasers using terahertz time domain spectroscopy*, Applied Physics Letters **93**, 101115 (2008).

[154] N. Jukam, S. S. Dhillon, D. Oustinov, J. Madéo, J. Tignon, R. Colombelli, P. Dean, M. Salih, S. P. Khanna, E. H. Linfield, and A. G. Davies, *Terahertz time domain spectroscopy of phonon-depopulation based quantum cascade lasers*, Applied Physics Letters **94**, 251108 (2009).

[155] T. Huynh and K. F. Lee. *Cross polarization characteristics of rectangular patch antennas.* In *1988 IEEE AP-S. International Symposium, Antennas and Propagation*, pages 708–711 vol.2, (1988).

[156] S. Bhardwaj and Y. Rahmat-Samii, *Revisiting the generation of cross-polarization in rectangular patch antennas: A near-field approach*, IEEE Antennas and Propagation Magazine **56**, 14–38 (2014).

[157] W. Yin, X. Liang, A. Chen, Z. Zhang, L. Shi, F. Guan, X. Liu, and J. Zi, *Cross-polarization suppression for patch array antennas via generalized Kerker effects*, Opt. Express **28**, 40–47 (2020).

[158] M. I. Pasha, C. Kumar, and D. Guha, *Mitigating High Cross-Polarized Radiation Issues Over the Diagonal Planes of Microstrip Patches*, IEEE Transactions on Antennas and Propagation **68**, 4950–4954 (2020).

[159] E. Rosencher, A. Fiore, B. Vinter, V. Berger, P. Bois, and J. Nagle, *Quantum Engineering of Optical Nonlinearities*, Science **271**, 168–173 (1996).

[160] C. Gmachl, A. Belyanin, D. L. Sivco, M. L. Peabody, N. Owschimikow, A. M. Sergent, F. Capasso, and A. Y. Cho, *Optimized second-harmonic generation in quantum cascade lasers*, IEEE Journal of Quantum Electronics **39**, 1345–1355 (2003).

[161] S. Liu, E. Lalanne, A. Johnson, P. Q. Liu, and C. Gmachl. *Intracavity second harmonic generation in quantum cascade lasers pumped by femtosecond Mid-IR pulses.* In *CLEO: 2011 - Laser Science to Photonic Applications*, pages 1–2, (2011).

[162] S. G. Carter, V. Ciulin, M. S. Sherwin, M. Hanson, A. Huntington, L. A. Coldren, and A. C. Gossard, *Terahertz electro-optic wavelength conversion in GaAs quantum wells: Improved efficiency and room-temperature operation*, Applied Physics Letters **84**, 840–842 (2004).

[163] M. A. Belkin, F. Capasso, A. Belyanin, D. L. Sivco, A. Y. Cho, D. C. Oakley, C. J. Vineis, and G. W. Turner, *Terahertz quantum-cascade-laser source based on intracavity difference-frequency generation*, Nature Photonics **1**, 288–292 (2007).

[164] L. Ateshian, H. Choi, M. Heuck, and D. Englund. *Terahertz Light Sources by Electronic-Oscillator-Driven Second Harmonic Generation in Extreme-Confinement Cavities*, (2020).

[165] Z. Lin, X. Liang, M. Lončar, S. G. Johnson, and A. W. Rodriguez, *Cavity-enhanced second-harmonic generation via nonlinear-overlap optimization*, Optica **3**, 233–238 (2016).

[166] C. Wang, Z. Li, M.-H. Kim, X. Xiong, X.-F. Ren, G.-C. Guo, N. Yu, and M. Lončar, *Metasurface-assisted phase-matching-free second harmonic generation in lithium niobate waveguides*, Nature Communications **8**, 2098 (2017).

[167] K. Fujita, S. Jung, Y. Jiang, J. H. Kim, A. Nakanishi, A. Ito, M. Hitaka, T. Edamura, and M. A. Belkin, *Recent progress in terahertz difference-frequency quantum cascade laser sources*, Nanophotonics **7**, 1795–1817 (2018).

[168] K. Fujita, S. Hayashi, A. Ito, M. Hitaka, and T. Dougakiuchi, *Sub-terahertz and terahertz generation in long-wavelength quantum cascade lasers*, Nanophotonics **8**, 2235–2241 (2019).

[169] A. H. Naqvi and S. Lim, *Review of Recent Phased Arrays for Millimeter-Wave Wireless Communication*, Sensors **18** (2018).

[170] I. F. Akyildiz, A. Kak, and S. Nie, *6G and Beyond: The Future of Wireless Communications Systems*, IEEE Access **8**, 133995–134030 (2020).

[171] M. Alonso-delPino, C. Jung-Kubiak, T. Reck, N. Llombart, and G. Chattopadhyay, *Beam Scanning of Silicon Lens Antennas Using Integrated Piezomotors at Submillimeter Wavelengths*, IEEE Transactions on Terahertz Science and Technology **9**, 47–54 (2019).

[172] Y. Monnai, K. Altmann, C. Jansen, H. Hillmer, M. Koch, and H. Shinoda, *Terahertz beam steering and variable focusing using programmable diffraction gratings*, Opt. Express **21**, 2347–2354 (2013).

[173] Y. Yang, O. D. Gurbuz, and G. M. Rebeiz, *An Eight-Element 370–410-GHz Phased-Array Transmitter in 45-nm CMOS SOI With Peak EIRP of 8–8.5 dBm*, IEEE Transactions on Microwave Theory and Techniques **64**, 4241–4249 (2016).

[174] G. Perez-Palomino, M. Barba, J. A. Encinar, R. Cahill, R. Dickie, P. Baine, and M. Bain, *Design and Demonstration of an Electronically Scanned Reflectarray Antenna at 100 GHz Using Multiresonant Cells Based on Liquid Crystals*, IEEE Transactions on Antennas and Propagation **63**, 3722–3727 (2015).

[175] M. R. M. Hashemi, S.-H. Yang, T. Wang, N. Sepúlveda, and M. Jarrahi, *Electronically-Controlled Beam-Steering through Vanadium Dioxide Metasurfaces*, Scientific Reports **6**, 35439 (2016).

[176] D. R. Scifres, W. Streifer, and R. D. Burnham, *Beam scanning with twin-stripe injection lasers*, Applied Physics Letters **33**, 702–704 (1978).

Appendix A

Fabrication Protocol

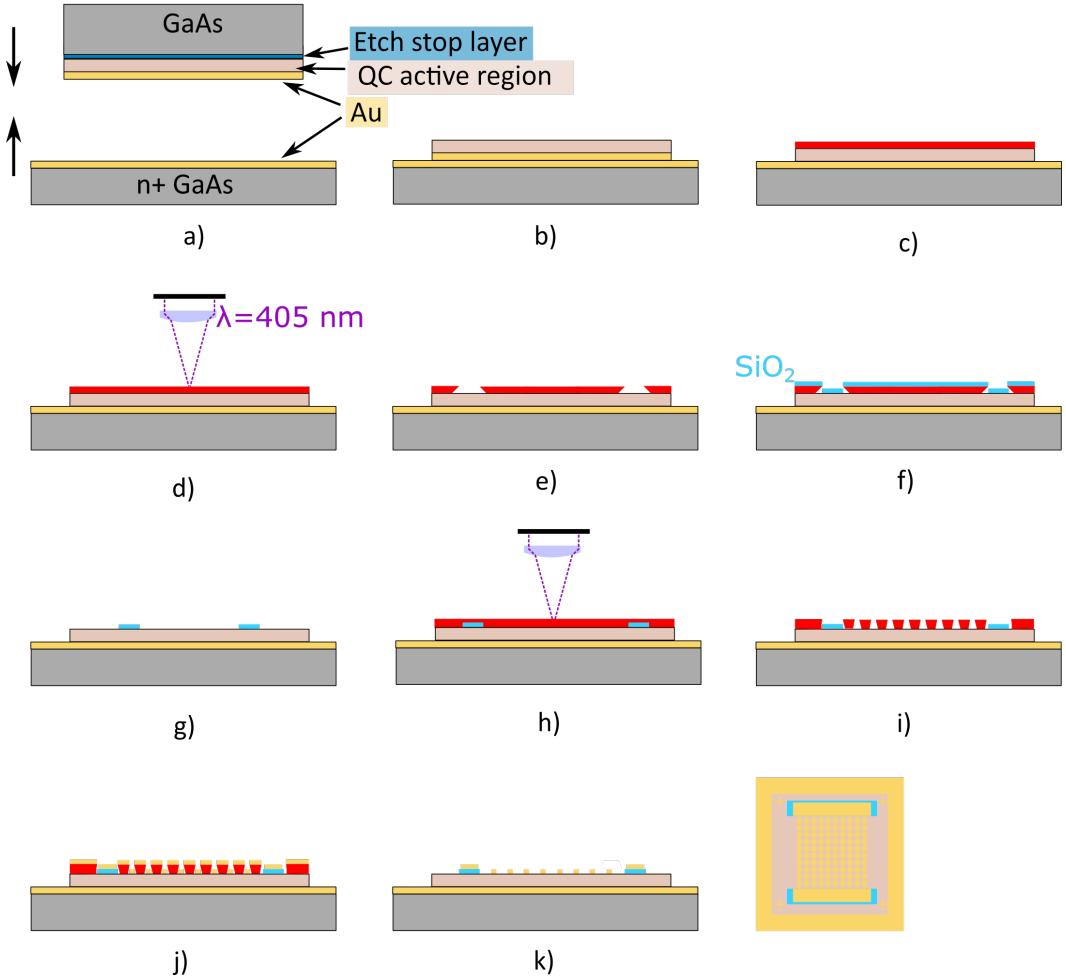

Figure A.1: Fabrication procedure. a) Wafer bonding. b) Substrate removal. c) Photoresist spin coating. d) 1st layer Photolithography. e) Development of photoresist. f) SiO_2 thin film sputtering. g) Lift-off. h) Lithography 2nd layer. i) Development of 2nd layer photoresist. j) Ti/Au thin film deposition. k) Lift-off. Process finishes.

1. Substrate removal (Wet etching)	Citric acid (100 gr) + H_2O_2 (40 ml) + H_2O (100 ml) . 55° C. HF. 2 minutes
2. First Layer (Photolithography)	Resist: ARN 4450 (-) Spin coating: (1) 500 rpm, 10 sec. (2) 5000 rpm 50 sec. Bake: 90°C, 10 min Dose: 1500 mJ/cm^2 Post exposure bake: 100°C, 8 min Develop: TMAH 50 sec, DI water 50 sec Lift off: Remover PG, First bath: 60°C, 30 min.
2. First Layer (SiO_2 Sputtering)	Power: 180 W Target: SiO_2 Time: 6500 sec MFC11: 10 sccm MFC12=MFC13=MFC14=MFC15 0.0 sccm Rot. speed: 10 rpm Deposited material: 200 nm
3. Second Layer (Photolithography)	Resist: ARN 4450 (-) Spin coating: (1) 500 rpm, 10 sec. (2) 5000 rpm 50 sec. Bake: 90°C, 10 min Dose: 1500 mJ/cm^2 Post exposure bake: 100°C, 8 min Develop: TMAH 50 sec, DI water 50 sec Lift off: Remover PG. First bath: 60°C, 30 min.
3. Second Layer (Ti/Au deposition)	Ar treatment (10 sccm, 5 min) Ti: 10 nm Au: 400 nm
4. Final etch (ICP)	RF Power: 20 W ICP Power: 800 W BCl_3= 10 sccm Cl_2: 20 sccm